Universitat Politècnica de Catalunya

Barcelona Tech

Departament de Física

Dynamics of disordered systems

Alessandro Vispa

A thesis submitted for the degree of Doctor of Science

Barcelona, September 2016

Supervised by

Dr. **Luis Carlos Pardo**

Prof. Dr. **Josep Lluis Tamarit**

Thesis supervised by:

Dr. Luis Carlos Pardo Soto

Universitat Politècnica de Catalunya, Barcelona, Spain

Grup de Caracterització de Materials - GCM

Prof. Dr. Josep Lluis Tamarit Mur

Universitat Politècnica de Catalunya, Barcelona, Spain

Grup de Caracterització de Materials - GCM

The research in this PhD thesis has been carried out within the doctoral program of Computational and Applied Physics of the Department of Physics of the Universitat Politècnica de Catalunya - Barcelona Tech. It has been supported by the FPI/UPC fellowship reference 2011.

Dynamics of disordered systems

Alessandro Vispa

Departament de Física, Universitat Politècnica de Catalunya

Abstract

Disordered systems are ubiquitous in nature and their study is complicated and often leads to controversial results. In any case, the important role of such systems in science and technological applications should not be ignored.

The characteristic properties of such systems seem to be driven by a fundamental feature, the degrees of freedom. Although many problems still remain matter of debate, the challenge posed in recent decades in the understanding of the impact of disorder in the physical behavior of materials is of considerable scientific interest.

An exact description of a disordered phase is not possible since it is a many-body problem hard to model. However, for some materials it is possible, upon cooling, to preserve the disordered liquid-like structure having a state of high regularity. Therefore, for the so-called glass formers, it is possible to freeze some degrees of freedom obtaining a glass that presents some liquid-like properties with the high viscosity of a solid below the melting temperature T_m.

The aim of the present PhD thesis is to present our understanding of disorder in related experimental approaches using three different pure compounds: two plastic crystals (1-Chloroadamantane and Freon113) and a liquid (Glycerol). To understand the behavior of these kinds of materials neutron scattering and dielectric spectroscopy have been used. These two powerful techniques allow us to investigate the dynamics of disordered phases on a picosecond time scale. Furthermore, given the complexity of these disordered phases, data analysis and model selection have been performed with a Bayesian approach that provides a solid statistical ground based on probability distribution functions.

Such methods have been applied to study the above mentioned compounds dynamics in order to provide an explanation of some open questions.

The plastic phase of Cl-Adamantane ($C_{10}H_{15}Cl$) has been investigated in order to study the its short range order and its dynamics. In the temperature range where the experiments have been performed, a thermal effect has been detected and it has been linked to a dynamical and structural change. This has been supported by the thermodiffractograms that have been measured in a recent experiment at D1B. Here, a neutron diffraction and spectroscopy study is reported. The analysis of the width permit us to have

a consistent picture of the mechanism on a picosecond time scale, against which the most recent models for Cl-Adamantane dynamics can be verified. Model selection, performed with the fitting algorithm FABADA, give us a preliminary, qualitative description about the motions of the molecules in the plastic phase.

The orientational glass former Freon113 ($Cl_2FC - CClF_2$) has been object of a dynamic and thermodynamic study in order to analyze its kinetic and thermodynamic fragilities. By means of dielectric spectroscopy coupled with calorimetry and inelastic neutron scattering we show that the high value of fragility (kinetic and thermodynamic) is connected to a coupling between low-energy modes and acoustic phonon branches. Such dynamics contribute to the excess entropy which it is the cause of the very high value of fragility.

For what concerns the dynamics of one of the prototypical glass-forming liquid, glycerol ($C_3H_8O_3$), we report a quasielastic neutron scattering study as a function of temperature. The spectral analysis has shown the presence of three different motions: one related to the translation of the whole molecule and two confined and temperature-independent movements. A thorough analysis, based on Bayesian inference, of the complete energy range allowed us to perform a robust model selection.

In addition, a brief overview of the theoretical background for neutron scattering and dielectric spectroscopy, as well as a description of the experimental setup and the consequent data treatment and analysis, are given to deliver a comprehensive and consistent view of the topic under consideration.

The results, presented in Chapters 6, 7 and 8, , represent a small step for a deeper understanding of the disordered phases dynamics, giving a base for further investigations.

List Of Publications

I **FABADA Goes MANTID to Answer an Old Question: How Many Lines Are There?** D. Monserrat, A. Vispa, L. C. Pardo, R. Tolchenov, S. Mukhopadhyay, F. Fernandez-Alonso. JPCS, 663 012009 (2015).

II **Insights into the determination of molecular structure from diffraction data using a Bayesian algorithm** A. Henao, M. Rovira-Esteva, A. Vispa, J. Ll. Tamarit, E. Guardia, L. C. Pardo. Journal of Physics: Condensed Matter, 25 (45), 454217, 2013.

III **Coupling of the dynamics and structure at the thermodynamic anomaly of the plastic phase of 1-Chloroadamantane.** A. Vispa, D. Monserrat, G. J. Cuello, F. Fernandez-Alonso, S. Mukhopadhyay, F. Demmel, J.Ll. Tamarit, L. C. Pardo. (in preparation).

IV **Thermodynamic and kinetic fragility of Freon113: the most fragile plastic crystal.** A. Vispa, M. Romanini, M. A. Ramos, L. C. Pardo, F. J. Bermejo, M. Hassaine, A.I. Krivchikov, J. W. Taylor, J. Ll. Tamarit. (submitted).

V **A robust comparison of dynamical scenarios in a glass-forming liquid.** A. Vispa, S. Busch, J. Ll. Tamarit, T. Unruh, F. Fernandez-Alonso, L. C. Pardo. Phys. Chem. Chem. Phys., 18 3975 (2016).

VI **Microscopic dynamics of glycerol: a QENS study** A. Vispa, M. Rovira-Esteva, M.D. Ruiz-Martin, S. Busch, T. Unruh, L. C. Pardo, J. Ll. Tamarit. JPCS, 549 012013 (2014).

Role of the author in this work

The present work of thesis presents the analysis and discussion of results from dynamic investigation of disordered phases.

The experiments have been performed by the author at FRMII, ISIS facilities for what concerns the quasielastic neutron studies and at ILL for diffraction measurements, while the Broadband Dielectric Spectroscopy experiment has been done using the GCM (Group of Characterization of Materials) laboratories at Universitat Politècnica de Catalunya.

The Bayesian fit method used for the analysis is presented in papers I and II. A detailed description is contained in Chapter 5. The author performed the model selection presented in Section 5.5.1.

The original research part of the thesis is contained in Part IV. Chapter 6 contains the diffraction and quasielastic studies on 1-Clhoroadamantane (paper III - not published yet), experiments and analysis were performed by the author, as well as the writing of the manuscript with revision and discussion of the coauthors. Chapter 7 contains all the results for the dynamic and thermodynamic study on Freon113 (paper IV - submitted), in this case the author performed the BDS experiment and analysis and assisted in the writing of the manuscript, while the calorimetric and inelastic neutron scattering, performed by coauthors, are presented for sake of completeness. The study on liquid Glycerol (papers V and VI) presented in Chapter 8 has been performed in collaboration between the author and coauthors as well as the writing of the manuscript.

The whole work of the author has been done under the supervision of Dr. Luis Carlos Pardo and Prof. Dr. Josep Lluis Tamarit.

Contents

Part I

Introduction

Chapter 1

Disordered phases

1.1 From order to disorder

Order and disorder are quite complex concepts with several exceptions and shades, that make difficult to give them a generally accepted and shared definition [1].

An example of a system highly ordered is given by a perfect crystal, which can be reproduced knowing the symmetry and the arrangement of atoms and molecules in the unit cell. Therefore a regular spatial matrix of atoms or molecules is the reference configuration most appropriate for modeling a crystalline solid. Such a regularly ordered structure is maintained, at least in principle, through the entire material, and this regularity can be described by the concept of lattice (long range order) and locally by the coordination number (short-range order). Hence a perfect crystal possesses translational and orientational simmetries, this implies that relatively simple models can describe the physical phenomena in solids, permitting a complete determination of the positions and orientations of atoms and molecules (Figure 1.1a).

The concept of disorder is instead, in some way, easier [1]. Being strongly connected to the concept of "aleatoric", it can be defined as a state of lack or departure from the state of order.

The exact reverse of the situation in a solid is given by the ideal gas, in which atoms and molecules are subjected to greater thermal energy with respect to the attractive forces. This results in a constant movement, where position and orientation are not correlated and in which the probability of interaction between them is very low. Hence,

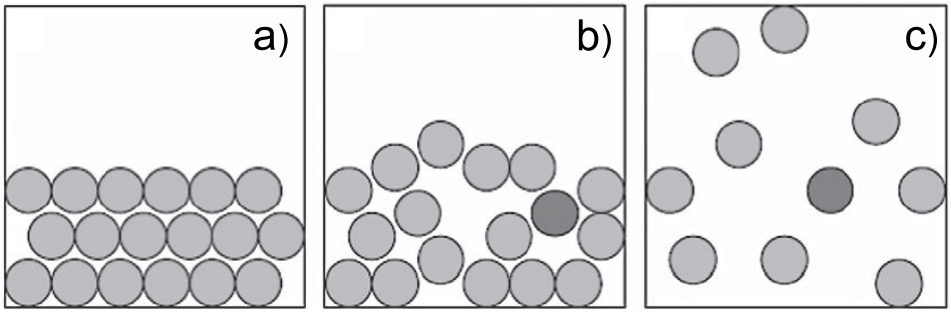

Figure 1.1: 2D diagram of the structure different phases of matter: (a) a solid, (b) a liquid, and (c) a gas [2].

order is almost absent and the reference configuration can be described as random. These make of an ideal gas a perfect disordered system (Figure 1.1c).

The competition between the forces exerted by the atoms and molecules, which favor the order and the thermal agitation which leads to disordered systems, causes a physical restriction for which no system is completely ordered or disordered.

It is clear that disordered systems play a fundamental role in daily life, in the life sciences and natural sciences, as well as in technology development. Most of the phenomena on this planet includes systems (gas, liquid and amorphous systems) that present a certain degree of disorder, such as phenomena related to the environment as all the processes that occur in the atmosphere, the physics of water, biological processes that include liquids and amorphous systems. Such systems have also attracted considerable interest because they have been the base in the development of new technological applications such as photovoltaic cells, pharmaceuticals, liquid-crystals, refrigerants and building materials.

The scientific challenges offered by these systems is extremely complex, and modeling can vary from simple semi-empirical models to computer simulations. However, each of these models has its value in the understanding of disordered systems with regard to their complexity from the dynamics, energetic and structural point of view.

1.2 Liquids

Liquids occupy a very important position in physics, chemistry and technology [3]. At present there is no unique, shared theory that gives a good approximation of the liquid state, but there are models that tend to the solid and gas limits previously described.

Liquid properties such as densities ρ, thermal expansion coefficient α and compressibility K_T are typically not too different from the corresponding solid. Unlike the solid, however, liquids, as well as the gases, have the ability to flow, even if the viscosities in liquids are higher than those in the gases. This indicates that the molecules in fluids move relatively easily. This is a consequence of the types of interactions that are present in the liquid state. Such interactions allow to atoms or molecules, that compose it, to move freely through the material, but at the same time, these constituents are held together by relatively weak forces, sufficient to not permit a behavior such as that which occurs in the gaseous state.

The choice of a reference model in a liquid becomes therefore much more problematic, in fact, although a long-range order is not present, there is a short-range order, and the concept of coordination number (number of closest neighbor molecules around a given one) is still valid for liquids [2]. The presence of a short-range kind of order implies that the relative positions and orientations between nearest atoms or molecules are related even if this correlation is not persistent over long distances. Thus, a liquid does not show translational and orientational long-range order.

Liquids, as solids, present a quite high level of packaging of their constituents, that implies a nearly incompressibility. In many compounds the volume occupied by an atom in the liquid is similar to the volume occupied in the associated crystal. Therefore, packaging determines the structure of many liquid systems, which results to be, at least considering a small fraction of molecules in the liquid, very similar to the arrangement of the elements that constitute the crystal (Figure 1.2). The number of covalent bonds, for example, and with some exceptions, is on average the same between the liquid phase and crystalline phase.

As a consequence of the thermal agitation and the absence of forces that maintain the liquid particles in fixed positions, particles are free to move and the short-range order can be viewed as a transient order.

While the thermal motion in a gas is easily visualized and leads to a random dis-

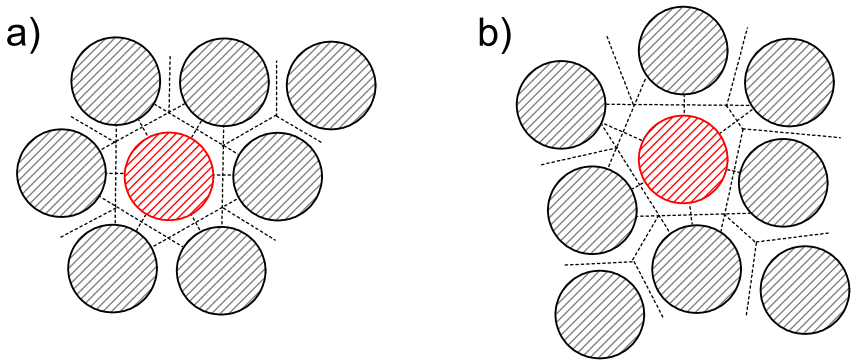

Figure 1.2: (a) Schematic picture of a regularly ordered system as a crystal, and (b) a sketch of the disordered structure as can be found in liquids and glasses [4].

tribution of the positions and orientation of the constituent particles, in a liquid, the problem becomes more complex.

In a highly packed liquid, many of the atoms or molecules are confined by their neighbors so that each of them can move only in the space delimited by the "cage" formed by the neighbors themselves. As soon as the atom or molecule moves away from the center of the confinement, the collisions with the particles surrounding it, reverses its speed and sends it back. Motions of this type have frequencies of the order of $10^{12} - 10^{13}$ Hz, similar to those of the vibrational motions in a solid or of the internal vibrations in a molecule, and may last on average for times of the order of a few picoseconds before being damped out.

Nevertheless, the confinement is not rigid. After a certain characteristic time (relaxation time) which depends on how the thermal motion is altered by intermolecular forces, the motions of the neighbors can allow the release of the central particle from the confinement, starting a diffusive motion that will lead it far from its initial position. It is therefore possible to visualize a picture in which the constituents are hopping along a zig-zag trajectory composed of discrete microscopic linear motions and interspersed with confined movements in residence sites. The hopping frequencies can be of the order of $10^{10} - 10^{12}$ Hz. Macroscopically it is possible to find the evidence of diffusive motions noticing that two miscible liquids are slowly mixed together without applying any external force to facilitate the blending. In this chaotic motion, the so-called Brownian

motion (R. Brown 1827), the particles move irregularly because they undergo random collisions with the constituents of the medium.

Such description can be used at the microscopic level to model the diffusing movement of a liquid particle, on time scales higher than that of the movements localized within the the confinement.

1.3 Plastic crystals

A plastic crystal is a crystal in which molecules interact weakly and possess some orientational degree of freedom. In this state, an intermediate behavior between the crystalline (translationally and orientationally long-range ordered) and the liquid phase (translationally and orientationally long-range disordered) is present. Compounds that show such state are also called *orientationally disordered crystals* (ODIC). In these mesophase the positional degree of freedom is suppressed, and the molecules are only allowed to rotate in a more or less free way, being their centers of mass forming an ordered lattice (such compounds exhibit a perfect crystalline translational order whereas orientations are dynamically disordered). Molecules can show an almost free rotation, or they may jump between a restricted number of possible orientations.

Plastic crystals are generally composed by almost spherical objects and, due to their lattice structure, they possess long-range order. Such an order can be seen through the diffraction patterns that present sharp Bragg peaks (that characterize the average ordered structure) and a strong diffuse intensity (that reflects the details of disorder in the system).

1.4 Glasses

The glass transition is a broad phenomenon. Any system that shows a certain degree of disorder can become a glass, arresting a determined degree of freedom in a state far from the equilibrium. This results in a great variety of different types of glass.

Generally when the temperature of a liquid is decreased, the molecules that compose it, begin to arrange themselves in a more regular way, in order to avoid tensions that may arise between the attractive and repulsive forces. In this way, the density increases and volume decreases (except for water) leading the system into a state in which each

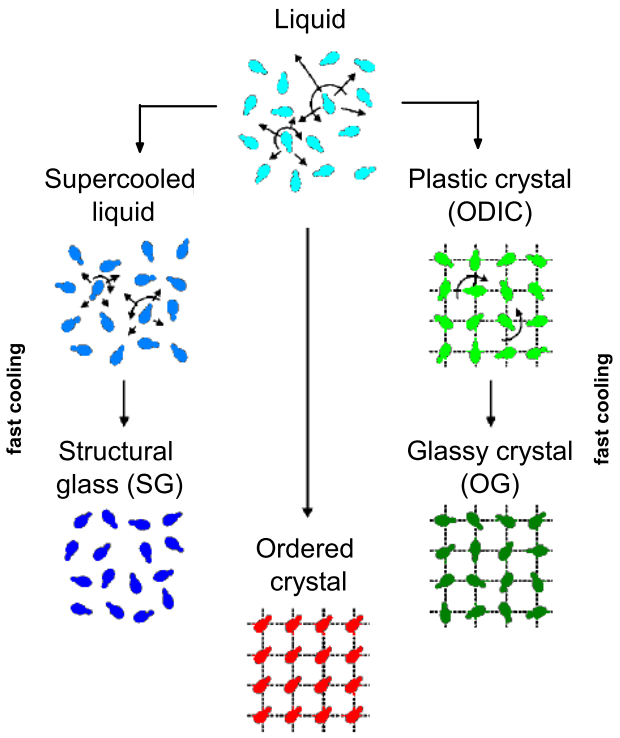

Figure 1.3: Scheme of the possible transitions of a liquid. Depending on the cooling rate it is possible to achieve an ordered structure as a crystal or a glass. Upon fast cooling supercooled liquids arrest their degrees of freedom becoming structural glasses, while plastic crystal, that present only orientational disorder, vitrify in orientational glasses [5].

molecule occupies a precise position in space. At the melting temperature T_m the liquid crystallize, in such case the volume will experience a discontinuous change and then, after further lowering of the temperature, it will contract at slower pace, effect that reflects the fact that the coefficient of expansion of a crystal is generally less than that of the respective liquid (Figure 2.1).

Since the crystallization is a probabilistic process, it is not always possible to obtain an ordered phase. Indeed, for some systems and by means of different methods it is possible to avoid the crystallization also below the melting temperature.

For instance, cooling fast enough a liquid continues to contract at the same pace. The

liquid is now *supercooled* and the state is a metastable equilibrium state which maintains essentially the same structure as above the melting temperature (Figure 1.3). Unlike the liquid state the increase of viscosity in the supercooled region causes a decrease of particle mobility, so that dynamics tends to assume a more cooperative character, separating particles in clusters that exhibit slow and fast movements. Maintaining a fast cooling rate, viscosity and relaxation time continue increasing, due to the slowing down of the dynamics, as long as the system is trapped in a disordered structure (Figure 1.3). The supercooled liquid becomes a *structural glass* (SG) at a temperature T_g, below which the system becomes unstable. It maintains the molecular disorder (orientational and translational) of its liquid phase. Examples of this kind of glass are given by windows glass and optical components.

Even in the case of a plastic crystal, upon a further cooling, molecules exhibit a slowing down of the molecular dynamics until to the point where it is possible to freeze the orientational disorder of the system (Figure 1.3). The new system thus obtained is said *orientational glass* (OG).

Another kind of glasses is given by those materials composed by molecules that present more than one possible conformation. This conformational disorder can be arrested lowering the temperature and so avoiding the switch between the possible molecular conformations and leading to a *conformational glass*. Such disorder is independent from the degrees of freedom related to the orientations or translations of the molecules, that are still able to relax in their equilibrium positions.

1.5 Scientific cases

A brief overview is given here to enumerate the various scientific open questions that have been tackled with the methodology presented in this work. An understanding of the dynamics of the glass formers is central to explain those scientific problems. All cases have been further explained in more detail in Chapter 6, 7 and 8.

1.5.1 Plastic-plastic transition in $C_{10}H_{15}Cl$

In recent years 1-Chloroadamantane (ClA from now on) has attracted great interest because of the importance covered in nanotechnology and pharmaceutical applications. Its plastic phase can be a promising test system for the study of liquids.

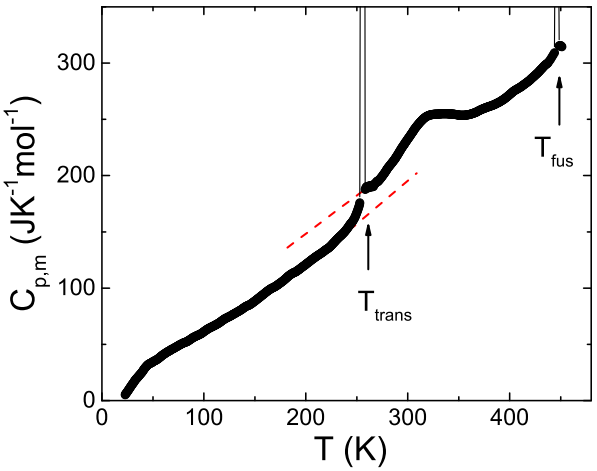

Figure 1.4: Experimental heat capacities of *l*-Chloroadamantane. Phase transition and fusion are observed at $T = 248$ K and $T = 440$ K, respectively. It is evident an anomalous heat-capacity hump around $T \approx 310$ K in the temperature range of plastically crystalline phase [8].

The anomaly (Figure 1.5) evidenced by calorimetric experiments of Kobashi *et al.* within the orientationally disordered phase, and the microscopic dynamics studies of Bée *et al.* [6] motivated us to investigated if there is any change in the structure and/or in the dynamics of ClA within the plastic phase as well as if there is a coupling between dynamical disorder and structure. We fulfill this task, by coupling neutron diffraction (ND) and quasi-elastic neutron scattering (QENS) techniques. Moreover, we have also investigated if it is possible to gain some insight about the dynamics of ClA by using a non-isotropic rotation model originally developed to describe polarization resolved microscopy data [7]. To the best of our knowledge, this model has not been used before for the analysis of QENS data.

1.5.2 High fragility Freon113

Typical strong glass formers (m reaching the minimal value ≈ 16, or $D \geq 100$) are tetrahedral network liquids as SiO_2 or GeO_2. At present the highest values of fragility for organic materials (exception made of polymeric materials) have been found in cis/trans-decahydro-naphthalene (decalin), with $m = 147$ [9].

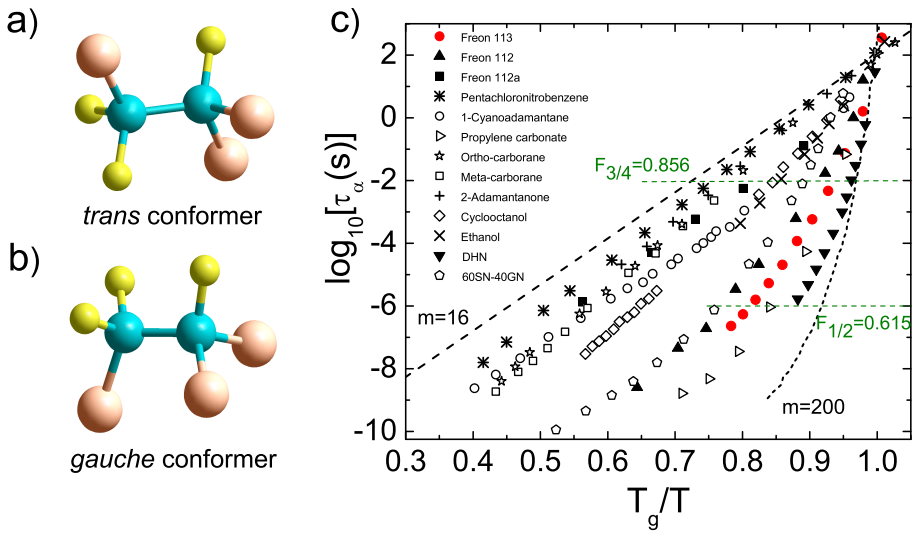

Figure 1.5: (a) and (b) panels show the molecular structure of the two Freon113 conformers. Fragility of Freon113 compared to other plastic crystals and to propylene carbonate, a typical fragile structural glass former. Strong glasses are closer to an Arrhenius behaviour (m = 16) while fragile glasses depart from it

Plastic phases are usually quite strong, *i.e.* the activation energy as a function of the temperature is quite constant. This low sensitivity to temperature changes is usually being related to the suppression of the translational degrees of freedom. In spite of this, Freon113 (1,1,2-trichloro-1,2,2-trifluoroethane, $CCl_2F{-}CClF_2$), has an extremely large fragility closer to that of a canonical glass than that of a plastic crystal.

Hence, a dynamic and thermodynamic study of the orientational glass former Freon113 (1,1,2-trichloro-1,2,2-trifluoroethane, $CCl_2F - CClF_2$) has been performed in order to analyze the kinetic and thermodynamic fragilities. The investigation was carried out by means of dielectric spectroscopy, specific heat measurements and inelastic neutron scattering.

1.5.3 Glycerol dynamics

An understanding of the dynamics of glass-forming liquids at temperatures significantly above the glass transition still represents a coveted goal so as to establish a physical framework to explore the undercooled liquid state. Although we have experimental ac-

cess to the equilibrium states of the liquid at high temperatures, the very nature of glasses makes it impossible to probe these at temperatures below the glass transition. Therefore, if any theory or explanation is to be extrapolated to understand the undercooled regime from knowledge of high-temperature equilibrium states, a consensus must first exists on the underlying physics of the liquid phase at temperatures above the glass transition. Such a consensus remains a challenge to the field, and often the analysis of experimental data is invariably colored by specific theoretical considerations.

The primary aim of this work is to provide a detailed and critical appraisal of quasi-elastic neutron scattering (QENS) data by invoking physical models which are as simple and as general as possible. In doing so, we address to two specific questions about the dynamics of liquid glycerol, a prototypical glass-forming liquid: The first one concerns how many distinct dynamical processes are present in glycerol in the sub-nanosecond (ns) regime. The second one concerns whether a HomoGeneus (dynamically driven, hereafter HG) [10,11] or HeTerogeneous (structurally driven, HT) [12–14] scenario better describes the QENS data. To avoid the common pitfalls associated with "classical" data-analysis procedures (e. g., use of additional parameters not justified by the information content of the data), we make extensive use of Bayesian inference methods.

1.6 Outline of the work

In the present work it is presented a basic but as far as possible general and integrated treatment of the behavior of the disordered phase, mainly directed to the study of molecular dynamics in glass forming materials.

After introducing the required basic theoretical fundamentals, we have paid attention to the investigation methods and the physical models since, despite the great developments in simulations, they are useful to provide a qualitative understanding of molecular motions. The analysis has been performed by means of Bayesian inference, with the attempt to create a robust and transparent method based on probabilistic foundation with which perform a model selection.

Thereafter, the studies on the systems are presented: 1-chloroadamantane, freon113 and glycerol. These three systems present respectively an increasing degree of disorder and have been used to explain some of the dynamical properties of general value. The objectives have been:

- 1**-chloroadamantane**: Give an explanation of the plastic-plastic phase transition by the coupling between dynamics and structure.
- **freon113**: To understand the microscopic origin of the huge fragility value ever seen in plastic crystal analyzing the coupling between dynamics having distinct origins.
- **glycerol**: Investigate the microscopic dynamic of one of most intensive studied viscous liquid, glycerol, comparing two dynamical scenarios.

The analysis of the dynamics of such compound and the method used, that have general validity, could contribute to a deeper comprehension of disordered phase phenomenology.

Part II

Theoretical framework

Chapter 2

Theory of glasses

In order to gain some insight about the glass transition, in this Chapter we give a brief and general description of the theories behind glassy phenomena. A "up to bottom" description will be followed, starting from the macroscopic classification of glasses related to the temperature dependence of their relaxation times, we will go deeper into the microscopic origins of glassy behavior.

2.1 Temperature dependence of relaxation time

2.1.1 Strong and fragile

Lowering the temperature very fast some properties show a dramatic increase, the liquid do not have time to relax to equilibrium and it forms a glass. In the (T, V)-plot (Figure 2.1) this is shown as a deviation from the liquid line settling down in a nearly parallel line to the crystal line.

The glass transition temperature T_g is not a constant characteristic of the material like the melting temperature, but it is a "dynamic" temperature that depends on the cooling rate: faster the cooling rate, higher the T_g value. Thus glassy state is not a well-defined state but depends on the temperature (and pressure) history. The fact that T_g is dependent from the cooling rate has been verified by experiments [15, 16], but until the cooling rate is in the range $0.1 - 100$ K/min, the variation of T_g is not so meaningful. Furthermore, since in such state the viscosity reaches very high values, the glass transition temperature is generally defined by $\eta(T_g) = 10^{12}$ Pa s.

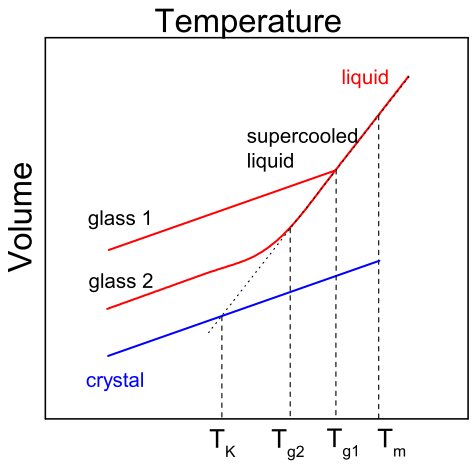

Figure 2.1: Schematic illustration of measured property of liquid. Decreasing T liquid can crystallize (blue line) with a dramatic decrease of the volume, or, depending on the cooling rate, it can vitrify (red lines). Since T_g value depends on the cooling rate, a liquid can follow the "glass 1" path or, cooling it more slowly, the system might follow the "glass 2". T_g is the temperature at which, on cooling, there is the departure from the equilibrium liquid line.

It is useful, however, to give a more general definition based on relaxation time τ. As we know, the relaxation time τ shows a sharp increase when we get close to the dynamic glass transition T_g. By definition, τ is finite at T_g; in fact, T_g is defined as the point where relaxation time is of order $10^2 - 10^3$ s, which is finite.

Usually for most liquids at high temperatures the mechanism of relaxation is ruled by a simple Arrhenius behavior of the relaxation time τ,

$$\tau = \tau_0 \exp\left(\frac{E_a(T)}{k_B T}\right) , \tag{2.1}$$

in which the activation energy E_a is essentially temperature independent.

However, in some cases, the increase of the relaxation time is steeper with respect to the purely Arrhenius behavior. As the temperature is decreased the relaxation time often shows a stronger increase than that followed by the Arrhenius law, thus making the associated activation energy to significantly increase when approaching the glass transition T_g. Such phenomenon is usually viewed as resulting from a significant increase of some characteristic cooperativity relaxation length. A solid nonlinear formula that

interpolates equilibrium data above T_g when approaching T_g is then necessary. It turns out that such formula, found independently from any theoretical framework, is the Vogel-Fulcher-Tamman (VFT) law. For the relaxation time, it can be written:

$$\tau = \tau_0 \exp\left(\frac{D \cdot T_0}{T - T_0}\right) , \tag{2.2}$$

where the temperature T_0 is associated with an ideal glass transition and D is the strength parameter.

The rise up of the relaxation time or, similarly, the viscosity increase, is generally characterized by recourse to the concept of fragility [17, 18]. The fragility index, m, which has been used to classify glass former materials and accounts for such a deviation of the Arrhenius temperature dependence, is defined as:

$$m = \left[\frac{\partial \log \tau}{\partial (T_g/T)}\right]_{T=T_g} . \tag{2.3}$$

Those materials for which their characteristic relaxation times τ follows an Arrhenius law are known as "strong" glass formers, whereas "fragile" glass formers are those which exhibit super-Arrhenius behavior and therefore τ increases much faster with decreasing temperature in such a way that the activation energy increases with decreasing temperature when approaching T_g (see Figure 2.2). The fragility index m is a fundamental parameter of the relaxational behavior of glass formers and it is used to classify the slowing down of the dynamics, by measuring the deviation from the Arrhenius behavior. Small values of the fragility m describe *strong* liquids, whereas larger values of m indicate that the liquid is *fragile*.

The term fragile indicates how "abrupt" is the glass transition. Since in fragile liquids it is quite easy to arrest one or more degrees of freedom, they are affected by the increase in viscosity and relaxation time in a very narrow temperature range, for this reason they are better glass formers with respect to strong materials [19].

The VFT formula seems reasonable also without providing any theoretical argument. Its exponential nature agrees quite well with the very physical idea that activation rules the dynamics at low temperatures [19]. Furthermore, the non-Arrhenius exponent characterizes the difference between strong and fragile materials: by varying the parameter T_0 we can distinguish between the Arrhenius behavior that describes strong liquids ($T_0 \approx 0$), to a steeper rise of τ (T_0 increases) that is typical of fragile glass formers.

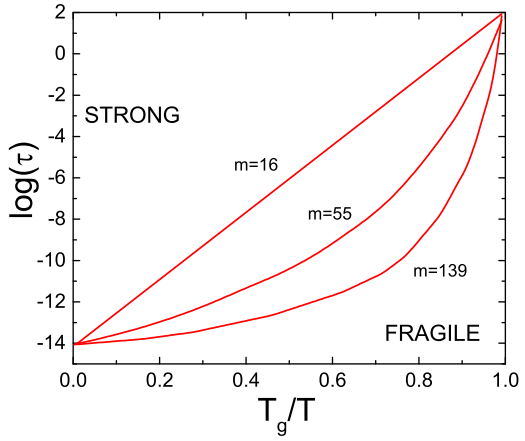

Figure 2.2: Angell plot showing the temperature dependence of the logarithmic relaxation time τ. The representation is normalized to the glass transition temperature T_g and it is normally used to distinguish materials in strong (Arrhenius behavior) and fragile (super-Arrhenius behavior). Strong materials show smaller values of the fragility index, whereas fragile materials have bigger values of it.

In conclusion it is useful to note the relation that exists between the strength parameter D and the fragility parameter m:

$$m = \frac{D \cdot T_0}{\ln(10 \cdot T_g)} \cdot \left(1 - \frac{T_0}{T_g}\right)^{-2} . \tag{2.4}$$

2.1.2 Adam-Gibbs theory

Focusing the attention on the entropy it is possible to see that the entropy of the liquid decreases faster with respect to the entropy of the crystal. This seems to be obvious since

$$\frac{dS}{dT} = \frac{C_p(T)}{T} \tag{2.5}$$

where the specific heat, $C_p(T)$, of a liquid is larger than that of a crystalline solid. The *excess entropy* is then defined as the difference between the liquid and the crystal entropy:

$$\Delta S_{exc}(T) = S_{liq}(T) - S_{cryst}(T) . \tag{2.6}$$

Such a quantity decreases lowering the temperature. Plotting $\Delta S_{exc}(T)/\Delta S_{exc}(T_m)$ vs T/T_m, as shown in Figure 2.3, we can notice that for some systems the excess entropy

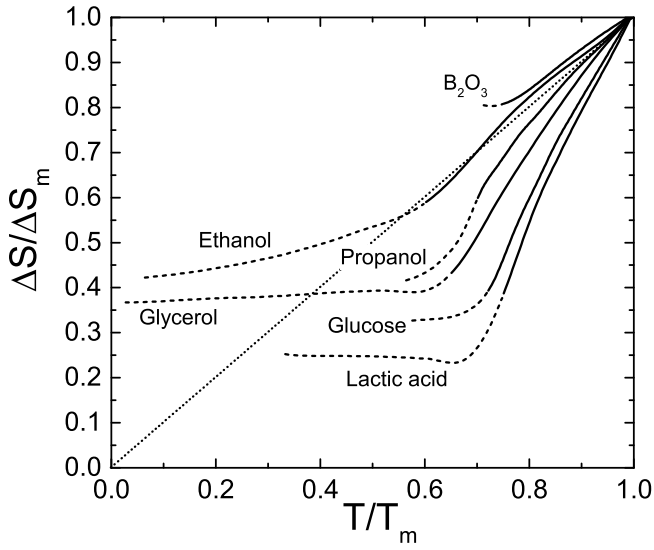

Figure 2.3: Excess entropy of some substances, scaled by their values at melting temperature. For each sample the excess entropy seems to disappear at a non-zero temperature T_K [20].

vanishes at a determined temperature. This temperature is called Kauzmann's temperature, T_K (see Figure 2.1), and it is defined as the temperature for which $\Delta S_{exc}(T_K) = 0$.

For some compounds T_K is finite and this suggests that, at $T < T_K$, the entropy of the supercooled liquid would be lower than the entropy of the stable crystal counterpart. This phenomenon is known as Kauzmann's paradox or entropy crisis.

The entropy of a liquid, S_{liq} in eq. (2.6), can be divided in two contributions: a vibrational contribution corresponding to the short-time vibrational dynamics, and a configurational contribution related to the position of its constituent particles

$$S_{liq} = S_{vib} + S_c \ . \tag{2.7}$$

Since the vibrational part is not so different from the vibrational entropy of the crystal, we can assume $S_{cryst} \approx S_{vib}$, and then

$$\Delta S_{exc}(T) = S_{liq}(T) - S_{crys}(T) \approx S_c(T) \ . \tag{2.8}$$

Hence the excess entropy is approximately equal to the configurational entropy. In a supercooled liquid S_c decreases when the temperature is lowered [19].

On these thermodynamic grounds we can write the temperature dependence of relaxation time τ using the so called Adam-Gibbs equation:

$$\tau = \tau_0 \exp\left(\frac{C}{TS_c(T)}\right) , \tag{2.9}$$

where C is a constant factor. Equation (2.9) shows that the relaxation time increases when the configurational entropy decreases. The exact behavior of $S_c(T)$ at low T is unknown, however, using eq. (2.5) and (2.8), we can write:

$$\frac{dS_c}{dT} = \frac{d}{dT}(S_{liq} - S_{cryst}) = C_p^{liq} - C_p^{cryst} = \Delta C_p , \tag{2.10}$$

hence

$$S_c(T) - S_c(T_K) = \int_{T_K}^{T} dT \frac{\Delta C_p}{T} . \tag{2.11}$$

The difference in the specific heat between the liquid and the crystalline phase is temperature independent. Using such approximation and the fact that $S_c(T_K) = 0$ it is possible to write for $S_c(T)$:

$$S_c(T) = \Delta C_p \log\left(\frac{T}{T_K}\right) \qquad \text{expanding for } T \approx T_K \qquad S_c(T) \approx \Delta C_p \frac{T - T_K}{T_K} . \tag{2.12}$$

The configurational entropy is then proportional to the crystal-liquid difference of the specific heat ΔC_p. Approaching the dynamical glass transition, *i.e.* going towards T_g, the specific heat value of the glassy phase becomes comparable to the value of the respective crystal. Therefore, as expressed by eq. (2.12), the higher is the change in the specific heat, the steeper is the configurational entropy decrease. Combining eq. (2.12) and eq. (2.9) one obtains:

$$\tau = \tau_0 \exp\left(\frac{T_K}{\Delta C_p T(T - T_K)}\right) \qquad \text{and near } T_K \qquad \tau = \tau_0 \exp\left(\frac{A}{T - T_K}\right) , \tag{2.13}$$

that is a VFT relation. This thermodynamic fragility is correlated to the excess entropy S_{exc} (the excess of liquid entropy over that of the crystal, that is generally taken as the configurational entropy S_c [21] which appears in the Adams-Gibbs equation (eq. 2.9)), scaled by the excess entropy at T_g, $S_{exc}(T_g)$. Such thermodynamic "Angell plots" (i.e., T_g-scaled Arrhenius plots) $S_{exc}(T_g)/S_{exc}(T)$ vs. T_g/T (Figure 2.4) exhibited a very similar behavior to that of classical Angell plots of the viscosity or relaxation time, $\log\tau$ vs. T_g/T, for many glass-forming systems [22].

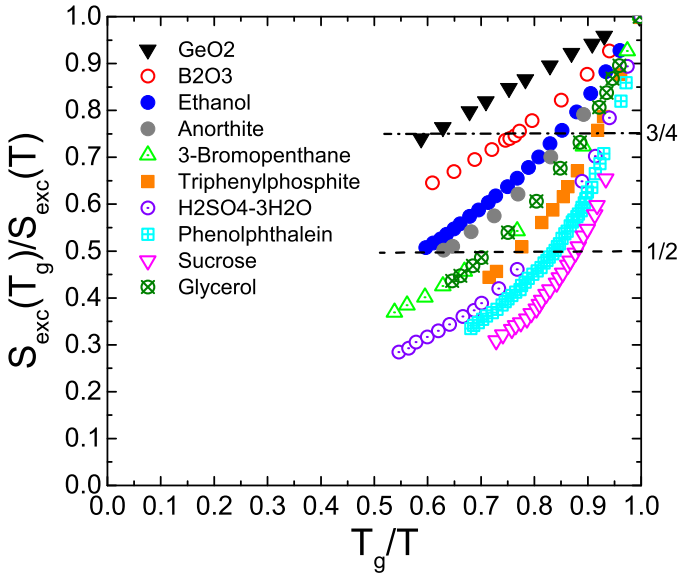

Figure 2.4: Excess entropy vs. T_g-scaled temperature plots. The form is similar to that of Figure 2.2. The lines drawn at the 1/2 and 3/4 marks are used to obtain thermodynamic fragilities $F_{1/2}$ and $F_{3/4}$ for comparison with the kinetic quantities. The $F_{3/4}$ is preferable, since it does not require any data extrapolations (for strong liquids) for its determination [22].

2.1.3 Dynamic and thermodynamic fragility

The relation between kinetic fragility, that describes the temperature dependence of transport coefficients in viscous liquids, and thermodynamic fragility has been object of several studies [22–26]. Thermodynamic fragility has been defined [26] in terms of the temperature dependence of the excess entropy, scaled by the excess entropy at T_g and compared to the kinetic one.

First of all we have to notice that the Vogel temperature T_0, where viscosity or relaxation time extrapolate to infinity by the VFT formula, and the Kauzmann temperature T_K, where the supercooled liquid entropy extrapolates to the crystal entropy, are not quantities directly measured, in fact, one is a parameter coming from a fit procedure (T_0) and depends on the temperature interval over which the fitting is performed, and the other (T_K) is the result of a linear extrapolation of the data where the excess entropy vanishes (remember that the configurational entropy is not exactly equal to the

excess entropy).

Despite the singularities in T_0 and T_K discussed above, in many systems it is possible to consider [21, 27]:

$$T_0 \approx T_K \ . \tag{2.14}$$

This relation establishes a deep connection between two different frameworks: dynamics (relaxation time) and thermodynamics (configurational entropy). Thus, the point in which the dynamic divergence in the VFT fit is expected can be approximate to the point where the configurational entropy vanishes.

To have a quantitative comparison between the two scenarios a definition of the two fragilities has to be given. Using the Angell plot $log\eta$ vs T_g/T, for the *kinetic fragility* we have,

$$F_{1/2} = 2\frac{T_g}{T_{1/2}} - 1 \ , \tag{2.15}$$

where $T_{1/2}$ is defined as the temperature half way between 10^{13} Pa s (or 10^2 s for the relaxation time) characteristic of the glass transition, and 10^{-4} Pa s (or 10^{-14} s), the common viscosity high-temperature limiting value for liquids. In the same way, a *thermodynamic fragility* $F_{1/2}$ could be defined from the above mentioned $S_{exc}(T_g)/S_{exc}(T)$ normalized curves. Nevertheless, it was argued that for the thermodynamic fragility is preferable to use the $T_{3/4}$ line (the temperature at which $S_{exc}(T_g)/S_{exc}(T) = 3/4$) to avoid the need for too large extrapolations in the case of strong liquids

$$F_{3/4} = 2\frac{T_g}{T_{3/4}} - 1 \ . \tag{2.16}$$

As shown in Figure 2.5 and despite some exceptions, the fragilities of many substances exhibit a correlation between the kinetic and the thermodynamic part.

2.2 Energy landscape

We have seen how phenomena that take place in glassy compounds can be reproduced by means of simple models starting from basic notions. However, such description is limited to the search for the fundamental mechanisms behind the slowing down of the relaxation and the fall out of equilibrium of the slow degrees of freedom that induce the glass transition. Those models are very helpful, because provide a link between dynamics and glassy behavior, but they are not able to explain how these mechanisms

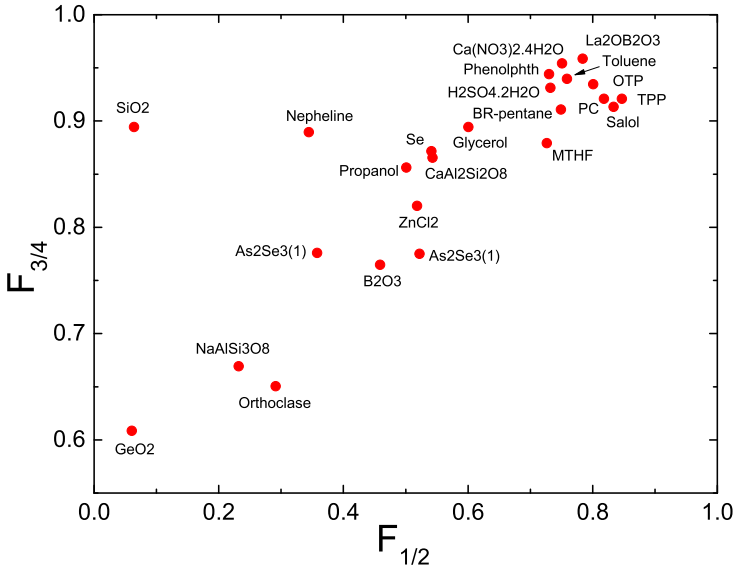

Figure 2.5: Correlation between the thermodynamic $F_{3/4}$ and kinetic $F_{1/2}$ fragility for some compounds [22].

arise in real systems, such as, for example, the origin of energy barriers that give rise to Arrhenius and super-Arrhenius character near T_g or the origin of stretched exponential dynamics [28].

An attempt to give an explanation has been done putting the attention on how the system evolves in the phase space, *i.e.* the space of all configurational degrees of freedom [19]. This space, for a glass former system is complicated, for example, considering a system composed by N particles of the same chemical species, with ν that is the number of internal degrees of freedom of each particle (orientation, conformation, etc.), then the dimension of the space will be $(3+\nu)N+1$ [29]. Over the phase space can be defined the potential energy of the system, which a surface is called *potential energy landscape*. Each one of the system configurations may be represented as a point, that, moving on the surface of the potential energy landscape determines the system dynamics.

The potential energy hypersurface presents local minima that correspond to equilibrium sites of the system. The absolute minimum (ground state) describes, of course, the crystalline state, but there are also all the minima due to defects and dislocations

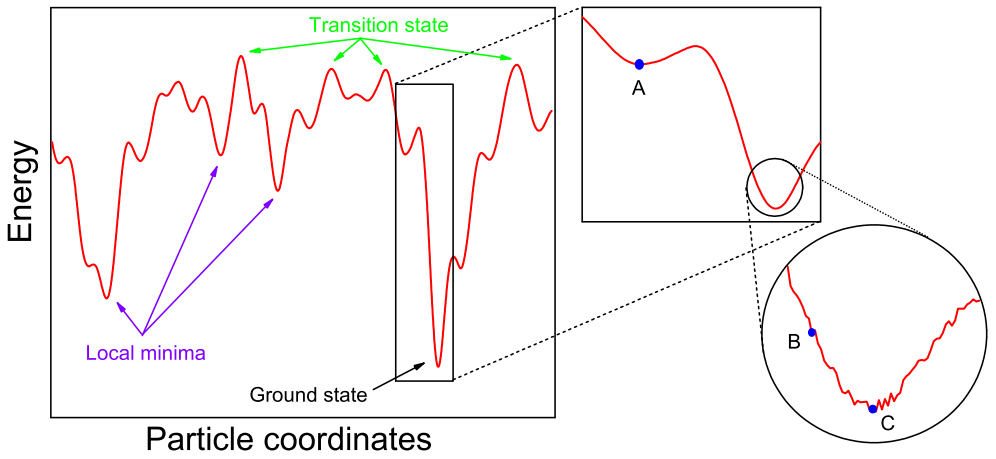

Figure 2.6: 2D representation of a potential energy landscape for a N-particle system. Absolute minimum corresponds to the crystal phase, while local minima correspond to the amorphous and glassy state. In right panels an enlargement of the energy landscape. The three points A, B and C correspond to: a metastable equilibrium state, an unstable state out of the equilibrium and to a stable equilibrium state, respectively [29].

of the crystal, which can be seen as excitations with respect to the ground state. More interesting is the presence of others local minima, which describe the amorphous and glassy state (lack of long-range order), and show a potential energy higher than the crystal one.

The main idea of this approach is that at low temperatures a supercooled liquid examines the phase space through jumps, overcoming barriers of potential energy that separate different amorphous minima. The system does not perform, however, such jumps in the attempt to reach lower minima, moreover we are considering a system at equilibrium (although metastable), so that the average potential energy, where the system is located, is constant in time. The system goes through minima that on average have the same energy, resulting in equilibrium and therefore ergodic. A system is said to be ergodic, when it has the same behavior if averaged over time or averaged over the phase space, *i.e.*, that all accessible microstates are equiprobable over a long period of time.

At the glass transition temperature T_g, the system is blocked in a local minimum of

the phase space, hence it cannot explore the phase space in the available time. In this case the barrier cannot be surpassed, for that, once a system is trapped within a local minimum it cannot escape and ergodicity is broken.

The potential energy landscape scenario offers a description in terms of two time scales: a short time due to the vibrational relaxation within a potential energy minimum, and a long time relaxation due to the transition between one minimum to another. Since the jumping time becomes larger lowering the temperature, the second time scale is longer than the vibrational one. The short and the long time scale can be seen respectively as the β (fast) and α (slow) relaxation of the dynamic correlation function. Considering such interpretation, vibrations in the potential energy minimum of the phase space correspond to vibrations of particles within the confinement formed by neighbors, whereas passing a barrier corresponds to the local diffusion of some particles [19].

2.3 Two step relaxation

The nature of glass transition is purely dynamical, in particular, close T_g, the beginning of glass transition is marked by the behavior of viscosity, that is the time integral of a dynamic correlation function, called shear relaxation function. The same happens with the diffusion coefficient, linked to the integral over time of the velocity-velocity correlation function. The correlation function $C(t)$ shows how rapidly correlations into the system decay in time [19]. A short-time ballistic regime is expected at high temperatures, in which particles move freely, followed by a dissipative regime, described by a normal exponential relaxation:

$$C(t) = C_0 \exp(-t/\tau) \ . \tag{2.17}$$

where τ is the only relaxation time in describing the system.

However, decreasing T the relaxation time τ grows precipitously, and the decay of $C(t)$ emerges approaching T_g. If the increase of τ with decreasing T was the only effect, there would be no signal which characterizes the approach to the glass transition. But it is not what happens. Approaching T_g a plateau is formed, hence the decay is not described by a simple exponential correlation function (Figure 2.7). This kind of behavior is called two step relaxation.

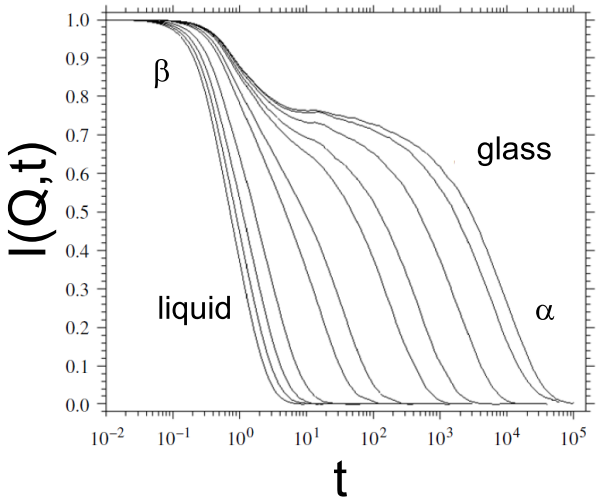

Figure 2.7: The dynamic correlation function $C(t)$ (in this case $C(t)$ is the incoherent intermediate scattering function $I(Q,t)$). Lowering the temperature, and approaching T_g the simple exponential decay changes in a two step relaxation [19].

Two steps relaxation is the evidence of the approach to the glass transition. At low temperatures the relaxation time increases, but only through the non-exponential dynamic correlation function which one has the evidence of the proximity of the glass transition. Furthermore, the presence of the plateau suggests a description based on two time scales: a fast and a slow process. The former has a weak dependence on T, whereas the latter is strongly dependent on temperature. The two processes are said β (fast process) and α (slow process) relaxation.

The shape of $C(t)$ suggests a clearly division between two time scales, separation that becomes more evident lowering the temperature. Important to notice that it is not possible to define a temperature at which begin the non exponential relaxation behavior. Thus the transition between the simple exponential and the two step relaxation can be seen as continuous.

It is possible to visualize such effect imagining a particle confined by its neighbors. The surrounding particles behave as a “cage”. Approaching the glass transition, the viscosity increases and reduces the space available to the movements of each particle. Thus the particle that is trapped will perform movements in the confined region until

the cooperation of the surrounding neighbors permit to break the cage and let the particle to diffuse. β relaxation is linked to the bouncing modes in the confined region, and α relaxation is related to the diffusion. Upon cooling the relaxation time of a liquid increases as well as the correlation length. Near T_g, particles have the tendency to form clusters showing then an heterogeneous dynamics due to their cooperativity.

2.4 Homogenous or heterogeneous?

The departure of the dynamic correlation function from exponential relaxation can be ascribed to the decay split into two steps. Evidence suggests that the Kohlraush-Williams-Watts stretched exponential form,

$$C(t) = C_0 \exp\left[-(t/\tau)^{\beta_{KWW}}\right] \ , \qquad \beta < 1 \tag{2.18}$$

fits reasonably well the data. The stretched exponent β_{KWW} is a parameter that can be used to determine the cooperativity of the many-body relaxation dynamics. The interesting point is that the exponent decreases lowering the temperature, emphasizing a clear deviation from a simple exponential relaxation behavior. However, at high values of T the exponent β_{KWW} approaches 1, and the relaxation returns to a simple exponential.

The microscopical origin of the non-exponential relaxation is not fully understood. Two generally accepted hypotheses are usually given: the homogeneous and heterogeneous scenarios. According to the first, relaxation is non-exponential in all the regions of the material, so that the stretched behavior of the correlation function is given to a proper phenomenon, also locally, due to the disordered environment that molecules see around themselves. For the heterogeneous view, on the other hand, the whole system is stretched because different domains have significantly different relaxation times, and in this sense dynamics is considered heterogeneous. These spatial heterogeneities [29] correspond to different regions distant few nanometers each other. Measuring the global relaxation time, typically an average over different domains is performed, and a global non-exponential decay is obtained.

It is believed that the heterogeneous dynamics is the basis of a phenomenon that takes place at low temperatures. This phenomenon is the breakdown of the Stokes-Einstein (SE) relationship between the viscosity and the diffusion coefficient.

$$D\eta = \frac{k_B T}{Cd} \ , \tag{2.19}$$

where C is a constant and d is the hydrodynamic effective diameter of the molecule. In supercooled liquids close to T_g, the diffusion coefficient D and $1/\eta$ have different functional dependence on T, so that the ration $D\eta/T$ is no longer a constant and the Stokes-Einstein relation is violated [30, 31].

A detailed explanation is given in [32]. Being the dynamics heterogeneous, the diffusion is driven by the fast clusters, while structural relaxation by the slow ones. Thus, at low T, diffusion and relaxation decouple, and the SE relation is broken.

Imaging now a simple system in which there are only two kinds of domains (fast and slow), in which diffusion coefficients and relaxation times are respectively $D_f >> D_s$ and $\tau_f << \tau_s$ [19]. In general it is possible to assume $\tau \approx \eta$, so that SE relation reduces to $D \approx 1/\tau$. The diffusion coefficient and relaxation time of the whole system are then given by,

$$\tau = \frac{\tau_f + \tau_s}{2} \approx \frac{\tau_f}{2} \ , \qquad D = \frac{D_f + D_s}{2} \approx \frac{D_f}{2} \ . \tag{2.20}$$

Hence,

$$D >> \frac{1}{\tau} \ , \tag{2.21}$$

so that the SE relation is violated: diffusion increases with respect the structural relaxation. The explanation is clearly oversimplified, but it gives a basic idea of this phenomenon in a supercooled liquid.

Furthermore, measurements of various substances have shown the link between the SE relation and the nature of the non-exponential decay of the dynamic correlation function [32]. When the stretched exponent β_{KWW} decreases the deviation from the SE relation becomes bigger. It is then quite evident the connection between β_{KWW}, the dynamical heterogeneities and the SE equation.

Part III

Experimental methods

Introduction

In this part an overview of the most important theoretical relations relative to the experimental techniques generally used for the analysis of soft materials will be given. We will focus on the techniques used in the development of this thesis, in particular, we will take into account neutron scattering and dielectric relaxation techniques. The discussion will be followed by a brief description of how such formulas are connected to the physical quantities measured in our experiments.

Given the complexity of the dynamics and the structure in the materials under examination, we wish to emphasize the complementarity between the techniques discussed here, and that it is crucial to combine information from several of these techniques to fully understand the underlying mechanisms of molecular motions [33] and eventual connections with their structure. For a deeper description on the basics of neutron scattering and diffraction and dielectric spectroscopy, we refer the reader to a wide range of literature on theory [34–41] and on instrumentation [35, 40–44].

Figure 2.8 presents a traditional view of the time (frequency) range accessible to different techniques. It is important to note that scattering techniques have a significant advantage due to an additional variable - the scattering angle. It provides information on the geometry of the motion through the measurements of the scattering wavevector Q. Thus, in Figure 2.8, the lengthscale ($\approx 2\pi/Q$) accessible to experimental techniques is shown as the x-axis. Dielectric relaxation spectroscopy has no particular Q, and that is the reason it is outside of the main sketch presented in Figure 2.8.

Furthermore, it is important to note that the way in which it is possible to get information about the sample under analysis depends on the type of instrumentation which is used. Considering that there are many types of instruments and of possible configurations for each instrument, the use of a particular machine and therefore of a

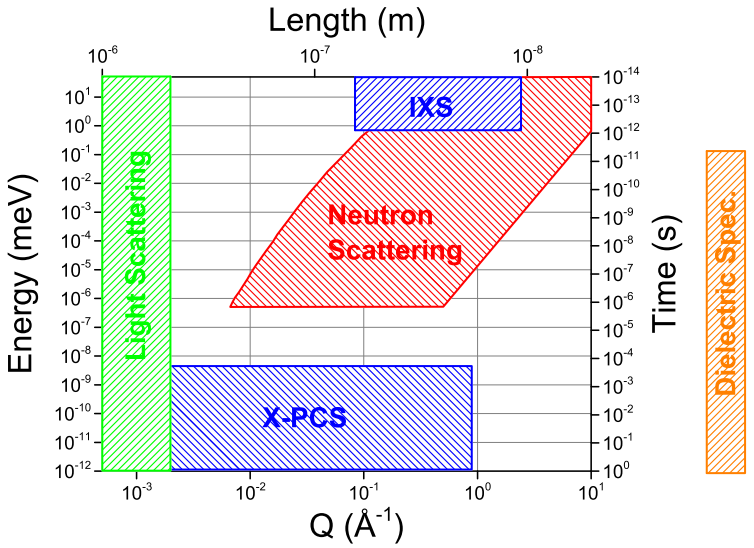

Figure 2.8: Sketch showing the frequency (time) and wavevector (length) ranges accessible with traditional experimental techniques. Longer times (not shown) can be accessed by many techniques. IXS is Inelastic X-Ray Scattering and XPCS is X-ray Photon Correlation Spectroscopy. Dielectric relaxation spectroscopy does not have a particular length scale (Q), thus is placed outside of the main plot

particular technique of investigation delimits the length and the time scale that it is possible to probe in the analyzed systems.

The main features about the instruments will be presented, paying particular attention to the functioning of the instruments used for subsequent analysis.

Chapter 3

Neutron scattering

3.1 Neutron scattering principles

The properties of neutron make it particularly suited for the study of matter. The absence of charge implies that the interaction between neutrons and matter is confined to short range, so that the neutron can penetrate deep into the sample. The wavelength associated with the neutron is on the same order of magnitude of inter-atomic distances of solids and liquids. This tells us that neutrons are particularly suited to the study of the structure by means of diffraction experiments. Moreover, neutrons have an associated kinetic energy, $k_B T$, on the order of 25 meV, which is a typical energy for collective excitations in solids and liquids. Therefore, both wavelength and energy are ideally suited to studies of the atomic dynamics of condensed matter by means of spectroscopy technique.

Let us consider an ideal neutron scattering experiment in which a monochromatic beam of neutrons, characterized by the wavevector $\mathbf{k_i}$, impact on a target (Figure 3.1). During the collision the incident neutrons can exchange momentum and energy with the sample. The change of direction and module of the wavevector, before and after the diffusion process, is related to an exchange of momentum between the neutron and the sample, conventionally described in terms of the transferred wavevector $\mathbf{Q}$. The law of momentum conservation is therefore:

$$\mathbf{Q} = \mathbf{k_i} - \mathbf{k_f} \ . \tag{3.1}$$

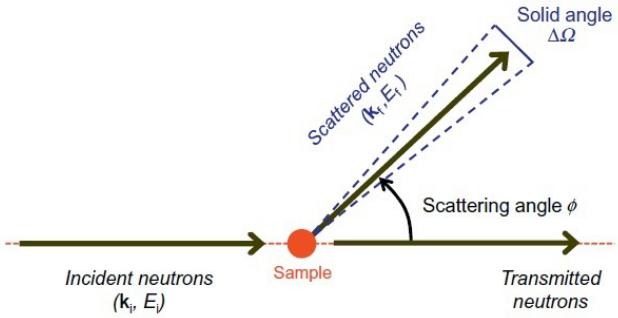

Figure 3.1: Schematic diagram of a generic arrangement for neutron-scattering experiments [36].

Generally the change in modulus of the vector $\mathbf{k}$ is related to an exchange of energy between the neutron and the sample, whose conservation law can be written:

$$\frac{\hbar^2 {k_i}^2}{2m_n} - \frac{\hbar^2 {k_f}^2}{2m_n} = \hbar\omega, \tag{3.2}$$

where $\hbar\omega$ is the transferred energy. By analyzing the (3.1) and (3.2) it is possible to notice that $\mathbf{Q}$ and ω result to be not independent and determine a cinematic constriction on the diffusion experiment. In fact the space ($\mathbf{Q}$, ω) is not fully accessible, as can be seen rewriting (3.1) in the following way:

$$Q^2 = {k_i}^2 - 2k_i k_f \cos\theta + {k_f}^2 \ . \tag{3.3}$$

Neutron scattering is considered *elastic*, when the neutron does not change its energy in the scattering process ($E_i = E_f$). If neutrons either gain ($\hbar\omega < 0$), or lose energy ($\hbar\omega > 0$) in the scattering process, the scattering is said *inelastic*.

3.1.1 What do we measure?

What we measure is the ratio of the neutrons scattered in a certain time interval and the incidents neutrons during the same time interval. So, we can count the neutrons which are diffused into a solid angle element $d\Omega$ around a final wave vector $\mathbf{k_f}$ and with a final energy between E_f and $E_f + dE_f$. This amount is:

$$\frac{d^2\sigma}{d\Omega dE_f}\, d\Omega dE_f \ , \tag{3.4}$$

where the quantity $d^2\sigma/d\Omega dE_f$ is called *double differential cross section.*
A physical comprehension of eq. 3.4 can be given in the following way: we know that, when the incident neutron has a wavelength comparable with the interatomic distances that characterize the structure of the sample, the neutron will undergo a deviation in its direction. Furthermore, a neutron passing through a sample can gain or lose energy, creating or annihilating movements within the material itself. If we are not interested in such movements, one can eliminate the energy dependence by integrating over all possible final energies E_f getting:

$$\frac{d\sigma}{d\Omega} = \int \frac{d^2\sigma}{d\Omega dE_f}\, dE_f \ , \tag{3.5}$$

that is called *differential cross section.* Hence $d\sigma/d\Omega$ depends in an integral way on the dynamics of the system but does not disclose a detailed information about the motions. Similarly, a *total scattering cross section* for the system under investigation is defined by:

$$\sigma_T = \int \frac{d\sigma}{d\Omega}\, d\Omega \ , \tag{3.6}$$

which can be measured in a simple transmission experiment. This observable depends only on k_i, and contains less information about the structure and dynamics of the sample with respect to $d\sigma/d\Omega$.

3.2 Scattering law

An incident neutron, passing near a nucleus of the sample, is subject to three distinct events. The neutron can be transmitted, without any kind of interaction, absorbed and so trapped by the nucleus or scattered. In the last case its direction as well as its energy are changed [35, 45] and can be measured placing a detector along the direction $\mathbf{k_f}$. To describe the interaction between neutrons and nuclei, we need to use formalism that comes from the quantum-mechanical theory of scattering.

In order to obtain information on the sample, from neutron scattering, we need to define a general expression of the double differential cross section for a given system transition from one quantum state to another, namely by the initial states $|\lambda_i\rangle$ of the sample and those $|\mathbf{k_i}\rangle$ of the neutron to the final states of the sample, $|\lambda_f\rangle$, and of the neutron, $|\mathbf{k_f}\rangle$. For a complete discussion we should describe the initial and final states of neutron also from a state of spin (respectively $|\sigma_i\rangle$ e $|\sigma_f\rangle$).

Since the aim of this analysis is not study magnetic characteristics of the sample, this aspect was not taken into account: measures were carried out with non-polarized neutrons and it is therefore used a system of detection and analysis that is not sensitive to polarization. In this case the potential of interaction is spin independent.

By summing over all possible final states λ_f of the sample, and doing an average for the initial states with probability p_λ, we obtain the following final expression for the double differential cross section:

$$\begin{aligned}\frac{d^2\sigma}{d\Omega dE_f} &= \frac{1}{\hbar}\frac{d^2\sigma}{d\Omega d\omega} = \\ &= \frac{1}{N}\frac{k_f}{k_i}\left(\frac{m_n}{2\pi\hbar^2}\right)^2 \sum_{\lambda_i} p_\lambda \sum_{\lambda_f} \overline{|\langle \mathbf{k_f}\lambda_f|\hat{V}|\mathbf{k_i}\lambda_i\rangle|^2}\delta(\hbar\omega + E_{\lambda_i} - E_{\lambda_f}) \ ,\end{aligned} \tag{3.7}$$

where $\hat{V}$ is the Fermi's pseudopotential and the δ-function is included to ensure the energy conservation. The Fermi's pseudopotential depends by instantaneous positions of the neutron and the nucleus respectively $\mathbf{r}$ and $\mathbf{R}$, and by b, the *scattering length*. The scattering length depends on the interaction, varies depending on the spin state of the neutron-nucleus system and its sign and its intensity vary irregularly with the atomic number and the mass number of the diffuser atom (see Figure 3.2).

Assuming that the isotopic and spin distributions, referred to the same type of atomic element, are random, is possible to mean simply on the initials distributions, we get:

$$\frac{1}{\hbar}\frac{d^2\sigma}{d\Omega d\omega} = \frac{1}{N}\frac{k_f}{k_i}\frac{1}{2\pi\hbar}\int \sum_{d,d'}\sum_{j,k\in d,d'} \overline{b_j^* b_k}\left\langle e^{-i\mathbf{Q}\cdot(\mathbf{R}_j(0)-\mathbf{R}_k(t))}\right\rangle e^{-i\omega t}dt. \tag{3.8}$$

where d and d' refer to the case of a multi-component sample (in the case of a single component system, $d = d'$ and we can omit the sum over d and d'), $\mathbf{Q} = \mathbf{k_i} - \mathbf{k_f}$ is the transferred wavevector and $\omega = (E_i - E_f)/\hbar$ is the transferred energy between the probe and the sample.

3.2.1 Coherent and Incoherent

We need to evaluate $\overline{b_j^* b_k}$ which is the average of the scattering lengths done on the isotopic and spin distributions, varying on all the corresponding pairs of atoms d and d'. Therefore we can write:

$$\overline{b_j^* b_k} = \overline{b_d^* b_{d'}} + \left(\overline{|b_d|^2} - |\overline{b_d}|^2\right)\delta_{jk}\delta_{dd'} \ , \tag{3.9}$$

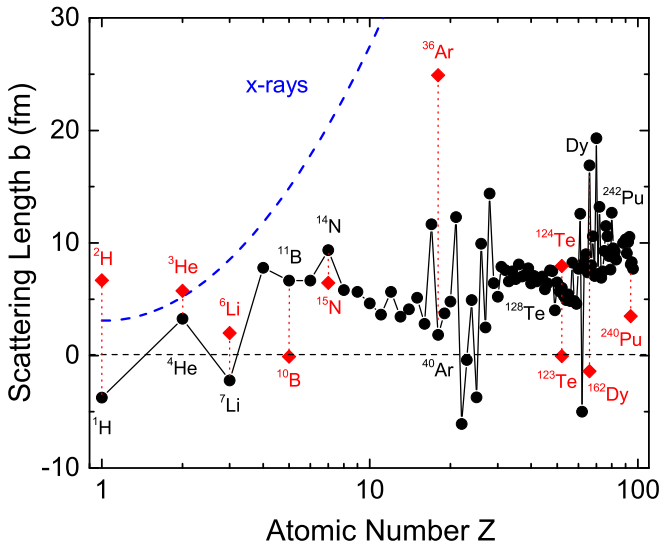

Figure 3.2: Scattering lengths along the periodic table for neutrons (full black circles and full red squares) and X-ray (dashed blue line). The black symbols describe the value of the most abundant isotope for a given element, while red squares correspond to scattering lengths for a specific isotopes. The X-ray values presuppose electrically neutral elements (i.e., Z=number of electrons).

.

the substitution of (3.9) in (3.8), provides:

$$\frac{1}{\hbar}\frac{d^2\sigma}{d\Omega d\omega} = \frac{1}{N}\frac{k_f}{k_i}\sum_{d,d'}\overline{b_d^* b_{d'}}\sum_{j,k\in d,d'} S_{jk} + \frac{1}{N}\frac{k_f}{k_i}\sum_{d}\left(\overline{|b_d|^2} - |\overline{b_d}|^2\right)\sum_{j\in d} S_j \ , \qquad (3.10)$$

The first term in (3.10) is the sum, over all possible pairs of atoms j and k, of the correlation between the position of the atom j at time $t = 0$ and that the atom k at time t. This therefore represents a term of interference and it said *coherent cross section*. The second term, instead, is the sum of self-correlations of each individual atom between its position at the initial instant and the one at time t; that term is said *incoherent cross section*.

Let's give an interpretation to the definitions introduced above for a single component system: since the scattering length, b, varies depending on the isotope and depends on the orientation of the nuclear spins, the potential of which is affected by the probe is not uniform, but changes from one atom to another. Therefore, only the average

potential ($\propto |\overline{b_d}|$) can give interference effects and give rise to coherent scattering. The changes from the average potential, instead, are random and do not give rise to interference phenomena. This is incoherent scattering which is therefore proportional to the mean square deviation ($\overline{|b_d|^2} - |\overline{b_d}|^2$).

It is now possible to write the eq. (3.10) as the sum of two terms, a coherent and an incoherent part:

$$\frac{1}{\hbar}\frac{d^2\sigma}{d\Omega d\varepsilon} = \underbrace{\frac{k_f}{k_i}\frac{N\sigma_{coh}}{4\pi}S_{coh}(\mathbf{Q},\omega)}_{coherent} + \underbrace{\frac{k_f}{k_i}\frac{N\sigma_{inc}}{4\pi}S_{inc}(\mathbf{Q},\omega)}_{incoherent} , \tag{3.11}$$

where $S_{coh}(\mathbf{Q},\omega)$ and $S_{inc}(\mathbf{Q},\omega)$ are respectively the *dynamic structure factor* and the *incoherent dynamic structure factor* and N the number of scattering centers.

The two functions can be expressed, respectively, as:

$$\begin{aligned} S_{coh}(\mathbf{Q},\omega) &= \frac{1}{2\pi\hbar N}\sum_{j,k}\int_{-\infty}^{+\infty}\left\langle e^{-i\mathbf{Q}\cdot\mathbf{R}_j(0)}e^{i\mathbf{Q}\cdot\mathbf{R}_k(t)}\right\rangle e^{-i\omega t}dt , \\ S_{inc}(\mathbf{Q},\omega) &= \frac{1}{2\pi\hbar N}\sum_{j}\int_{-\infty}^{+\infty}\left\langle e^{-i\mathbf{Q}\cdot\mathbf{R}_j(0)}e^{i\mathbf{Q}\cdot\mathbf{R}_j(t)}\right\rangle e^{-i\omega t}dt . \end{aligned} \tag{3.12}$$

The time Fourier transforms of eqs. (3.12) give a time-dependent functions known as *intermediate scattering function* and *self-intermediate scattering function*:

$$I_{coh}(\mathbf{Q},t) = \frac{1}{2\pi\hbar N}\sum_{j,k}\left\langle e^{-i\mathbf{Q}\cdot\mathbf{R}_j(0)}e^{i\mathbf{Q}\cdot\mathbf{R}_k(t)}\right\rangle , \tag{3.13}$$

$$I_{inc}(\mathbf{Q},t) = \frac{1}{2\pi\hbar N}\sum_{j}\left\langle e^{-i\mathbf{Q}\cdot\mathbf{R}_j(0)}e^{i\mathbf{Q}\cdot\mathbf{R}_j(t)}\right\rangle . \tag{3.14}$$

The intermediate scattering functions are dimensionless, while the scattering functions themselves are of dimension ω^{-1}, as defined via eq. (3.8). As shown explicitly by eq. (3.11), scattering functions are obtained via the measurement of double differential cross sections. Intermediate scattering functions are, instead, directly accessible with neutron-spin-echo techniques [36].

Quasielastic neutron scattering

Let us analyze the case of a liquid system. The simplest approach to describe these systems is given by the classical approximation, *i.e.*, considering a monoatomic liquid, consisting of N particles of mass M which follow the Boltzmann statistics. This approximation, for most of the systems analyzed, it is widely accepted, since interatomic distances are large compared to the wavelengths normally used.

Since a fluid is an isotropic system, in these expressions is considered only the module of the wavevector Q.

We can show that the response function is the Fourier transform of the *relaxation function* $I(Q,t)$, namely:

$$S(Q,\omega) = \frac{1}{2\pi}\int e^{-i\omega t} I(Q,t)dt \ . \tag{3.15}$$

In the case of classical fluids we can write for the relaxation function:

$$I(Q,t) = \frac{1}{N}\langle \rho_Q \rho_Q^* \rangle \ , \tag{3.16}$$

that is true for the coherent part, while the single particle contribution is:

$$I_s(Q,t) = \langle e^{i\mathbf{Q}\cdot(\mathbf{R}(t)-\mathbf{R})} \rangle \ . \tag{3.17}$$

It should be noted that equation (3.15), with relations (3.16) and (3.17) is attributable to the result obtained (see section 3.2.1):

$$S(\mathbf{Q},\omega) = \frac{1}{2\pi\hbar N}\int_{-\infty}^{\infty} e^{-i\omega t} \sum_{jj'} \langle e^{-i\mathbf{Q}\cdot\mathbf{R}_j} e^{i\mathbf{Q}\cdot\mathbf{R}_{j'}} \rangle dt \ .$$

In the classical fluids theory we do not have a single expression for the response function that is valid for each value of Q and ω; rather are used different models, depending on the range of values of Q and ω we want to examine.

Is also useful to introduce the static structure factor. This is defined as the integral in ω of coherent part of the response function:

$$S(Q) = \int S(Q,\omega)d\omega = \frac{1}{N}\langle \rho_Q^2 \rangle \ . \tag{3.18}$$

From the definition (3.18) and from the definition of density operator $\hat{\rho}(\mathbf{r},t) = \sum_j \delta[\mathbf{r} - \hat{\mathbf{R}}_j(t)]$, it is clear that the static structure factor depends on the correlations between different atoms at the same instant, is therefore a measure of the instantaneous arrangement of the diffusion centers of the system. For example, in a perfect crystal, we

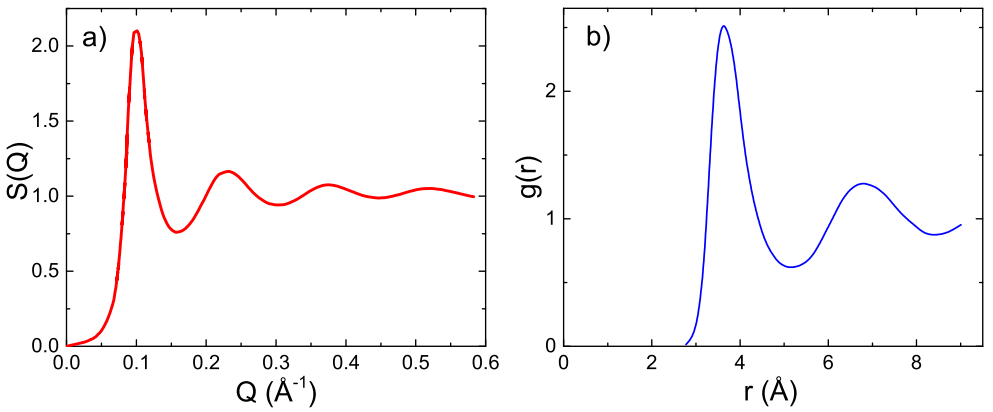

Figure 3.3: (a) Example of static structure factor for a liquid. (b) Pair distribution function.

have a set of delta functions of Dirac corresponding to the positions of the atoms in the Q-space, while for systems with no long range order $S(Q)$ has a trend similar to that shown in Figure 3.3a.

To understand the analytic form of (3.16) and (3.17) we distinguish two regions: one at high Q values and one at low Q values. At intermediate Q values an univocal formulation does not exist, but only approximations that tend, in the respective limits, to the situations that will be described later (see Figure 3.4).

By coherent scattering we have information about the positions and relative movements of different particles in the liquid. As shown above, the intermediate scattering function $I(\mathbf{Q},t)$ is:

$$I(\mathbf{Q},t) = \frac{1}{N}\sum_{jj'}\langle e^{-i\mathbf{Q}\cdot\mathbf{R}_j(0)} e^{-i\mathbf{Q}\cdot\mathbf{R}_{j'}(t)}\rangle \ ,$$

and it is the correlation function associated with this type of diffusion.

At $t = 0$, $I(\mathbf{Q},t)$ is the static structure factor of the system $S(Q)$, whose typical trend is shown in Figure 3.3a. The main peak is followed by rapid oscillations that tend to the asymptotic value $S(\infty) = 1$.

The function $S(Q)$ is related to the pair correlation function $g(r)$ through the relation:

$$S(\mathbf{Q}) = 1 + \rho_0 \int e^{i\mathbf{Q}\cdot\mathbf{r}} g(r) d\mathbf{r} \ , \tag{3.19}$$

where $\rho_0 = N/V$ is the particle density of the liquid. The static pair distribution function $g(r)$ is a measure of the probability of finding an atom at a distance r from

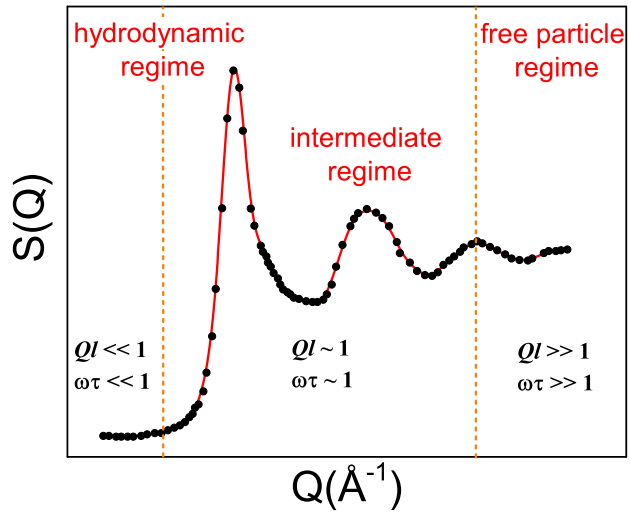

Figure 3.4: Scheme of a static structure factor $S(Q)$. It is possible to distinguish three regions: the hydrodynamic limit, an intermediate regime and the limit of free particle.

one placed in the origin (Figure 3.3b). In the inner region of the atom this probability is practically zero, then rises rapidly up to a first peak, thus determining the oscillations in the static structure factor at large Qs.

The single particle motion can be studied starting from the self intermediate scattering function, associated with the particles density:

$$I_{inc}(Q,t) = \frac{1}{N}\sum_j \langle e^{-i\mathbf{Q}\cdot\mathbf{R}_j(0)} e^{i\mathbf{Q}\cdot\mathbf{R}_j(t)} \rangle \ .$$

Given the isotropy of a fluid, such a function, as well as $S(Q,\omega)$, will depend exclusively by the module of Q. The frequency spectrum of the function $I_{inc}(Q,t)$ is the incoherent dynamic structure factor $S_{inc}(Q,\omega)$, tied to the incoherent diffused experimental intensity:

$$S_{inc}(Q,\omega) = \frac{1}{2\pi}\int e^{-i\omega t} I_{inc}(Q,t)dt \ .$$

Even in the case of incoherent scattering, the two functions $S_{inc}(Q,\omega)$ and $I_{inc}(Q,t)$ provide information in a spatial range of the order of $2\pi/Q$, but for what which concerns the single particle motion.

Considering the relation between the wavevector Q and the average distance l between the particles and between the frequency ω and the mean time between collisions τ, is possible to distinguish three extreme situations (Figure 3.4):

- $Ql \ll 1$ and $\omega t \ll 1$. It is a situation almost macroscopic, the system can be described as a continuous fluid and the dynamics of its particles is essentially diffusive. In this case the classical theory provides for $S_s(Q,\omega)$ a Lorentzian spectrum centered in $\omega = 0$, with a full width at half maximum (FWHM) equal to $2DQ^2$ where D is the diffusion coefficient of the system.

- $Ql \approx 1$ and $\omega t \approx 1$. In this intermediate region are not possible immediate simplifications, but the attempt is to introduce approximate models that tends to explain the behavior of the diffusing particle. One of these models is that of cage diffusion, which provides that the particle which diffuses remains trapped in a cage constituted by the first neighbors for a finite time.

- $Ql \gg 1$ and $\omega t \gg 1$. In this regime, the wavelength is much smaller than the average distance l between the particles and the characteristic time is very lower than the average collision time τ. So, every single particle does not perceive the presence of the other and can be regarded as non-interacting. In this limit, the classic spectrum for $S_s(Q,\omega)$ is determined by a statistical distribution of velocities and its form, in general, may be approximated by a Gaussian centered at $\omega = 0$ with an half width at half maximum (HWHM) equal to $[2\ln^2(\frac{k_BT}{m})]^{1/2}Q$, tied to the mean square velocity of a particle $\langle \mathbf{v}_j^2 \rangle = 3(k_BT/m)$.

Part of the present work is dedicated to the study of quasi-elastic scattering (QENS) [35,46], which provides information on the dynamics of the random motions within the sample. QENS concerns to those inelastic events in neutron scattering that are almost elastic (Figure 3.5). Such term is usually used to describe a widening of the elastic line in the energy spectrum rather than the discrete peaks representing inelastic processes. As mentioned, neutron scattering - and thus also QENS - contains coherent and incoherent components. The coherent component gives information about interference between atoms or molecules. Incoherent scattering describes the scattering by single atoms: if the atoms or molecules experience random motions during the scattering, a transfer of energy to or from the neutrons is related to this single-particle scattering. This gives a broadening of the line arising from elastically scattered neutrons, the width of which is evidently connected to coefficient that controls the diffusion. Thus QENS can be used to study diffusion, where an individual particle performs a random walk over the sample [47,48].

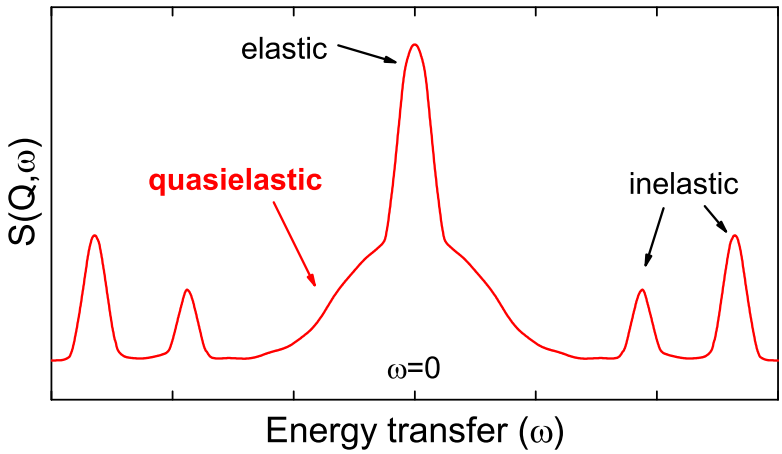

Figure 3.5: Diagram of an $S(Q,\omega)$. In *elastic scattering* there is no energy exchange ($\hbar\omega = 0$) and ideally it should be represented by a delta function. *Inelastic scattering* presents an energy exchange $\hbar\omega \neq 0$ due to processes that occur at discrete energy step such as stretching modes, vibrational modes, etc. In *quasielastic scattering* the energy exchange is different from zero but of the order of μeV. This is due to events occurring with an energy distribution such as translations, rotations, etc [46].

In general, for a diffusing atom within a fixed volume, the incoherent scattering function $S_{inc}(Q,\omega)$ in the elastic region is separable into a purely elastic component, $A_0(Q)\delta(\omega)$, and a quasi-elastic component centered on $\omega = 0$, $A_1(Q)L(\omega)$, where $\delta(\omega)$ is the delta function and $L(\omega)$ is a Lorentzian function.

$$S(Q,\omega) = A_0(Q)\delta(\omega) + A_1(Q)L(\omega)\ . \tag{3.20}$$

The elastic component is used to characterize the geometry of the underlying motion and the Lorentzian term gives information on the time scale of the diffusion. The elastic intensity as a function of Q can be represented by a structure factor called the elastic incoherent structure factor (EISF), which can be written:

$$EISF = \frac{A_0(Q)}{A_0(Q) + A_1(Q)} = \frac{\text{elastic intensity}}{\text{total intensity}}\ . \tag{3.21}$$

For purely translational diffusion, the EISF is zero except at $Q = 0$. For the rotational diffusion of a particle, the EISF is unity at $Q = 0$ and falls to a minimum at a Q value which is inversely proportional to the radius of gyration of the rotating molecule. The shape of EISF represents the geometry of the diffusional process.

Another characteristic of the incoherent scattering function, the Q-dependence of the quasielastic line width $\Gamma(Q)$ of the central component, which is due to translational long-range diffusion.

In a liquid the quasielastic contribution is almost always observed, even if generally it is superposed on the inelastic processes. In the condition of small Q exchanged is however possible separate this contribution from other processes [36].

Also in some crystals that display orientational disorder (called "plastic crystals") is possible to see the quasielastic contribution, in fact, molecules are subjected to reorientations between a finite number of quasi-equilibrium configurations. This phenomenon corresponds to the transport of individual atoms between quasi-equilibrium sites and, thus, also gives rise to quasielastic features in the neutron-scattering response.

3.3 Time-of-Flight inelastic neutron scattering

The Time-of-flight (TOF) technique is a method for determining the kinetic energy of a neutron, by the measure of the time it takes to cover a known distance between two fixed points, since its velocity, after the moderation, is of the order of kms^{-1}. Energy ($\hbar\omega$) and momentum (Q) transfer are the quantities measured in inelastic experiments. Spectrometers suitable for such measures can be divided into two categories:

- **Direct geometry spectrometers**: in which the incident energy, E_i (crystal or chopper) is selected, and the final energy, E_f, is determined by time-of-flight.
- **Indirect (inverted) geometry spectrometers**: in which the sample is illuminated by a white incident beam, whose energy is determined at the sample position by the measurement of the time-of-flight and the final energy is measured by a crystal.

At a pulsed source all spectrometers use the time-of-flight techniques, while on continuous sources choppers are needed to provide a pulsed beam.

For direct geometry spectrometers k_i is fixed and k_f varies as a function of time whereas the opposite is true for indirect geometry instruments. As seen in Section 3.1, the conservation laws give:

$$\mathbf{Q}^2 = \mathbf{k}_f^2 + \mathbf{k}_i^2 - 2\mathbf{k}_f\mathbf{k}_i\cos(\phi)\ , \qquad \frac{\hbar^2 Q^2}{2m} = E_i + E_f - 2\left(E_i E_f\right)^{1/2}\cos(\phi)\ . \quad (3.22)$$

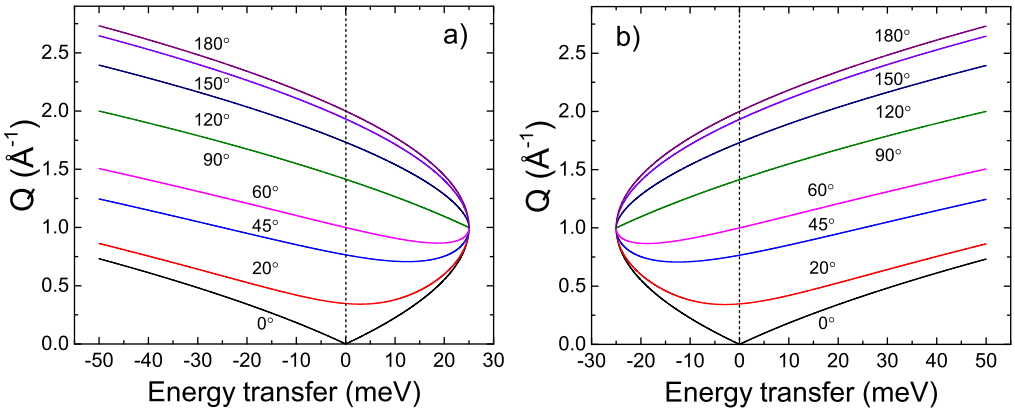

Figure 3.6: Cinematic ranges through (Q, ω) space. In (a) a direct geometry spectrometer and in (b) an indirect geometry spectrometer for detector at the given scattering angles (respectively $0, 20, 45, 60, 90, 120, 150$ and $180°$). The graphs have been done using an energy transfer for both processes of 25 m eV.

For direct geometry E_f can be eliminated leaving

$$\frac{\hbar^2 Q^2}{2m} = 2E_i - \hbar\omega - 2\cos(\phi)\left[E_i\left(E_i - \hbar\omega\right)\right]^{1/2} \tag{3.23}$$

These are parabolas in (Q, ω) space. To make optimum use of direct geometry spectrometers, they are equipped with large detector arrays, giving simultaneous access to a large area of (Q, ω) space.

Similarly for indirect geometry, E_i can be eliminated giving

$$\frac{\hbar^2 Q^2}{2m} = 2E_f - \hbar\omega - 2\cos(\phi)\left[E_f\left(E_f - \hbar\omega\right)\right]^{1/2} \tag{3.24}$$

The parabola are inverted. An important feature of the indirect geometry instrument is the access to a wide range of energy transfers for energy loss (Figure 3.6).

3.3.1 The high resolution spectrometer *IRIS*

IRIS is a high-resolution quasi/in-elastic neutron scattering spectrometer (Figure 3.7). It is an indirect geometry spectrometer, that means that neutrons scattered by the sample are analyzed in energy by means of Bragg scattering from a crystal-analyzer array. As in other instruments at a pulsed neutron source, the time-of-flight technique

is used for data analysis. The instrument uses neutrons coming from a liquid hydrogen moderator at 25 K and consequently it has access to a large flux of cold neutrons [49,50].

The primary spectrometer. The transport of the neutrons, from the moderator to the sample position, is achieved using a neutron guide. At IRIS the guide is terminated by a 2.5 m long converging $Ni - Ti$ supermirror. The supermirror helps to focus the beam at the sample position but also it is useful to increase incident flux (a factor of ≈ 3 at 5 Å). At the sample position the neutron flux is roughly $5.0 \cdot 10^7$ n cm^{-2}s^{-1} (white beam at full ISIS intensity). After the moderation neutrons wavelength range is defined by two disc choppers. These are rotating discs (operating at 50, 25, 16.6 or 10 Hz) that permit the passage of neutrons in the selected wavelength range. The choppers are constructed with and absorbing material and each one presents small adjustable apertures to let the neutrons pass. The upper and lower limits of the incident wavelength range are defined by adjusting the chopper phases. Wavelength range defines the energy resolution and energy-transfer range (inelastic) or d-spacing range (elastic) covered during an experiment. Both choppers are synchronized to avoid problematic frame overlap.

The secondary spectrometer. It is composed of the sample chamber and a part consisting of a vacuum vessel containing two crystal analyzer arrays (Pyrolytic Graphite and Mica), two detector banks composed of 51 ZnS scintillator element and a diffraction detector bank at $2\theta = 170°$ containing ten ^3He gas tubes. Incident and transmitted beam monitors are positioned before and after the sample position. To reduce the background contributions the pyrolytic graphite analyzer is mantained at 10 K.

Operational mode and resolution. During a quasielastic neutron scattering experiments, the scattered neutrons are energy-analyzed by means of Bragg scattering from a large array of single crystals (Pyrolytic Graphite in our case). Only those neutrons with the appropriate energy to satisfy the Bragg condition are directed towards the detector bank. By recording the time of flight, energy gain and energy loss processes may be investigated [49,50]. The scattering process is shown schematically in Figure 3.8.

The two disc choppers define the energy range of incident neutron. Consequently, the time-of-flight, t_1 , of each neutron along the primary flight path, L_1 , is variable.

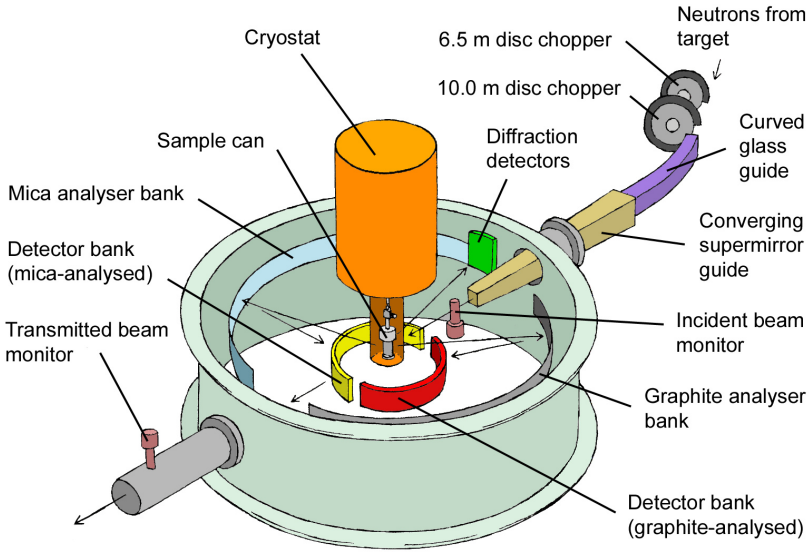

Figure 3.7: IRIS Spectrometer [50]. Choppers select the desired neutron wavelength whereas the supermirror focuses neutrons at the sample position.

However, since only those neutrons with a final energy, E_2 , that satisfies the Bragg condition, $\lambda = 2d\sin\theta$, are scattered toward the detectors. Thus:

$$E_2 = \frac{1}{2}m_n\left(\frac{L_2}{t_2}\right)^2 = \frac{p^2}{2m_n} = \frac{1}{2m_n}\left(\frac{h}{2d\sin\theta}\right)^2 , \tag{3.25}$$

where d is the d-spacing of the analyzing crystal. The distance from the sample position to the detector bank (L_2) is well known, hence the time, t_2, can be calculated using,

$$t_2 = \frac{2m_n L_2 d\sin\theta}{h} \tag{3.26}$$

Finally measuring the total time-of-flight, $t = t_1 + t_2$, and having accurate knowledge of t_2, L_1 and L_2, can be determined the energy resolution:

$$\Delta E = E_1 - E_2 = \frac{1}{2}m_n\left[\left(\frac{L_1}{t_1}\right)^2 - \left(\frac{L_2}{t_2}\right)^2\right] . \tag{3.27}$$

In our experiment we used an incident wavelength of 2.52 Å that provide an energy resolution (FWHM) of 17.5 µeV. The energy range scanned has been from -0.5 and 0.5 m eV and the [002] reflection of the pyrolitic graphite analyzer permitted us to explore the Q-range between 0.44 and 1.8 Å^{-1}.

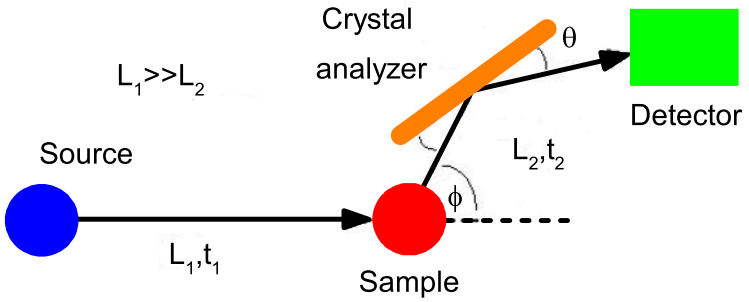

Figure 3.8: An indirect-geometry inelastic neutron scattering spectrometer layout.

3.3.2 The time-of-flight Spectrometer *TOFTOF*

TOFTOF is a direct geometry multi-chopper time-of-flight spectrometer, located at the research neutron source Heinz Maier-Leibnitz (FRM II) (Figure 3.9). It is suitable for both inelastic and quasi-elastic neutron scattering and is ideal for material science investigations since it offers an excellent signal-to-background ratio, high energy resolution and high neutron flux..

The instrument owes its name (TOFTOF) to the fact that it selects the incident beam energy by a time-of-flight monochromatization (TOF-) in the primary spectrometer, and after the collisions with sample the energy transfer is measured via tof technique (-TOF).

The primary spectrometer. The s-shaped curved guide that transports neutrons to the instrument, behaves as a filter for the neutrons with a cutting edge of 1.38 Å. The chopper system consists of seven independent fast rotating disc choppers (up to 22 000 rpm) positioned in four separated housings. The chopper discs are made of carbon-fiber-reinforced plastic and coated with ^{10}B for neutron absorption. The first chopper pair (numbers 1 and 2) is used as a rotating pulsing chopper producing short polychromatic neutron bunches from the continuous neutron beam.

Each bunch broadens after a certain path, since each one is composed of neutrons with different energies and, therefore, velocities. Thus, a further pair of chopper (6 and 7) is placed at the end of the primary spectrometer and used as monochromator. These choppers cut a small wavelength range out of each pulse. Hence neutrons that are too

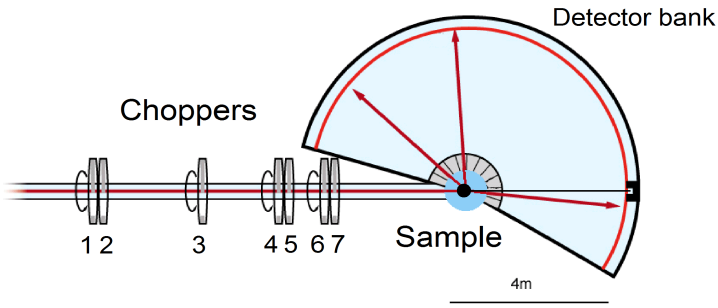

Figure 3.9: TOFTOF layout [51]. First pair of choppers (1 and 2) are coupled with the last one (6 and 7) and operate as a velocity selector. Choppers 4 and 5 suppress the transmission of higher order wavelengths, and 3 is the frame overlap chopper. The energy of scattered neutron is measured by the time of flight from the sample to the detectors bank. The angular range covered by detectors is $-15\ ^\circ$ to $-7\ ^\circ$ and $7\ ^\circ$ to $140\ ^\circ$. Each single detector covers an angular range of about $0.5\ ^\circ$.

fast or too slow are absorbed by the boron coating. To suppress the transmission of neutrons with higher order wavelengths, two more choppers (4 and 5) are used. In such way the passing of neutrons with velocities different from the one selected is avoided. The remaining single chopper can be used to reduce the neutron pulse frequency at the sample to decrease the overlap of successive pulses due to energy gain and energy loss of the neutrons by the interaction with the sample (so-called "frame overlap") [52].
Each chopper presents two pair of slits, a wide and a narrow one, positioned oppositely each other (Figure 3.10a). Since the wide slits are adapted to the width of the neutron beam they represent a good choice with respect intensity and resolution of the primary spectrometer. The narrow slits, instead, give the possibility to increase the resolution, even if this is accompanied by an intensity decrease. The switch from one to another slit is achieved by tuning the rotational frequency of the frame overlap chopper with respect the one of the pulsing and monochromating choppers.
Furthermore, to avoid an overlap of slow scattered neutrons with the the following neutron pulse one can acts on the chopper frequency. A good compromise is given by

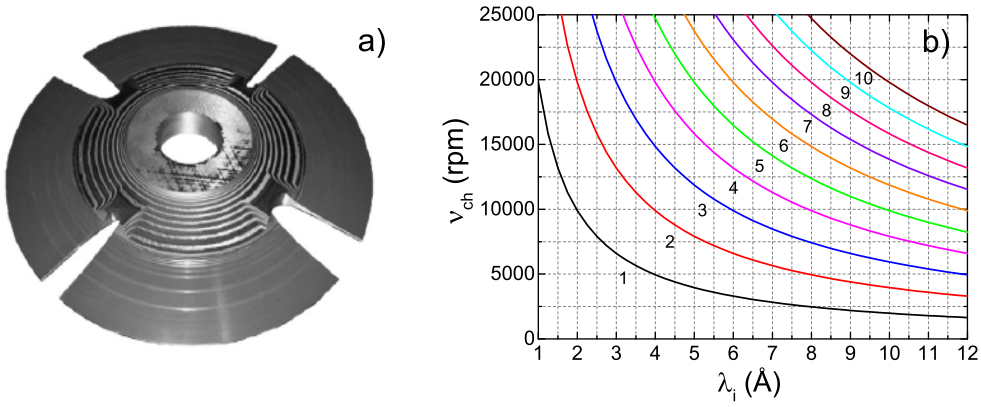

Figure 3.10: (a) Photo of a TOFTOF chopper disc. It is shown the narrow and a wide slit pair. (b) Frame overlap ratios n for the TOFTOF spectrometer.

the equation:

$$\nu_{ch} = 1.978 \times 10^4 \frac{n}{\lambda_i(\text{Å})}, \tag{3.28}$$

where ν_{ch} is chopper rotation frequency of all choppers except the frame overlap chopper and λ_i is the mean wavelength of incident neutrons. Relation (3.28) is illustrated in Figure 3.10b for all the frame overlap ratios available at TOFTOF [52]. It can be used to determine the frame overlap ratio for any instrument configuration. It is important to note that the frame overlap ratio increases with increasing chopper speed for a constant wavelength and this is accompanied by a decrease in the beam intensity that reaches the sample.

The secondary spectrometer. It is composed by the sample chamber and the flight chamber that contains the detectors bank. The sample chamber and the flight chamber are filled with Ar and they separated by an Al foil. The detectors (Figure 3.9) are mounted on eight racks, which are positioned around the flight chamber. The available space allows the placement of 1006 detectors. The shielding of the racks is made by a Cd coverage, which prevents rescattering of the neutrons not captured by detectors. The detection at TOFTOF is made through the reaction of neutrons with ^3He nuclei. The neutrons captured by detectors cause a decay that produce a detectable current pulse.

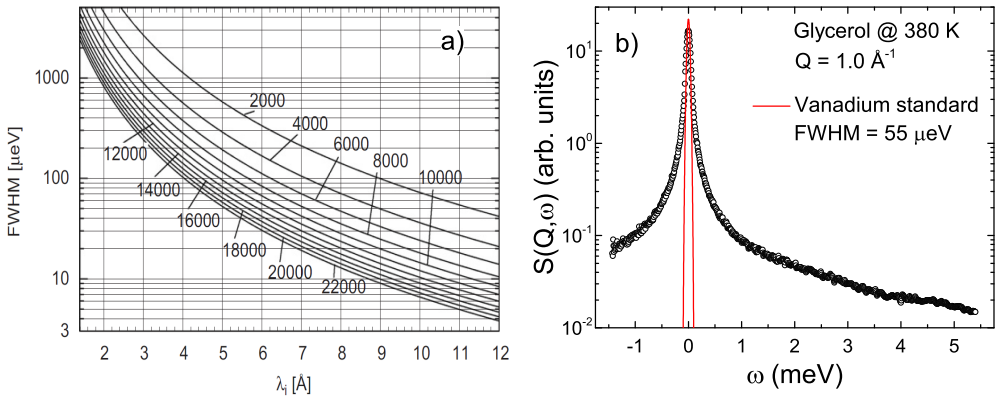

Figure 3.11: (a) Calculated resolution curves of the TOFTOF spectrometer for different chopper frequencies (wide slits). The curves are labeled with the values of the chopper frequencies in rpm [52]. (b) Glycerol spectrum at $T = 380$ K and $Q = 1.0$ Å^{-1}. Red line shows the resolution peak with a FWHM of 55 μeV measured with vanadium rod.

Resolution. In a chopper time-of-flight instrument there is the possibility to regulate the resolution according to the needs of the experiment. The precision with which the transmitted neutron energies are determined gives the energy resolution. It can be improved choosing neutrons with lower incident velocities or increasing the chopper rotational speed. The energy resolution diminishes by increasing the energy transferred and it can be calculated in the form of the instrumental line width ΔE (FWHM). The formula is not included in this work, but it contains all the geometrical and functional information about the spectrometer and it is given in [52, 53].

Also the divergence of the incident beam influences the resolution. Neutrons are reflected by the guide with an incident angle (degrees) of up to $m \cdot \lambda$, where λ is the neutron wavelength (in nanometres) and m is defined as the ratio between the angle of total reflection of the neutron guide compared to the angle of total reflection of an hypothetical neutron guide coated with nickel. This part of the resolution is only slightly influenced by the wavelength of the neutrons.

To probe the dynamics for liquid glycerol in the nanoseconds time-scale has been used a wavelength of 6.0 Å, that coupled to a choppers rotational frequency of 12000 *rpm* has provided an energy resolution of 55 μeV (see Figure 3.11a). In our experiment, the resolution in Q is not taken into account, this is because the energy-dependence of the

incoherent scattering is evaluated and not the Q-dependence of the coherent process. Thus the energy resolution has to be considered, and for this end, the resolution is measured using a sample that does not show any quasielastic broadening. In our case was used a vanadium sample for the determination of the resolution (see Figure 3.11b).

3.4 QENS data reduction

An ideal experiment is based on three fundamental conditions [54]: a perfect instrument, an ideal sample and a direct correlation between the intensity $I(\theta, \omega)$ and $S(Q, \omega)$. Before proceeding with the proper analysis it is necessary to perform appropriate modifications to the measured data.

The measure consists in the sum of various contributions. Of such contributions, only the signal coming from the sample is of interest in the subsequent analysis. Thus, all the contributions not belonging to the scattering signal have to be subtracted.

There are different programs which are capable of reducing the time-of-flight data. In this thesis the standard data reduction and evaluation tool used in TOFTOF has been Frida [55], while the one used in IRIS has been Mantid [56]. Although the programs are different the data reduction procedure is similar, therefore, a general and common description of data evaluation process will be given.

It is possible to calculate the scattering functions from the measured data in several steps. However it is important to note that, depending on the need of the data treatment and the characteristics of the sample, not all of these steps have been done in the presented studies.

3.4.1 General data reduction procedure

Instrumental effects. Normally, the data have to be converted to be a function of neutron energy transfer, the energy-dependent detector efficiency is corrected, and the detector sensitivity is normalized using measurements performed on a vanadium sample.

An ideal detector measures all the neutrons that hit it as a function of the incident neutron energy, E_f. In contrast, in a real detector, part of these neutrons are not revealed for intrinsic reasons due to the detector operation principles. It is possible to define the efficiency, $\eta(E_f)$, as the measure of the deviation from the ideal case. It is the ratio between the detected neutrons and all the neutrons incident on the detector

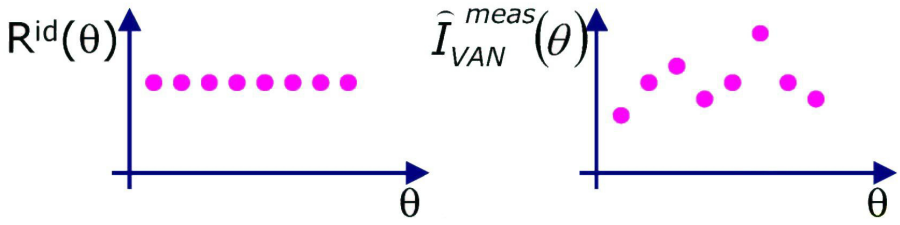

Figure 3.12: Intensity I_{Van}^{meas} in the ideal case and in the real case [54].

as a function of the energy E_f. This quantity is dimensionless and its value is between 0 and 1. The detection process corresponds to the absorption, by the detector, of the neutron. The efficiency also depends on the scattering angle 2θ; generally one proceeds via normalization with the vanadium rod. This element diffuses the neutrons isotropically, since it has a completely incoherent cross section, so that its energy integrated spectrum is, ideally, a constant value as a function of the scattering angle, while as a function of energy it turns out to be an elastic diffuser. Eventual fluctuations of the experimental spectrum highlight efficiency differences between the angles, and then between the detectors (Figure 3.12). Dividing the spectra for the normalized intensity $I_{Van}^{meas}(\theta)$ is possible to correct such difference and also, in part, the effects due to the angular resolution, since not all the angles have the same probability to be attained by the diffused beam, because of the geometry of the experiment, the divergence of the incident beam and of the finite dimensions of the detectors and the sample.

Experimentally we must also consider the energy resolution, in fact, both the incident and diffused energy are affected by uncertainties due, in the case of a time of flight spectrometer, to the spatial path or to the pulse duration. For these experiments, *i.e.* for a time-of-flight spectrometers, the uncertainties on the flight time and on the path of neutrons produce an energetic uncertainty which is function of them:

$$\Delta E = \frac{h^3}{m^2 L \lambda^3}\Delta t + \frac{h^2}{mL\lambda^2}\Delta L \quad \Rightarrow \quad \frac{\Delta E}{E} = \frac{2h}{mL\lambda} + 2\frac{\Delta L}{L} \ . \tag{3.29}$$

If the energy resolution of the instrument was perfect, the response function should be like $R(\omega, \omega_f) = \delta(\omega - \omega_f)$, whereby:

$$I^{meas}(\omega) = \int R(\omega_f, \omega) I^{true}(\omega_f) d\omega_f = I^{true}(\omega) \ . \tag{3.30}$$

Actually, the response $R(\omega, \omega_f) \neq \delta(\omega - \omega_f)$ and it is therefore necessary to be able to calculate or measure it. To do this we need a sample such that $I^{true}(\omega) \approx \delta(\omega)$ and whose intensity does not vary excessively with Q, an element that diffuses incoherently. An element that falls within that category is precisely the vanadium. Its spectrum is a measure of enlargement related to the energy resolution, and then, to the energetic response function of the spectrometer. A further correction of the data is then given by the convolution:

$$I^{meas}(\omega) \approx \int I^{meas}_{Van}(\omega - \omega_f) I^{true}(\omega_f) d\omega_f \ . \tag{3.31}$$

Imperfections of the sample. One must consider that passing through the sample, the incident neutron beam undergoes an attenuation due to two possible processes: *absorption* and *scattering*. Therefore, the obtained scattering function $S(2\theta, \omega)$ has to be corrected for these effects. These phenomena are usually corrected with the Paalman and Pings algorithm [57]. The algorithm to correct the absorption of neutrons requires the scattering and absorption cross sections of the sample and of the container and returns the correction factors, that are dependent on the scattering angle and the energy transfer dependent, that are used to scale the measurements. The scattering and absorption cross section have been calculated using the "Neutron cross section calculation" tool implemented in DAVE software [58].

Another contribution to consider is that due to the *multiple scattering*, *i.e.* the contribution due to those neutrons that reach the detector after being scattered more than once from the sample, from the cell or by both. In general, one can express the measured intensity as

$$I^{meas} = I^{meas}_1 + I^{meas}_m \ , \tag{3.32}$$

where I^{meas}_1 is the intensity of single scattering and I^{meas}_m is the sum of all the orders of multiple scattering. The effects of subsequent diffusions can be of two types (Figure 3.13a):

- attenuation, namely the removal from the original direction of an individually diffused neutron;
- intensification of the single signal for an angle that differs from the original.

In the multiple scattering expression (eq. 3.32) the dominant term is the first, the double scattering, while increasing the order of diffusion, multiple scattering becomes less probable and less intense. In Figure 3.13b are displayed various examples of multiple

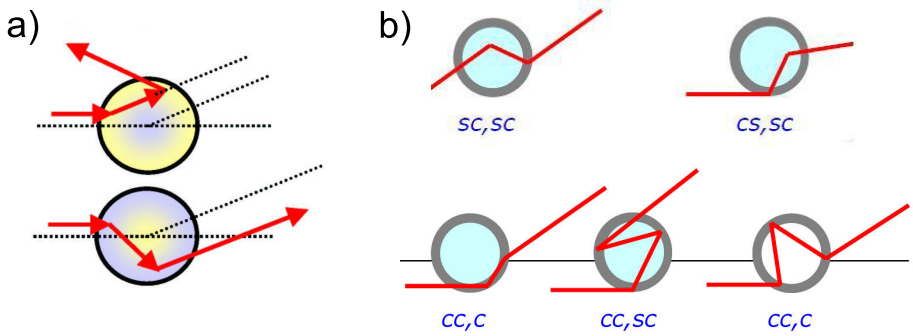

Figure 3.13: (a) Double diffusion cases. In the figure above the doubly diffused neutron is removed from the original direction, causing an attenuation of the signal, while in the lower figure, neutron goes to intensify the original signal. (b) Multiple scattering. In the figure S indicates the sample and the C the cell.

scattering. An important aspect of multiple scattering is that there are different contributions to it, depending on whether the beam interacts with the sample first and then with the cell or viceversa, but also that interacts twice with the sample or twice with the cell. Of course it is fundamental the type of material that the beam passes through before and after the diffusion (Figure 3.13b). In order to minimize the effect of multiple scattering, usually the cell thickness is selected in such a way that the relation between the incident and the scattering intensities, $I_{scat} = 0.1 I_{inc}$ is satisfied. Since the multiple scattering can not be measured, it must be calculated numerically, or simulated. The second procedure provides a satisfactory result without imposing restrictive requirements to the cell size or to the sample diffusive power with respect to the cell itself.

Finally, the data were grouped into spectra at constant Q, resulting in the scattering functions $S(Q,\omega)$ of the whole system in the beam.

The obtained $S_{meas}(Q,\omega)$ is not equal to the $S(Q,\omega)$. This is caused by the principle of detailed balance. In real systems the occupation of excited states is not symmetrical but it is driven by the Boltzmann-factor. Hence an energy transfer from the sample to the neutron is less probable than the opposite process. This can be seen, writing:

$$S_{meas}(Q,-\omega) = \exp\left(\frac{\hbar\omega}{k_B T}\right) S_{meas}(Q,-\omega) \tag{3.33}$$

where $\omega > 0$ denotes a neutron energy gain scattering process. At the high temperatures and the low energy transfer the detailed balance factor can be considered constant, thus such a correction has not been taken into account.

Background subtraction. From $S_{meas}(Q, \omega)$, the contribution of the samples has to be extracted by subtracting the background contributions. This contribution is due to the neutrons still present in the environment and the scattering of such neutrons with other materials that are on the beam. It should be moreover considered the cell that contains the sample. All these elements are in turn scattering centers and produce an additional signal which reaches the detectors. This scattering effect, mainly elastic, produces a background present in the flight channels.

To subtract such contribution is necessary to make two measurements: one of the empty instrument and the other with an absorbent material (typically cadmium) inside the cell. In this way one can determine the additional diffusion generated before and after the scattering process with the sample. One defines with X_S the intensity due to the measure *sample+cell*, with X_E the one due to the measure of *empty cell* and with X_A the contribution due to the measure *absorber+cell*. Then indicating with T the transmission coefficient of the sample, with S the contribution to the intensity of the sample, with C and A the terms of the empty cell and the absorber, respectively, we can write:

$$\begin{cases} X_S = A + S + T \cdot C \\ X_E = A + C \\ X_A = A \end{cases} \quad \Rightarrow \quad S = (X_S - X_A) - T \cdot (X_E - X_A) \ . \tag{3.34}$$

3.5 Model description

The main idea, used in the present work, to study the dynamics in glass forming systems is to separate the motions of a molecule in a translational part and a confined motion in which the molecule performs movements in finite volume.

The effect of the confinement in the liquid state, can be described as a transient trapping of molecules resulting by a decrease of temperature or by an increase of density. Microscopic density fluctuations in disordered fluids at high temperatures and low densities usually relax quickly on time scales of the order of few picoseconds. Then, by lowering the temperature or increasing the density in the liquid state, a rapid increase

in local order which surrounds the particle leads to a substantial increase of the structural relaxation times. A particle trapped in the confinement, in the liquid state, can only diffuse through the adjustment of a large number of molecules that surround it. Therefore there is a strong correlation between the motion of a single particle and the density fluctuations in the fluid.

In this Section some models for the description of such systems showing the thermal evolution of relaxation times will be presented.

Let us recall the relation:

$$\frac{d^2\sigma}{d\Omega d\omega} = N\frac{\sigma}{4\pi}\frac{k_f}{k_i}S(Q,\omega) \ , \tag{3.35}$$

where N is the number of molecules in the sample, k_i and k_f are respectively, the wave vector of the incident and scattered neutrons, and $S(Q,\omega)$ is the dynamic single-particle structure factor. Since N, σ, k_i and k_f are known quantities in a QENS experiment, $S(Q,\omega)$ can be directly derived from the double-differential cross section.

In the Van Hove theory of neutron scattering [34], $S(Q,\omega)$ is given in terms of the Fourier transform of the intermediate scattering function (ISF) of the atom, $I(Q,t)$, in accordance with the relationship:

$$S(Q,\omega) = \frac{1}{2\pi}\int I(Q,t)e^{i\omega t}dt \ . \tag{3.36}$$

It is possible to note that $I(Q,t)$ is the quantity of main interest related to the experiment.

3.5.1 The decoupling approximation

Considering the intermediate scattering function, eq. (3.14), we have to examine all the movements performed by molecule. Being extremely difficult, it is used the decoupling approximation that, generally accepted in QENS experiments, allows us to rewrite the intermediate scattering function as a product of the various contributions (Figure 3.14) [35, 59–61].

$$I(Q,t) = I_1(Q,t)\cdot I_2(Q,t)\cdot I_3(Q,t)\cdot \ldots \tag{3.37}$$

The condition for which such approximation is considered valid is given by the separation of time scales relative to the motions of the molecule. Simplifying and without losing the general validity, the analysis can be restricted to cases of identical molecules,

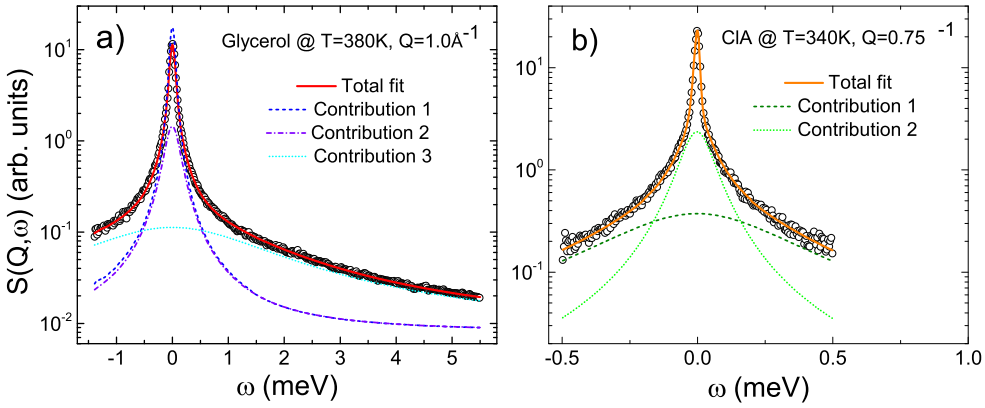

Figure 3.14: Dynamic structure factors are presented as a sum of different components. Each contribution corresponds to a distinct movement performed by the molecule. In (a) liquid glycerol at $T = 380$ K and $Q = 1.0$ Å^{-1} that presents three distinct movements, while in (b) plastic Cl-adamantane at $T = 340$ K and $Q = 0.75$ AA^{-1} shows two contributions to the total scattering function.

in which only one kind of atom (such as hydrogen) can be seen. Moreover, these atoms shall be regarded as dynamically equivalent. Therefore all the scattering laws are restricted to the case of a single scatterer [35].

Analyzing the position vector $\mathbf{R}(t)$ of any atom in the molecule it is possible to distinguish between intra- (translations and rotations) and inter-molecular (vibrations) motions. Let us assume that the dynamics of each movement can be written separately, obtaining:

$$\mathbf{R}(t) = \mathbf{r_{intra}}(t) + \mathbf{r_{inter}}(t) \ , \tag{3.38}$$

in which $\mathbf{r_{intra}}(t)$ describes the instantaneous position of the whole molecule, at time t, respect a coordinate system external from molecule, and $\mathbf{r_{inter}}(t)$ is the displacement from the equilibrium position caused by internal motions.

For example, dealing with liquid samples the position vector $\mathbf{r_{intra}}(\mathbf{t})$ can be divided in a translational $\mathbf{r_T}(t)$ component and a rotational $\mathbf{r_R}(t)$ one around its own center of mass. Then the dynamics of the hydrogen atoms can be thought as composed of three components: the translation of the center of mass, the rotation around the center of mass and the vibrational motion of the atom around its equilibrium position. The

intermediate scattering functions becomes:

$$I(Q,t) = I_T(Q,t) \cdot I_R(Q,t) \cdot I_V(Q,t) \ . \tag{3.39}$$

When a bulk sample is treated, the molecule can not assume all the positions in space and it is confined in a well-defined position. This lack of translational degree of freedom, leads us to consider three cases:

- In crystalline phases, each molecule has a precise equilibrium position and orientation, which are subjected to small amplitude oscillations due to thermal agitation.
- In the fully-disordered phases, a molecule can access to any position and orientation in space. Thus the treatment of the dynamics of these phases can be learned from the method originally developed for liquids.
- In cases of orientationally disordered phases, a convenient description of the molecular rotational motions is related on the existence of equilibrium positions for each molecule. Molecule fixed in its lattice position can rotate by instantaneous jumps [35].

Then for orientationally disordered phases:

$$I(Q,t) = I_R(Q,t) \cdot I_V(Q,t) \ . \tag{3.40}$$

The hypothesis of independence for different molecular movements gives us such formulation for ISF for a liquid sample (eq. 3.39) and for a bulk sample (eq. 3.40). Given eq. (3.36), it is possible to rewrite eqs. (3.39) and (3.40) in terms of the scattering functions:

$$S_{liquid}(Q,\omega) = S_T(Q,\omega) \otimes S_R(Q,\omega) \otimes S_V(Q,\omega) \tag{3.41}$$

$$S_{bulk}(Q,\omega) = S_R(Q,\omega) \otimes S_V(Q,\omega) \ , \tag{3.42}$$

where $\otimes$ denote the product of convolution. As stated in the Section 3.2.1, it is useful to remember that the functions $S(Q,\omega)$ have a Lorentzian shape. For what concerns the eq. (3.42) we must emphasize that, in this formulation, it has been completely neglected the contribution originating from lattice modes.

Furthermore, one should note that the vibrational contribution can be well approximated by a Debye-Waller factor, $\exp\left[-\frac{1}{3}\langle u^2\rangle Q^2\right]$, where $\langle u^2\rangle$ is the mean square vibrational amplitude of the hydrogen atom around its equilibrium position. Since in

the energy range investigated the vibrational factor is hidden by the quasi-elastic peak, then, the vibrational contribution has been neglected in the intermediate scattering function.

Decoupled contributions

After having established the validity of the decoupling approximation, functions that describe the translation and the confined motion will be discussed separately [62].

For the ***translational*** part we can write such function as a product of a short time dynamics and a decay at long times, because the time scales for the motion in the confinement and for the relaxation of the confinement itself are sharply separated. One can assume that the translational dynamics at small times of the trapped molecule can be treated as the motion of the center of mass in an isotropic harmonic potential, created by the mean field of the neighboring molecules.
On the other hand, the relaxation of the molecules forming the confinement at long times can be described with an exponential time decay. This relaxation model is characterized by the structural relaxation time τ_T, which is Q-dependent. Therefore, the translational ISF with the full time dependence can be written:

$$I_T(Q,t) = I_T^s(Q,t) \exp\left[-\frac{t}{\tau_T}\right] \approx \exp\left(-DQ^2 t\right) , \tag{3.43}$$

where D is *self-diffusion coefficient.*

Without placing restrictions on the type of motion, in general, for the **confined** part, in which the molecule can be considered immobile for infinite times, in a fixed volume, the intermediate scattering function can be written as the sum of a constant and an exponential decay:

$$I(Q,t) = const + e^x \qquad \overset{FT}{\Rightarrow} \qquad S(Q,\omega) = \delta(\omega) + L , \tag{3.44}$$

where $\delta(\omega)$ is a delta function and L is a Lorentzian function.

For sake of completeness an example of confined motion will be given. The case of molecular rotation around the center of mass will be treated. Considering a vector $\mathbf{b}(t)$ that originates in the center of mass, the rotational intermediate scattering function assumes the form:

$$I_R(Q,t) = \langle e^{-i\mathbf{Q}\cdot\mathbf{b}(t)} e^{-i\mathbf{Q}\cdot\mathbf{b}(0)} \rangle = j_0^2(Qb) + \sum_{l=1}^{\infty} (2l+1) j_l^2(Qb) C_l(t) , \tag{3.45}$$

in which $j_l(x)$ is the spherical Bessel function of the l-th order and $C_l(t)$ is the rotational correlation function of the order l. For a typical Q-range normally used in QENS experiments (in our cases $Q < 2.5$ Å) such expansion is very useful. The advantage is that the Q-dependence of the rotational ISF is exactly given and this calls for a model with smaller orders of the correlation functions that are Q-independent.
In a similar way of what done for translational dynamics, the rotational correlation function of the first order can be separated into motion at short times in the confinement, and a relaxation at long time. Then it is possible to write:

$$C_1(t) = C_1^s(t) \exp\left[-\frac{t}{\tau_R}\right], \tag{3.46}$$

where τ_R is the rotational relaxation time. At small times the orientation of the molecule is fixed by the presence of bonds with the first neighbors. Molecule performs harmonic oscillations around the direction of the bond, described by $C_1^s(t)$. At longer times, the bonds break and the confinement begins to relax, so that the molecules can reorient, losing memory of their initial orientation. Therefore, the rotational correlation function decays through the exponential relaxation.

3.5.2 Homogeneous vs Heterogeneous scenarios

In the study of liquid phase a model selection using an homogeneous (HG) and an heterogeneous (HT) scenario in describing the single particle dynamics has been performed.

Generally it is inclined to think of single-component liquid as affected by a homogeneous dynamic. This interpretation is valid, partly because many important properties can be derived from a modeling a liquid as a homogeneous continuum [63]. For example the diffusion, viscosity, ion mobility, and the rate of chemical reactions are all described on this basis. Beyond the contribution arising from the translational diffusion of the center of mass, a model has been built with two further relaxation processes that, homogeneously, affect all molecules. In such case the entire scattering function can be written:

$$\begin{aligned} S_{HG}(Q,\omega) = y_0 + \left[\delta(\omega) + \left(\frac{\Gamma_D}{\omega^2 + \Gamma_D^2}\right)\right] \otimes \left[a(Q)\delta(\omega) + (1 - a(Q))\left(\frac{\Gamma_a}{\omega^2 + \Gamma_a^2}\right)\right] \\ \otimes \left[b(Q)\delta(\omega) + (1 - b(Q))\left(\frac{\Gamma_b}{\omega^2 + \Gamma_b^2}\right)\right] \end{aligned}$$

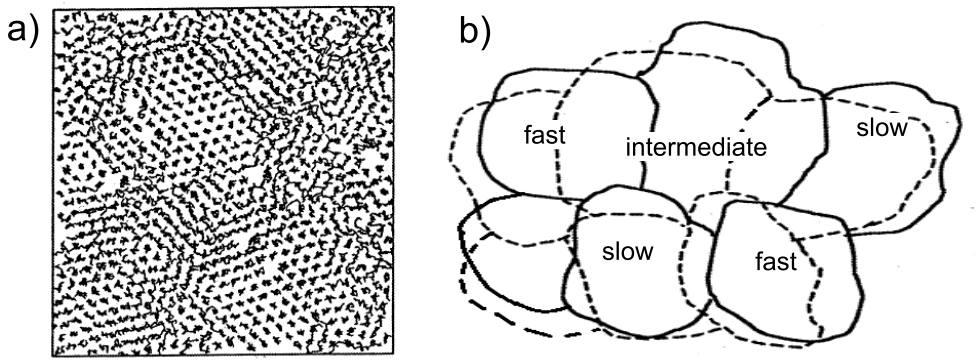

Figure 3.15: (a) Image of heterogeneous spatially dynamic. (b) Scheme of regions spatially heterogeneous dynamics near the glass transition. In these clusters molecules exhibit dynamics on different time scales. These regions are typically on the order of a few nanometers and evolve over time [63].

$$= y_0 + L_D \otimes [a(Q)\delta(\omega) + (1 - a(Q))L_a] \otimes [b(Q)\delta(\omega) + (1 - b(Q))L_b] \ . \tag{3.47}$$

L_i are Lorentzian functions described by the FWHM, Γ_i.

The heterogeneous scenario is, instead, based on the assumption of the existence of clusters, each one characterized by its own velocity that yields to a separation of regions with faster dynamics from ones with slower dynamics. In such case not all the molecules perform the same motions, a percentage of them realize faster movement respect the others. These kinds of regions in which a group of molecules have the same dynamics are called "island of mobility" (see Figure 3.15). In this case the scattering function is:

$$\begin{aligned} S_{HT}(Q,\omega) = y_0 + \left[\delta(\omega) + \left(\frac{\Gamma_D}{\omega^2 + \Gamma_D^2}\right)\right] \otimes \Bigg\{ P\left[a(Q)\delta(\omega) + (1 - a(Q))\left(\frac{\Gamma_a}{\omega^2 + \Gamma_a^2}\right)\right] \\ + (1 - P)\left[b(Q)\delta(\omega) + (1 - b(Q))\left(\frac{\Gamma_b}{\omega^2 + \Gamma_b^2}\right)\right] \Bigg\} \end{aligned}$$

$$\begin{aligned} = y_0 + L_D \otimes \big\{ & P\left[a(Q)\delta(\omega) + (1 - a(Q))L_a\right] \\ & + (1 - P)\left[b(Q)\delta(\omega) + (1 - b(Q))L_b\right] \big\} \ . \end{aligned} \tag{3.48}$$

For what concerns the localized motions is possible to note that the heterogeneous model has the same dynamic of the homogeneous one but with different percentages,

described by the parameter P.

In both models the first term L_D represents the movement associated with the translational diffusion. The spectral width of the Lorentzian associated with such motion has a quadratic Q-dependence, $\Gamma_D = DQ^2$, where D is the translational diffusion coefficient. The other two motions, L_a and L_b, are the localized movements and describe two movements that take place at different time scale. In both cases, the form factors $a(Q)$ and $b(Q)$ relative to these dynamics give a measure of the length scales associated with the localized movements.

3.5.3 Isotropic vs Anisotropic rotational model

In the isotropic rotational diffusion model, the molecular reorientation occurs via random small angle rotations. The average on time, being in the presence of random rotations, provides no preferential orientation for the molecule. Here we will present only the main results of the model developed by Sears [64]. The relative ISF is written:

$$I_{iso}(Q,t) = \sum_{l=0}^{\infty}(2l+1)j_l^2(Qr)e^{-l(l+1)D_R t} \ , \tag{3.49}$$

in which D_R is the rotational diffusion coefficient and $j_l^2(Qr)$ are the spherical Bessel functions. The time-Fourier transform of eq. (3.49) gives the scattering function in the form:

$$S_{iso}(Q,\omega) = A_0(Q)\delta(\omega) + \sum_{l=1}^{\infty} A_l(Q)\frac{l(l+1)D_R}{\omega^2 + \left[l(l+1)D_R\right]^2} \tag{3.50}$$

with

$$A_0(Q) = j_0^2(Qr) \qquad \text{and} \qquad A_l(Q) = (2l+1)j_l^2(Qr) \ . \tag{3.51}$$

The characteristic time for the isotropic motions is defined as, $\tau_{iso}^{-1} = l(l+1)D_R$.

Besides the isotropic model, we tested an anisotropic model. The calculation of this type of model that considers all possible orientations, is a difficult many-body problem and being described in many textbooks, only the relations used in the present study will be presented . An anisotropic rotational diffusion model lead us to write:

$$I_{ani}(Q,t) = \sum_{l=0}^{\infty}\sum_{m=-l}^{l} A_l e^{-\Gamma_l^m t} \ , \tag{3.52}$$

where $\Gamma_l^m = l(l+1)D_z + m^2(D_z - D_x)$. Time Fourier transform of $I_{ani}(Q,t)$ gives the

scattering function $S(Q,\omega)$, that, in the anisotropic case, is:

$$S_{ani}(Q,\omega) = A_0\delta(\omega) + \sum_{l=1}^{\infty} A_l \sum_{m=-l}^{l} \frac{l(l+1)D_z + m^2(D_z - D_x)}{\omega^2 + \left[l(l+1)D_z + m^2(D_z - D_x)\right]^2} \ . \tag{3.53}$$

We can note that the two scattering functions are expressed as a sum of infinite contribution. Expanding the sum in (3.50) and in (3.53) only till the second term we get:

$$S_{iso}(Q,\omega) = A_0\delta(\omega) + A_1 L(2D_R) + A_2 L(6D_R) \tag{3.54}$$

$$S_{ani}(Q,\omega) = A_0\delta(\omega) + 2A_1 L(D_z + D_x) + A_2 L(2D_x) \ . \tag{3.55}$$

In the anisotropic case the rotational diffusion coefficients D_x and D_y are considered equal, but they differ from D_z. This assumption, in the case of ClA, is justified by the value of the inertia momenta, in fact, $I_x \approx I_y \neq I_z$. The limit of isotropic rotation can be achieved if $D_z = D_x$.

Neutron diffraction

Neutron diffraction or elastic neutron scattering is a powerful tool to the determination of the atomic and/or magnetic structure of a sample. A diffraction experiment permit us to obtain a diffraction pattern that provides information about the structure of the material.

The formalism developed in the previous Sections finds an immediate application in the study of solid state. It is therefore necessary to consider the neutron scattering with respect to a solid with high-symmetry. However, since that the analysis of the scattering by a single crystal with one atom per unit cell has been treated in depth in numerous texts [34–38], the approach so far described will be applied to systems of most interest for the purposes of our discussion. The theoretical description is therefore focused on disordered and amorphous systems, materials in which it is not applicable the assumption of periodicity and long-range order. Therefore the solid is defined as a system in which each atom (or molecule) has a well-defined equilibrium position in relation to the time of measurement and does not include solids in which the atoms are subjected to translational diffusion.

3.5.4 Vibrations and harmonic approximation

Given the definition of solid, for each atom or molecule in the solid it is possible to associate an equilibrium position $\mathbf{r}_j$. The position can therefore be written as a function of the instantaneous displacement from the equilibrium site:

$$\mathbf{R}_j(t) = \mathbf{r}_j + \mathbf{u}_j(t), \qquad j = 1, \ldots, n \quad . \tag{3.56}$$

Using the equations corresponding to the coherent and incoherent scattering functions for a monatomic solid, we get:

$$S_{coh}(\mathbf{Q}, \omega) = \frac{1}{2\pi\hbar N} \sum_{j,k} \int_{-\infty}^{+\infty} \left\langle e^{-i\mathbf{Q}\cdot\mathbf{u_j(0)}} e^{i\mathbf{Q}\cdot\mathbf{u_k(t)}} \right\rangle e^{i\mathbf{Q}\cdot(\mathbf{r}_j - \mathbf{r}_k)} e^{-i\omega t} dt \tag{3.57}$$

and

$$S_{inc}(\mathbf{Q}, \omega) = \frac{1}{2\pi\hbar N} \sum_{j} \int_{-\infty}^{+\infty} \left\langle e^{-i\mathbf{Q}\cdot\mathbf{u_j(0)}} e^{i\mathbf{Q}\cdot\mathbf{u_j(t)}} \right\rangle e^{-i\omega t} dt \ . \tag{3.58}$$

Assume now that the forces acting in the solid are harmonics, i.e. they act, as a linear function of the displacement, so as to bring back each atom in its equilibrium position.

To evaluate the thermal average in the equations (3.57) and (3.58) we make use of the quantum theory of the simple harmonic oscillator.

$$\left\langle e^{-i\mathbf{Q}\cdot\mathbf{u_j(0)}} e^{i\mathbf{Q}\cdot\mathbf{u_k(t)}} \right\rangle = e^{-[W_j(\mathbf{Q})+W_k(\mathbf{Q})]} e^{\langle \mathbf{Q}\cdot\mathbf{u_j(0)}\mathbf{Q}\cdot\mathbf{u_k(t)}|\rangle} \ , \tag{3.59}$$

where the first factor, the *Debye-Waller factor*, is a function of Q.

$$e^{-W_j(\mathbf{Q})} = e^{-1/2\left\langle[\mathbf{Q}\cdot\mathbf{u_j(0)}]^2\right\rangle} \ . \tag{3.60}$$

For small displacements, the right-hand term can be expressed as:

$$e^{\langle \mathbf{Q}\cdot\mathbf{u_j(0)}\mathbf{Q}\cdot\mathbf{u_k(t)}\rangle} = 1 + \langle \mathbf{Q}\cdot\mathbf{u_j(0)}\mathbf{Q}\cdot\mathbf{u_k(t)}\rangle + \frac{1}{2!}\left\langle \mathbf{Q}\cdot\mathbf{u_j(0)}\mathbf{Q}\cdot\mathbf{u_k(t)}\right\rangle^2 + \dots \ . \tag{3.61}$$

The Debye-Waller factor is a multiplicative term to the cross section and for isotropic systems can be written:

$$2W(Q) = \frac{1}{3}Q^2\left\langle u^2\right\rangle \ , \tag{3.62}$$

where $\left\langle u^2\right\rangle$ is the mean-square displacement. This relation is widely used in the study of disordered materials.

3.5.5 Elastic events

Ignoring the time-dependent terms in eq. (3.61), the coherent scattering function becomes:

$$S^{el}_{coh}(\mathbf{Q},\omega) = \frac{1}{2\pi\hbar N}\sum_{j,k}\int_{-\infty}^{+\infty} e^{-[W_j(\mathbf{Q})+W_k(\mathbf{Q})]} e^{i\mathbf{Q}\cdot(\mathbf{r}_k-\mathbf{r}_j)} e^{-i\omega t} dt \tag{3.63}$$

$$= \left[\frac{1}{N}\sum_{j,k} e^{-[W_j(\mathbf{Q})+W_k(\mathbf{Q})]} e^{i\mathbf{Q}\cdot(\mathbf{r}_k-\mathbf{r}_j)}\right]\delta(\omega) \ . \tag{3.64}$$

The $\delta(\omega)$ describes a purely elastic scattering. The delta function is the result of the fact that in eq. (3.59) the correlation function remains finite at infinite time, and this describes the existence of a well-defined structure over time. The integration of (3.63) gives the elastic structure factor.

$$S^{el}(\mathbf{Q}) = \frac{1}{N}\sum_{j,k} e^{-[W_j(\mathbf{Q})+W_k(\mathbf{Q})]} e^{i\mathbf{Q}\cdot(\mathbf{r}_k-\mathbf{r}_j)} \ . \tag{3.65}$$

Similarly it is possible to obtain an expression for the incoherent scattering:

$$S^{el}_{inc}(\mathbf{Q},\omega) = \left[\frac{1}{N}\sum_{j} e^{-2W_j(\mathbf{Q})}\right]\delta(\omega) \ , \tag{3.66}$$

integrating over energies, gives:

$$S_{inc}^{el}(\mathbf{Q}) = \frac{1}{N}\sum_{j} e^{-2W_j(\mathbf{Q})} \ , \tag{3.67}$$

which contains an average of Debye-Waller factor for all atoms in the sample.

For a solid with a long-range order, the equilibrium positions $\mathbf{r}_j$ can be described by the relation $\mathbf{r}_j = \mathbf{r}_l + \mathbf{r}_d$, where $\mathbf{r}_l$ is related to the center of the unit cell and $\mathbf{r}_d$ to the relative position of a lattice position within the cell. In the presence of an atom of type d in the position $\mathbf{r}_d$, the set of vectors $\mathbf{r}_l$ describes a perfect crystal lattice. The elastic structure factor becomes:

$$S(\mathbf{Q})_{dd'}^{el} = \frac{(2\pi)^3}{V_0} e^{-[W_d(\mathbf{Q})+W_{d'}(\mathbf{Q})]} e^{i\mathbf{Q}\cdot(\mathbf{r}_{d'}-\mathbf{r}_d)} \sum_{\tau} \delta(\mathbf{Q}-\tau) \ , \tag{3.68}$$

where τ vectors are vectors of the reciprocal lattice and V_0 the volume of the unit cell. The equation (3.68) describes a series of peaks for each Q that is equal to a vector of the reciprocal lattice τ. These peaks are called Bragg peaks, and from eq. (3.68) it is possible to get the coherent elastic cross section

$$\left(\frac{d\sigma}{d\Omega}\right)_{coh}^{el} = \frac{(2\pi)^3}{V_0} \sum_{\tau} |F(\tau)|^2 \, \delta(\mathbf{Q}-\tau) \ , \tag{3.69}$$

where

$$F(\tau) = \sum_{\mathbf{r}_d} \bar{b_d} e^{-W_d(\tau)} e^{i\tau\cdot\mathbf{r}_d} \ , \tag{3.70}$$

that is the structure factor of the unit cell for the crystal. In the same way, the differential cross section of incoherent elastic is:

$$\left(\frac{d\sigma}{d\Omega}\right)_{inc}^{el} = \sum_{\mathbf{d}} c_{\mathbf{d}} \sigma_{inc}^{\mathbf{d}} e^{-2W_{\mathbf{d}}(\mathbf{Q})} \ . \tag{3.71}$$

In the interpretation of neutron diffraction data from crystalline solids is fundamental to note that eq. $\mathbf{r}_j = \mathbf{r}_l + \mathbf{r}_d$ assumes a single value of $\mathbf{d}$ relative to the center of the unit cell. If there is a change in values $\mathbf{d}$ through the crystal, the translational invariance is not guaranteed and it is necessary to consider eq (3.65). The presence of a translation and the loss of long-range order, as in the glasses and other amorphous materials, requires a knowledge of the time-average atomic positions to be able to calculate the $S(\mathbf{Q})$.

3.6 Diffractometers

Neutron diffraction is a very useful tool to investigate the structure of matter in a wide range of disciplines. There are two types of different diffraction instruments. One is the angle-scanning method with monochromatic neutrons, commonly used in steady-state sources. In such case the scattering vector, Q, is selected by changing the crystal angle and the scattering angle. The other, generally in pulsed neutron sources, is the wavelength-selection method by TOF. The scattering vector is scanned by changing the wavelength and keeping fixed the scattering angle. Both of them, of course, satisfy the Bragg's law, $Q = 4\pi \sin\theta/\lambda$.

3.6.1 High resolution neutron two-axis diffractometer *D1B*

$D1B$ is a two-axis neutron diffractometer positioned in the guide hall at the Institute Laue-Langevin (see Figure 3.16). It is dedicated to diffraction experiments requiring a high neutron flux. The high flux and the efficiency of its detector bank make it the appropriate instrument for a wide range of experiments with very small samples.

Three monochromators use the reflection [002] of pyrolitic graphite to provide a very high flux ($6.5 \cdot 10^6$ $n\mathrm{cm}^{-2}\mathrm{s}^{-1}$) focused onto the sample position with a wavelength of 2.52 Å. Using a germanium monochromator a second wavelength with $\lambda = 1.28$ Å is available. $D1B$ is furnished with microstrip $^3He/CF_4$ position sensitive detector covering in total 128 ° ranged from 0.8 to 128.8 ° in 2θ. The efficiency of the detectors at 2.52 Å is 86%, which means that they can detect the 86% of the scattered neutrons. A radial oscillating collimator (ROC) can be positioned between the sample and the detector bank for reducing the signal due to the non vanadium based sample environment [42, 65]. Due to the features of the instrument a complete scan of diffraction patterns with temperature can be obtained in few hours. In disordered systems as the plastic crystals the centers of mass of the molecules have a high positional symmetry and form a regular lattice. Such materials (as 1-Clhoroadamantane) have few distinct Bragg peaks that can be resolved through neutron diffraction and describe the its structure. Thanks to the temperature scans, structural changes of long range order could be followed over phase transitions. In 1-Clhoroadamantane measurements has been used an orange cryostat (1.7 to 300 K) and vanadium sample-cell with cylindrical geometry were used to measure the samples. To take into account all the spurious contributions,

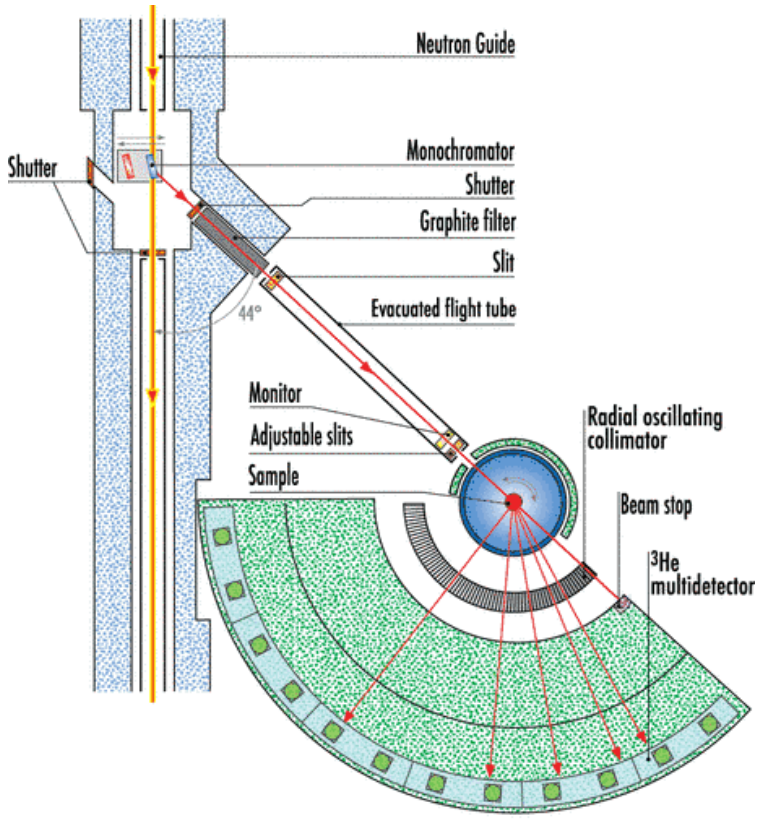

Figure 3.16: D1B experimental scheme [65]. Neutrons coming from the guide are monochromatized using the Bragg reflection over a crystal.

the empty cell and the empty instrument were measured to subtract to the sample.

3.7 Diffraction data refinement

Scattered neutrons that reach the detectors at D1B are affected by spurious contributions that are related to the signal coming from the sample. Such contributions have to be removed to get the diffraction pattern typical of the sample investigated.

The refinement has been performed using LAMP [66], permitting the manipulation of data in order to take into account the normalization to monitor counts, the different efficiencies of each detector cell, grouping of numors that correspond to the same measurement, and calculation of experimental errors.

Detector efficiency The detection system on D1B is composed by $^3He/CF_4$ position-sensitive detector formed by 1280 cells of 10 cm of height with a separation of 0.1°, covering an angular range of 128°. Nominally the detector efficiency is of 86% using $\lambda = 2.52$ Å [65], that means that detectors, not always catch the same number of neutrons.

To overcome this drawback, usually at each cycle beginning, a calibration is carried out so as to provide a measure of the efficiency of the detector. These values are used to correct the data detected by different detectors and possibly to discard malfunctioning cells. The workstation that controls D1B permits efficiencies on-line correction of raw data.

Monitor count normalization and raw data grouping Although the reactors involved in the experiments related to this work have a constant neutron flux, they may have small variations between different fuel cycles or even in the same cycle. Furthermore, if for the same sample we have measurements with different duration, the detectors will count more or less neutrons in dependence of the measurement time.

To consider these effects all measurements of D1B have been normalized to the number of neutrons to the monitor by means of macro implemented in LAMP. This number is proportional to the number of neutrons hitting the sample. In this way it is possible to compare data sets belonging to different cycles or characterized by distinct measurement times.

Each single raw data file is a measurement called *numor* (number of run). Usually to explore the entire scattering range, several short runs are taken rather than a unique long run. In this way it is possible to avoid problems that can occur during the measurement, in fact, if a numor has to be rejected it is always possible to reconstruct the whole scattering range.

Grouping procedure of different numors into a single measurement has been also done by a LAMP macro ("sumnum2fileD1B"). This calculation takes into account the offset angle of the detector bank during the measurement of each particular numor and the detector geometry.

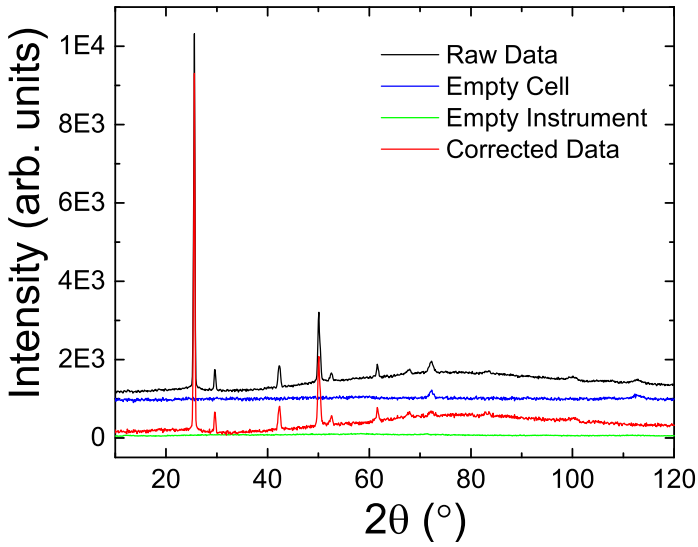

Figure 3.17: Example of data reduction for a diffraction spectrum of 1-chloroadamantane at $T = 260$ K. Subtraction of spurious contributions as the empty cell and the empty instrument give the corrected data ready to be analyzed.

3.7.1 Data treatment performed with FULLPROF

All the corrections and normalizations performed with the program LAMP have permitted to get a diffraction pattern of the neutrons scattered by the sample and by other contributions. It is then necessary a further data treatment to eliminate the spurious contributions and obtain the spectra relative only to the sample. The FULLPROF software package [67] has been used to perform the background and empty cell attenuation corrections to the diffraction data.

Non-sample contributions and multiple scattering Contributions that arise from the sample environment and the sample container must to be removed to get the sample contribution.

Even if in D1B the radial oscillating collimator (ROC), placed between the sample and the detector bank, reduces considerably the signal of the environment, measurements of the empty instrument (cryostat or furnace) and of the empty cell have been performed to eliminate the background and container contributions (Figure 3.17).

Generally, if the sample is considered point-like or very small, the free path of neu-

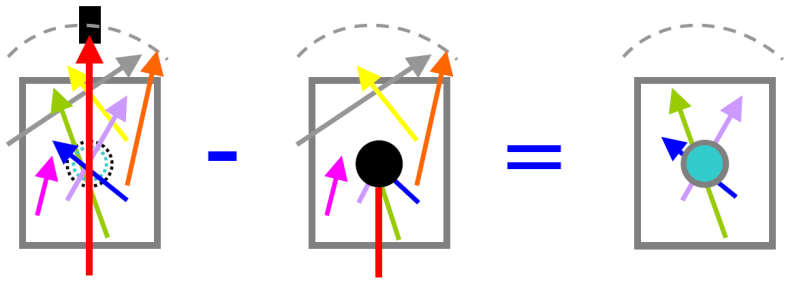

Figure 3.18: The contribution to the background of the neutrons passing through the sample can be obtained by the subtraction of the empty cell I_C and the absorber material I_A [54].

trons before the interaction with the sample will be bigger with respect to the sample dimensions. Under such condition the majority of neutrons will not interact with the sample and a small part of them will interact only once. However, in the real case incident neutrons can undergo two different processes: absorption or multiple scattering. Even if in our case the subtraction of the empty instrument and the empty container has been enough to extract the diffraction pattern, a description of such further corrections will be given.

The absorption measurement is usually carried out with a highly absorbing material with the dimensions of the sample holder and placed at the sample position. This permits to measure the contribution of those neutrons that do not pass through the sample position and hence are not affected by its presence. Subtracting it to the total background we have background contribution of neutrons that pass only through the sample (Figure 3.18). The effective background contribution I_B is then:

$$I_B = I_A + T(I_C - I_A) \ , \tag{3.72}$$

in which I_A is the intensity of the absorber (neutrons not passing at the sample position), I_C is the intensity of the empty cell (background contribution without the sample) and T is the transmission coefficient of the sample.

Using the Paalman and Pings algorithm [57] is then possible to calculate the attenuation correction. To determine the attenuation coefficients the geometry, the absorption and scattering cross section of the sample and the sample holder must be known. The

approach described does not take into account the effects due to multiple scattering.

Due to the geometry and composition dependence, multiple scattering contribution of both sample and cell is quite difficult to determine. Generally it can be calculated numerically assuming isotropic and elastic scattering [68–70] or by means of Monte Carlo simulation that gives a more precise results [71, 72].

Finally to determine the height, width and position of the reflection peaks, the corrected diffraction pattern has been analyzed using the Rietveld refinement method implemented in FULLPROF software [67, 73].

Chapter 4

Broadband dielectric spectroscopy

4.1 Electrostatics

Applying an electric field to a dielectric, the atomic and molecular charges inside dielectric are displaced or reoriented with respect to their equilibrium position, causing the polarization of the material and the formation of macroscopic dipole moment.

Let us define the displacement field $\mathbf{D}$ as:

$$\mathbf{D} = \mathbf{P} + \varepsilon_0 \mathbf{E} \ , \tag{4.1}$$

where $\mathbf{P}$ is the polarization, defined as the average dipole moment per unit volume, that quantifies the capacity of a material to react to the application of an electric field. The relationship between the polarization $\mathbf{P}$ with the field $\mathbf{E}$ within the dielectric:

$$\mathbf{P} = \chi \varepsilon_0 \mathbf{E} \ , \tag{4.2}$$

Combining eq. (4.1) and eq. (4.2) we get $\mathbf{D} = \varepsilon_0 \varepsilon_r \mathbf{E}$, where ε_0 is the permittivity of vacuum and ε_r is the relative dielectric constant. The relative dielectric constant is defined as $\varepsilon_r = 1 + \chi$, in which χ is the susceptibility of the material (both are dimensionless).

Assuming that within the dielectric there are no free charges, the polarization $\mathbf{P}$ will be the sum of the polarization due to induced dipoles $\mathbf{P_i}$ plus a contribution due to the

permanent dipole $\mathbf{P_p}$. $\mathbf{P_i}$ is the sum of the electronic polarization $\mathbf{P_e}$, caused by the displacement of the electrons with respect to the nuclei, and the atomic polarization $\mathbf{P_a}$, due to the movement of the nuclei compared to other nuclei in the material. If the material has polar molecules, we must add another contribution to the polarization due to the preferential orientation of permanent dipoles with respect to the applied field, this contribution is called orientational polarization $\mathbf{P_o}$. The total polarization will therefore be given by:

$$\mathbf{P} = \mathbf{P_i} + \mathbf{P_p} = (\mathbf{P_e} + \mathbf{P_a}) + \mathbf{P_o} \ . \tag{4.3}$$

Taking into account the induced polarization caused by N induced dipoles per unit volume V, it is possible to express it as $\mathbf{P_i} = N/V\alpha_i\mathbf{E_{loc}}$, in which α is the polarizability and $\mathbf{E_{loc}} = \mathbf{E}+\mathbf{P}/3\varepsilon_0$ is the local field. Using $\mathbf{P} = \varepsilon_0(\varepsilon_r - 1)\mathbf{E}$ and substituting, Mosotti and Clausius [74, 75] deduced the relation between the polarization and macroscopic electric field:

$$\mathbf{P_i} = \frac{N}{V}\alpha_i\mathbf{E_{loc}} = \frac{N\alpha_i}{V}\left(\frac{\varepsilon_r + 2}{3}\right)\mathbf{E} \ , \tag{4.4}$$

that yields to the Clausius-Mosotti equation:

$$\frac{\varepsilon_r - 1}{\varepsilon_r + 2} = \frac{N\alpha_i}{3V\varepsilon_0} \tag{4.5}$$

Considering now the macroscopic volume density of all N permanent dipoles per unit volume V, we define the orientational polarization, $\mathbf{P_o}$, as:

$$\mathbf{P_o} = \frac{\sum_i \boldsymbol{\mu_i}}{V} = \frac{N\langle\boldsymbol{\mu}\rangle}{V} \ , \tag{4.6}$$

where $\langle\boldsymbol{\mu}\rangle$ is the mean dipole moment. It depends on the interaction between the local electric field and the dipoles.

Assuming that the dipole are no-interacting, then the local field is equal to the macroscopic external electric field, and the mean dipole moment depends on the interaction energy of a dipole in the electric field ($W = -\boldsymbol{\mu}\cdot\mathbf{E}$) and on the thermal energy. Using the Boltzmann statistics:

$$\langle\boldsymbol{\mu}\rangle = \frac{\int_{4\pi}\boldsymbol{\mu}\exp\left(\frac{\boldsymbol{\mu}\cdot\mathbf{E}}{k_BT}\right)d\Omega}{\int_{4\pi}\exp\left(\frac{\boldsymbol{\mu}\cdot\mathbf{E}}{k_BT}\right)d\Omega} \ , \tag{4.7}$$

in which k_B is the Boltzmann constant, T the absolute temperature. The only contribution is due to the parallel component to the electric field, in fact $W = \mu E\cos\theta$, being

θ the angle between the dipole moment orientation and the electric field direction. If W is smaller with respect the thermal energy, eq. (4.7) reduces to:

$$\langle \mu \rangle = \frac{\mu^2}{3k_B T}\mathbf{E} = \alpha_0 \mathbf{E} \ , \tag{4.8}$$

with α_0 that is the orientational polarizability.
Therefore the orientational polarization can be written:

$$\mathbf{P_p} = \mathbf{P_o} = \frac{N}{V}\alpha_o \mathbf{E_{loc}} = \frac{N}{V}\frac{\mu^2}{3k_B T}\mathbf{E_{loc}} \ . \tag{4.9}$$

Considering the contribution to the polarization due to the induced and the permanent dipoles, from eq. (4.4) and eq. (4.9) we get:

$$\mathbf{P} = \frac{N}{V}(\alpha_i + \alpha_o)\mathbf{E_{loc}} \ . \tag{4.10}$$

Since $\mathbf{E_{loc}} = \mathbf{E} + \mathbf{P}/3\varepsilon_0$ and $\mathbf{P} = \varepsilon_0(\varepsilon_s - 1)\mathbf{E}$, substituing in eq. (4.10):

$$\frac{\varepsilon_s - 1}{\varepsilon_s + 2} = \frac{N}{3V\varepsilon_0}(\alpha_i + \alpha_o) \ , \tag{4.11}$$

where ε_s is the static permittivity that takes into account the contributions given by the induced and permanent dipoles.

Because eq. (4.5) is valid only around 10^{12} and 10^{15} Hz that are the characteristic frequencies of ionic and electronic movements, ε_r can be substitutes by the constant value ε_∞ (Figure 4.1), so the Clausius-Mosotti equation can be rewritten:

$$\frac{\varepsilon_\infty - 1}{\varepsilon_\infty + 2} = \frac{N\alpha_i}{3V\varepsilon_0} \ , \quad \text{and eq. (6.1) becomes:} \quad \frac{\varepsilon_s - 1}{\varepsilon_s + 2}\frac{\varepsilon_\infty - 1}{\varepsilon_\infty + 2} = \frac{N}{9V\varepsilon_0}\frac{\mu^2}{k_B T} \ . \tag{4.12}$$

The latter is the Debye formula and, considering permanent dipoles as non-interacting, describes the interaction between induced dipoles. Extending such result including the permanent dipole interaction [76] and writing in function of the dielectric strength $\Delta\varepsilon$:

$$\Delta\varepsilon = \varepsilon_s - \varepsilon_\infty = \frac{F}{3\varepsilon_0}\frac{N}{V}\frac{\mu^2}{k_B T} \ , \qquad \text{with} \qquad F = \frac{\varepsilon_s(\varepsilon_\infty + 2)^2}{3(2\varepsilon_s + \varepsilon_\infty)} \ . \tag{4.13}$$

A further correction was introduced by Kirkwood and Fröhlich [77–80] to model the interactions between dipoles respect the ideal case of non-interacting dipoles [41]. They introduced the correlation factor g given by:

$$g = \frac{\left\langle \sum_j \boldsymbol{\mu_j} \sum_k \boldsymbol{\mu_k} \right\rangle}{N\mu^2} = \frac{\mu^2}{\mu_{gas}^2} \ , \tag{4.14}$$

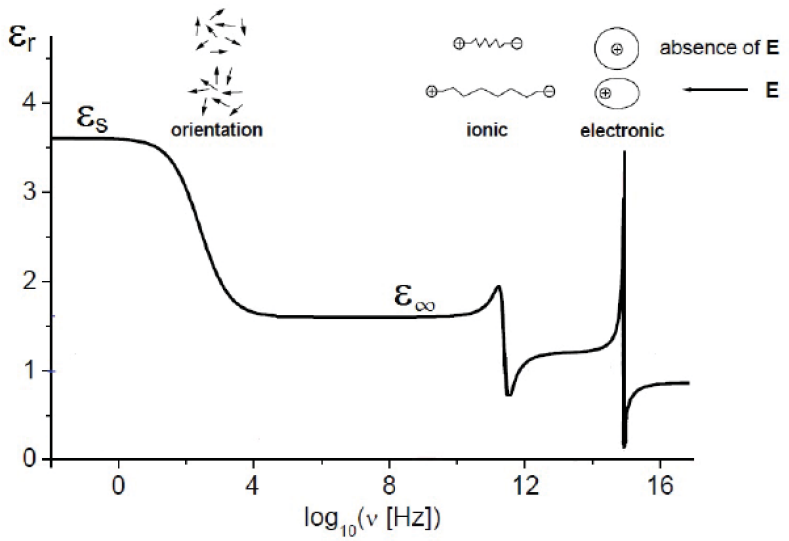

Figure 4.1: Kinds of polarization and corresponding dielectric constant ε_r as a function of frequency [41].

where μ_{gas}^2 is mean square dipole moment for non-interacting dipoles, that can be measured in the gas phase or in dilute solutions. A first procedure to calculate g and for practical calculation is to consider only the first neighbors of a given dipole. In that way g can be approximated by:

$$g = 1 + Z\langle\cos\varphi\rangle \ , \tag{4.15}$$

with Z coordination number and φ is the angle between the test dipole and one of the neighbors. Correlation factor g will differ from 1 when $\langle\cos\varphi\rangle \neq 0$ that is, when there is a correlation between the orientations of neighboring molecules. When $\langle\cos\varphi\rangle > 0$ and $g > 1$, molecules tend to direct themselves with parallel dipole moments, while when $g < 1$, molecules arrange themselves with antiparallel dipoles. If there is no specific correlation, then $g = 1$. If the correlations are not negligible, detailed information about the molecular interactions is required for the calculations of g, but being difficult to calculate theoretically, it can be experimentally estimated from the value of the dielectric strength:

$$\Delta\varepsilon = \varepsilon_s - \varepsilon_\infty = \frac{F}{3\varepsilon_0} g \frac{N}{V} \frac{\mu^2}{k_B T} \ . \tag{4.16}$$

The correlation factor is extremely useful in understanding the short-range molecular mobility and interactions in self-assembled systems.

4.2 Dielectric relaxation

Within the linear response theory, dielectric relaxation for small electric field strengths is a particular case. Applying an external field to a dielectric, the polarization reaches its equilibrium value, not instantaneously but after a period of time. This delay is mainly due to orientational polarization that is slower than the induced polarization, which reacts instantaneously to the application of the field. Likewise, when the field is switched off, the polarization decay caused by thermal motion follows the same law as the relaxation or decay function of dielectric polarization $\phi(t)$:

$$\phi(t) = \frac{\mathbf{P}(t)}{\mathbf{P}(0)} \ , \tag{4.17}$$

where $\mathbf{P}(t)$ is the time-dependent polarization vector. If a stationary periodic field $E(t) = E_0 \exp(i\omega t)$ is used, where ω is the angular frequency, eq. (4.2) becomes:

$$\mathbf{P}(\omega) = \chi(\omega)\varepsilon_0\mathbf{E}(\omega) \qquad \Rightarrow \qquad \mathbf{D}(\omega) = \varepsilon_r(\omega)\varepsilon_0\mathbf{E}(\omega) \ , \tag{4.18}$$

$$\text{with} \qquad \varepsilon_r(\omega) = \varepsilon^*(\omega) \quad = \quad \varepsilon'(\omega) - i\varepsilon''(\omega) \ . \tag{4.19}$$

The latter is a general expression of the complex dielectric function. The real part, named *permittivity*, is a measure of the energy stored in the system, while, the imaginary part, called *dielectric loss*, is proportional to the energy dissipated in the material.

Plotting $\varepsilon''(\omega)$ vs $\log(\omega)$ we get an asymmetric peak shape (Figure 4.2) whose position gives the characteristic relaxation time τ that is dependent by the temperature T. The characteristics of the peak depend on the material under investigation and on the interactions between molecules and from such peak it is possible to extract information on molecular dynamics. Analyzing Figure 4.2, we can note that in correspondence of the peak the real part present a step-like behavior with height $\Delta\varepsilon = \varepsilon_s - \varepsilon_\infty$ that is related with the strength. ε_s that corresponds to the maximun value of the polarization is the static permittivity, while ε_∞ is the relaxed permittivity and represents the contribution to the total polarization due only to electronic and atomic effects.

It is necessary to take into account also the motion of the charges going down at low frequencies. The dielectric response of the material must thus include the contribution

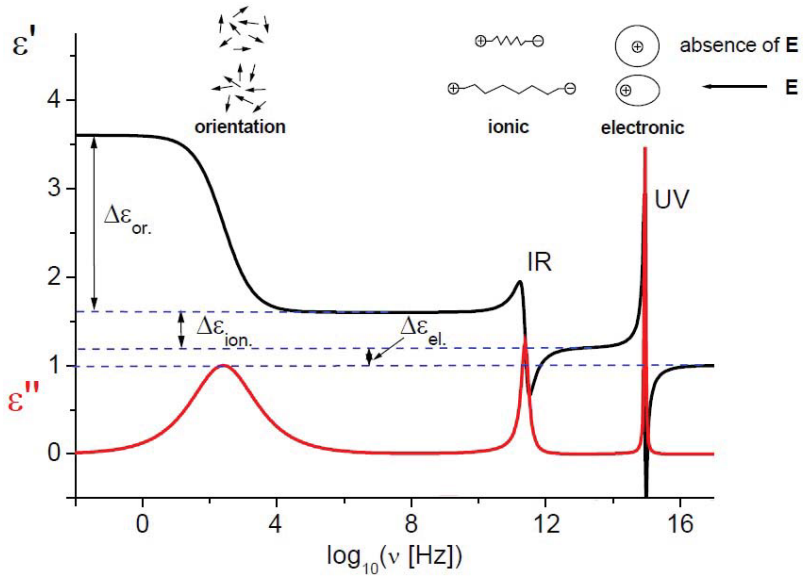

Figure 4.2: Types of polarization as a function of frequency. In figure are shown the real part, $\varepsilon'(\omega)$ (black line), and the imaginary part, $\varepsilon''(\omega)$ (red line), of the complex dielectric function [41].

of the conductivity. The relationship that links these two quantities is:

$$\sigma^* = i\omega\varepsilon_0\varepsilon^*(\omega) \ , \tag{4.20}$$

where σ^* is the complex conductivity. Considering all contribution we have to add a term to the imaginary part of the dielectric permittivity:

$$\varepsilon''(\omega) = \varepsilon_{or} + \frac{\sigma_0}{(\varepsilon_0\omega)^s} \ , \tag{4.21}$$

in which ε_{or} contains all the dielectric information, σ_0 is the DC conductivity and s is an exponent that indicates the ohmic ($s = 1$) or non-ohmic ($s < 1$) conduction character. In presence of an ohmic behavior, in the lower frequencies limit, the real part of ε^* does not depend on ω (Figure 4.3).

Another effect due to charges motion is the electrodes polarization (non-ohmic behavior), due to the formation of a charge layer at the electrode-sample interface that change the perception of the field by the sample and cause a change in the slope of the conductivity contribution (dashed lines in Figure 4.3). Since this effect do not affect the sample, it is normally not considered.

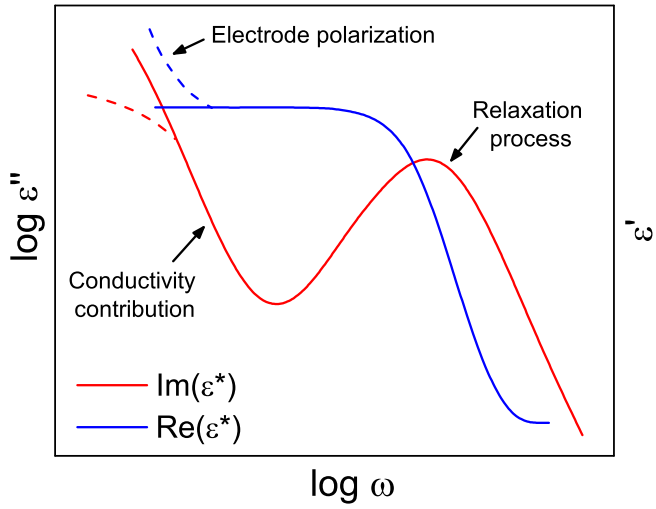

Figure 4.3: Diagram of the real $\varepsilon'(\omega)$ (solid blue line) and the imaginary $\varepsilon''(\omega)$ part (solid red line) of the complex dielectric function for a relaxation process and an ohmic conductivity. In the case of a non-ohmic conductivity (dashed lines) it is observed the electrode polarization.

4.3 BDS equipment

Dielectric spectroscopy technique is particularly suited for the investigation of the molecular dynamics. This is due to the wide frequency range (between 10^{-6} Hz and 10^{15} Hz) accessible by this technique [41, 81, 82].

The dielectric spectroscopy is normally performed in the frequency domain, and by varying the frequency of the applied AC field it is possible to carry out the measurements, but anyway one has to choose the appropriate configuration depending on the frequency range that one wants to explore (Figure 4.5).

The quantity to measure is the complex impedance $Z^*(\omega)$ of the sample that is linked to the complex dielectric permittivity by:

$$\varepsilon^*(\omega) = \frac{1}{i\omega Z^*(\omega) C_0} \ . \tag{4.22}$$

in which C_0 is capacitance of the capacitor in the vacuum.

An experimental layout is shown in Figure 4.6, where the temperature control is achieved by means of a nitrogen-gas heating/cooling system. Such system is the Novocontrol Quatro Cryosystem [83, 84]. It is composed by a cryostat where the sample

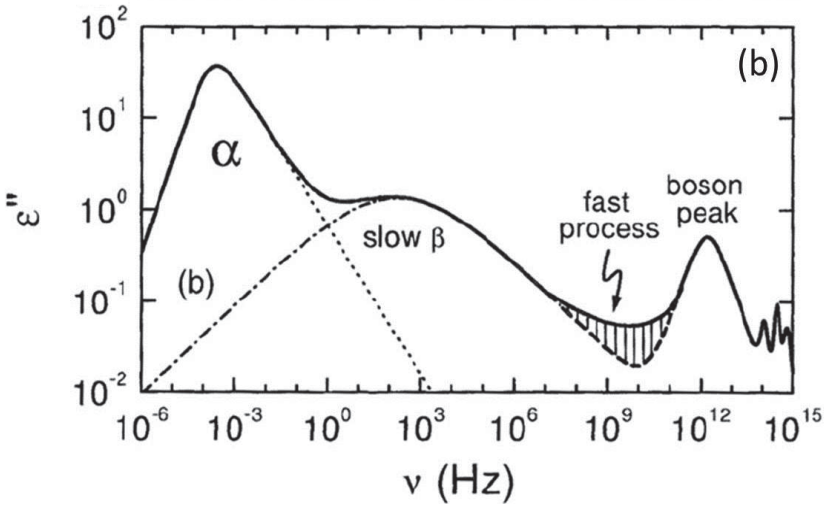

Figure 4.4: Schematic representation of the frequency dependence of the dielectric loss of a supercooled material near the glass transition temperature. The response of a glass presents well-defined peaks [41].

holder can be placed for the measurements, a gas heating unit, a liquid nitrogen unit and a liquid nitrogen Dewar with vacuum system and pressure control (see Figure 4.6). Temperature is determined by the use of a resistor sensor made of Pt ($PT100$) always in contact with the capacitor. The system has an accuracy of 0.01 K and operates between 116 and 773 K.

The Alpha-analyzer was also used with a second cryostat connected to a closed-cycle helium compressor. This cryostat, that originally was employed to produce liquid nitrogen, has been modified to use it as a vacuum chamber with temperature control (in this case we have to use an hermetic capacitor). The helium cryostat permits to reach very low temperature (thermal range is between 16 and 320 K). For these kind of measurements the capacitor stays directly on the top of the cold finger inside the cryostat where a diode sensor, placed inside the cold finger, is used to determine the temperature with a precision of the order of ≈ 10 m K.

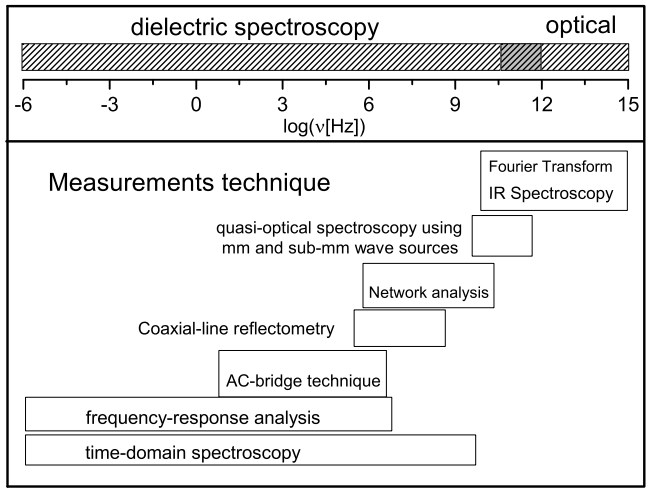

Figure 4.5: Different measurements techniques in the typical frequency range accessible ($10^{-6} - 10^{15}$ Hz) for a BDS experiment.

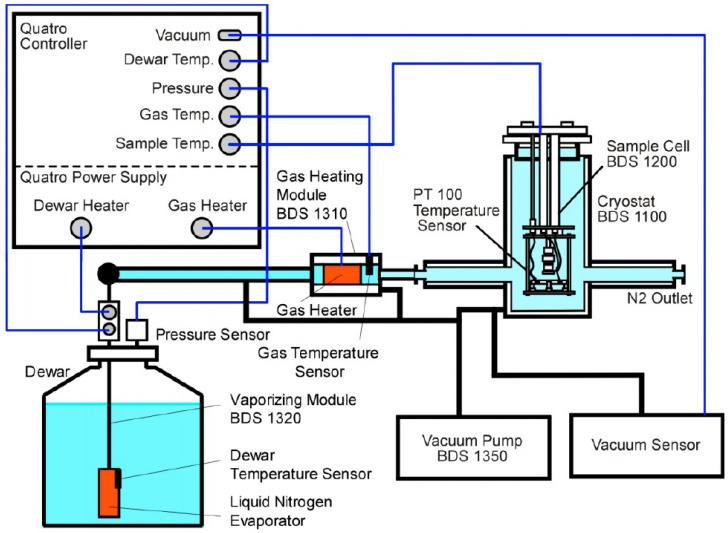

Figure 4.6: A heating device controls the pressure in the liquid nitrogen Dewar vessel to create a constant nitrogen stream. Two channels of the Quatro controller are designed to control pressure and temperature in the Dewar vessel. The nitrogen stream flows directly through the sample cell placed in the cryostat. Other two channels are devoted to the measure of the gas and sample temperatures.

4.4 BDS data correction

Measurement procedures, registration and storage are carried out automatically in the modern BDS systems. The measurements are performed in an on-line mode and the results can be shown in both frequency and time domain. There are several features of the modern software that control the process of measurement and calibration. The calibration parameters can be saved in a configuration file, allowing further measurements using the same parameters and without additional calibration. Data processing software generally includes the options of signal correction, such as correction of DC-conductivity and electrode polarization. The control of the analyzers or the temperature systems and the data treatment are often performed by means of different software programs. The Novocontrol software [83] contains all the features of practical importance.

WinDETA is implemented in the Novocontrol software and performs the measurement control, basic data evaluation and data representation. All devices are controlled by an unique user interface. WinDETA supports value lists for the independent quantities such as frequency and temperature. Temperature control is performed automatically and heating or cooling rates can be set. From the measurements of impedance all dielectric quantities like the dielectric spectra, conductivity, etc. are determined. Data, exported as ASCII files, have been analyzed with FABADA software (see Chapter 5).

DC-conductivity problem. The conductivity contribution in dielectric experiments is often an unwelcome phenomenon caused by the presence of charged impurities in the sample. In the frequency domain the DC-conductivity σ_0 provides to the imaginary part ε'' an additional term $\sigma_0/(\varepsilon_o\omega)$. This term makes difficult the relaxation processes analysis mostly when the conductivity contribution is greater than the amplitude of the relaxation and processes are present in the low frequency range. Even if in our case the conductivity is well separated from the relaxation processes encountered some details of such kind of correction will be given.

The modulus representation $M^*(\omega) = 1/\varepsilon^*(\omega)$ of dielectric data is one of the most efficient way for the analysis of DC-conductivity, since it transforms in a defined peak the power law behavior of the conductivity [85]. However, there are several problems in using such representation especially when the conductivity peak overlaps with the relaxation process. Since in such a situation the shape and position of the relaxation

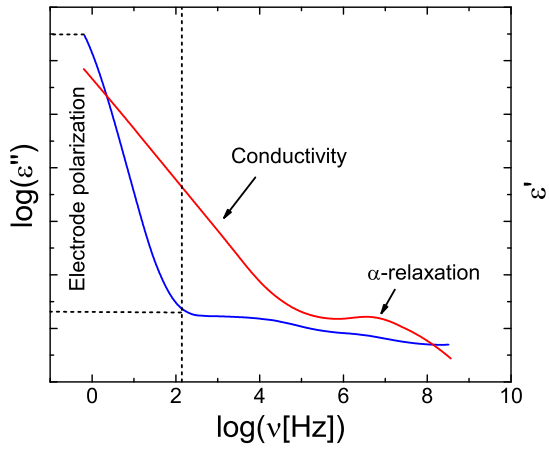

Figure 4.7: Electrode polarization is highlighted by the strong increase of the real part (blue line) of the dielectric complex function (ε'). It is shown also the imaginary part ε''.

peak depend on the conductivity, the real component of the modulus, that contains the DC-conductivity, does not permit to discriminate between different relaxation processes.

On the other hand the Kramers-Kronig relation [86] links the real and the imaginary part of the complex dielectric function. Since DC-conductivity is contained only in the imaginary part of the complex dielectric permittivity the conductivity can be calculated directly by means of the Hilbert transform.

Electrode polarization. This effect is a parasitic phenomenon that affects dielectric measurements masking the signal of the sample [41]. It is due to the stop of charges at the sample-electrode interface, where the separation between positive and negative charges causes an additional polarization. The magnitude and the frequency position of the electrode polarization are dependent from the conductivity of the sample.

To have only the signal coming from the sample, the contribution of the electrode polarization must be eliminated. Methods to determine this contribution are based on the model description of such process or there are estimation that can be subtracted to the data.

Electrode polarization can be seen as a large step of $\varepsilon'(\omega)$ at low frequencies. Since electrode polarization does not contain information about the sample, the part with the

electrode polarization is often not taken into account for the analysis (see Figure 4.7).

4.5 Relaxation models for dielectric data

The complex dielectric function, and consequently its real and imaginary parts have a specific frequency and temperature dependence. The features of such dependence originate from different processes, such as:

1. the motion flow of mobile charge carriers (translational diffusion);
2. microscopic movements of molecular dipoles (rotational diffusion);
3. the charge separation at the interfaces that leads to an additional polarization.

As stated in Chapter 4.2 the relaxation process is characterized by a step-like evolution of the real part (ε') and by a peak in the imaginary part (ε'') of the complex dielectric function (Figure 4.8). The information concerning the dynamics of a molecular group can be obtained by analyzing the dielectric function, this is because dipoles can be connected directly to the entire molecule or to a part of it (chemical groups, etc.). Therefore, the characteristic shape of the dielectric function depends on the correspondence between the frequency ($\nu = \omega/2\pi$) of the external field applied and the characteristic time τ of movements of the molecular dipoles. The information needed to describe a dielectric relaxation can be extracted by the evolution of the real and imaginary parts of the dielectric function. The dielectric strength $\Delta\varepsilon$ can be determined by the height of the step in ε' or by the area under the peak in ε''. The frequency of maximum loss ν_p is related to the characteristic relaxation time $\tau_p = 1/\omega_p$ of the dipoles. From the shape of the loss peak it is possible to derive the distribution of relaxation times.

In the description of the loss peak (connected with dielectric relaxation), a single lineshape function or a combination of several functions can be used, permitting us to extract information, through the fitting procedure, about the dipolar molecular dynamics.

4.5.1 Debye relaxation

The simplest way to determine the time dependence of the dielectric behavior, was proposed by Debye. It is based on the assumption that the change of the polarization

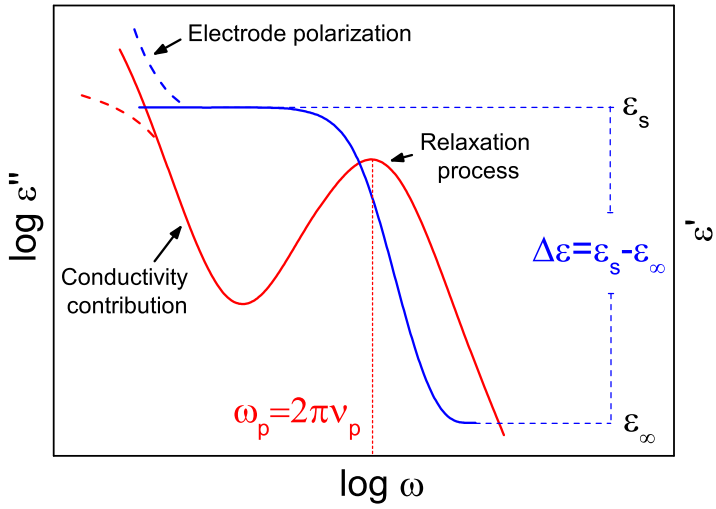

Figure 4.8: Real (solid blue line) and imaginary (solid red line) part of complex dielectric function as a function of normalized frequency. The figure shows the position of the maximum of the loss peak, ω_p, and the dielectric strength, $\Delta\varepsilon$.

is proportional to its actual value, and can be described by the following differential equation [41, 87]:

$$\frac{dP(t)}{dt} = -\frac{1}{\tau_D}P(t) \ . \tag{4.23}$$

In the previous equation τ_D is the characteristic relaxation time. For what concerns the correlation function $\phi(t)$, it is possible to note that can be derived from eq. (4.23) and leads to a simple exponential decay:

$$\phi(t) = \frac{\langle \Delta P(t)\Delta P(0)\rangle}{\langle \Delta P(0)^2\rangle} = \exp\left[-\frac{t}{\tau_D}\right] \ . \tag{4.24}$$

The validity of this hypothesis is verified when: (1) the dipoles do not interact, (2) the equilibrium is achieved through a unique process, (3) all the dipoles are considered equivalent, and therefore the characteristic time is common to all molecules.
In any case, in the limit $t \to 0$ the correlation function described by eq.(4.24) does not satisfy the mathematical conditions required and it is replaced by a Gaussian function.

The complex permittivity as a function of frequency assumes the form [80]:

$$\varepsilon^*_{Debye}(\omega) = \varepsilon_\infty + \frac{\Delta\varepsilon}{1 + i\omega\tau_D} \ , \tag{4.25}$$

that is known as the Debye equation. Eqs. (4.24) and (4.25) are linked by a Fourier

transform, in fact:

$$\frac{\varepsilon^* - \varepsilon_\infty}{\Delta\varepsilon} = \frac{1}{1 + i\omega\tau_D} = \Phi^*(\omega) = \mathcal{F}\left[-\frac{d\phi(t)}{dt} \right] . \tag{4.26}$$

The real and the imaginary part of the complex dielectric function can be separated in two contributions:

$$\begin{aligned} \varepsilon'(\omega) &= \varepsilon_\infty + \frac{\Delta\varepsilon}{1 + (\omega\tau_D)^2} \\ \varepsilon''(\omega) &= \Delta\varepsilon \frac{\omega\tau_D}{1 + (\omega\tau_D)^2} , \end{aligned} \tag{4.27}$$

where $\Delta\varepsilon = \varepsilon_s - \varepsilon_\infty$ is the dielectric strength with ε_s and ε_∞ that are the low and high frequency limits of dielectric constant, determined by all slower and faster processes that are present in the material under investigation, and the characteristic time τ_D is linked to the position of the maximum of the loss peak through $\omega_p = 2\pi\nu_p = 1/\tau_D$. The loss peak (Figure 4.9) is a symmetric peak with a half width ω_D of 1.14 decades.

4.5.2 Non-Debye relaxation

Usually dielectric functions are broader than that predicted by the Debye function and also present an asymmetric peak. Therefore the dielectric relaxation can not be described by equations (4.24) and (4.25). Several functions have been developed for non-Debye relaxation behavior.

A symmetric broadening of ε'' can be described by the **Cole-Cole** (CC) function (Figure 4.9) [88]:

$$\varepsilon^*_{CC}(\omega) = \varepsilon_\infty + \frac{\Delta\varepsilon}{1 + (i\omega\tau_{CC})^\alpha} . \tag{4.28}$$

In this case the real and the imaginary part of (4.28) are:

$$\begin{aligned} \varepsilon'(\omega) &= \varepsilon_\infty + \frac{\Delta\varepsilon(1 + \omega\tau_{CC})^\alpha \cos(\alpha\pi/2)}{1 + (\omega\tau_{CC})^\alpha \cos(\alpha\pi/2) + (\omega\tau_{CC})^{2\alpha}} \\ \varepsilon''(\omega) &= \Delta\varepsilon \frac{(\omega\tau_{CC})^\alpha \sin(\alpha\pi/2)}{1 + (\omega\tau_{CC})^\alpha \cos(\alpha\pi/2) + (\omega\tau_{CC})^{2\alpha}} . \end{aligned} \tag{4.29}$$

The parameter α varies in the range $[0, 1]$. The CC relaxation time τ_{CC} is related to the maximum of the loss peak by $\omega_{max} = 1/\tau_{CC}$. For $\alpha = 1$ Debye relaxation is recovered.

Some samples as liquid and glass forming materials present an asymmetric peak, as shown in Figure 4.9. Such behavior can be described by **Cole-Davidson** (CD)

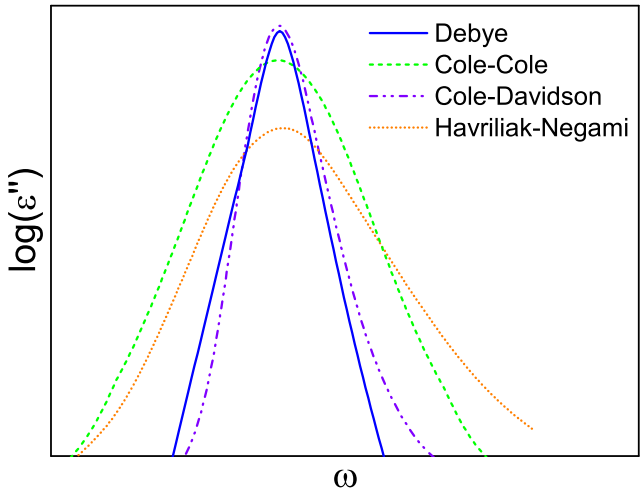

Figure 4.9: Dielectric loss spectra for different models: Debye (D, solid blue line), Cole-Cole (CC, dashed green line), Cole-Davidson (CD, point-dashed purple line) and Havriliak-Negami (HN, pointed orange line) functions. It is evident the difference in the width and the symmetry of such functions.

equation [89]:

$$\varepsilon^*_{CD}(\omega) = \varepsilon_\infty + \frac{\Delta\varepsilon}{(1+i\omega\tau_{CD})^\beta} \ . \tag{4.30}$$

β parameter ($0 < \beta < 1$) characterizes the asymmetric broadening of the loss peak for frequencies $\omega > 1/\tau_{CD}$, where τ_{CD} is the CD relaxation time related to the position of the peak maximum by $\omega_{max} = 1/\tau_{CD}\ \tan[\pi/(2\beta+2)]$. For $\beta = 1$ Debye function is achieved. The real and imaginary parts of CD function are given by:

$$\begin{aligned} \varepsilon'(\omega) &= \varepsilon_\infty + \Delta\varepsilon \cos(\omega\tau_{CD})^\beta \cos(\omega\tau_{CD}\beta) \\ \varepsilon''(\omega) &= \Delta\varepsilon \cos(\omega\tau_{CD})^\beta \sin(\omega\tau_{CD}\beta) \ , \end{aligned} \tag{4.31}$$

Generalizing, the description of relaxation is achieved by a combination of CC and CD functions, called **Havriliak-Negami** (HN) function [90, 91].

$$\varepsilon^*_{HN}(\omega) = \varepsilon_\infty + \frac{\Delta\varepsilon}{[1+(i\omega\tau_{HN})^\alpha]^\beta} \ , \tag{4.32}$$

where α and β vary between 0 and 1, and from them depend the position of maximal loss

$$\omega_{max} = \frac{1}{\tau_{HN}} \left[\sin \frac{\alpha\pi}{2\beta+2}\right]^{1/\alpha} \left[\sin \frac{\alpha\beta\pi}{2\beta+2}\right]^{-1/\alpha} . \tag{4.33}$$

The real and imaginary parts of the complex dielectric function are described by quite complex equations:

$$\begin{aligned} \varepsilon'(\omega) &= \varepsilon_\infty + \Delta\varepsilon\left[1 + 2(\omega\tau_{HN})^\alpha \cos(\alpha\pi/2) + (\omega\tau_{HN})^{2\alpha}\right]^{-\beta/2} \\ &\cdot \quad \cos\left[\beta \arctan\left(\frac{\sin(\alpha\pi/2)}{(\omega\tau_{HN})^{-\alpha} + \cos(\beta\pi/2)}\right)\right] , \\ \varepsilon''(\omega) &= \Delta\varepsilon\left[1 + 2(\omega\tau_{HN})^\alpha \cos(\alpha\pi/2) + (\omega\tau_{HN})^{2\alpha}\right]^{-\beta/2} \\ &\cdot \quad \sin\left[\beta \arctan\left(\frac{\sin(\alpha\pi/2)}{(\omega\tau_{HN})^{-\alpha} + \cos(\beta\pi/2)}\right)\right] . \end{aligned} \tag{4.34}$$

Debye relaxation is recovered for $\alpha = \beta = 1$. Only the HN-function is able to describe the data in the entire frequency range (Figure 4.9). This means that for a complete description of an isolated relaxation region is required at least a series of four parameters [41].

For the analysis of samples that present several relaxations it is necessary a sum of several contributions, each one described by one of the function showed above.

In several cases of non-Debye relaxation behavior in the time domain, the correlation function does not have the form of a simple exponential decay, it is then used the Kohlrausch-Williams-Watts (KWW) function [92]:

$$\phi(t) = \exp\left[-\left(\frac{t}{\tau_{KWW}}\right)^{\beta_{KWW}}\right] , \tag{4.35}$$

where τ_{KWW} represents the characteristic relaxation time and β_{KWW} is a stretching exponent ranging between 0 and 1 which depends on the material and on the external conditions such as temperature and pressure. Despite not having an analytical Fourier transform in the domain of frequency, KWW function and HN function are connected [93]. The exponents and the relaxation times of the two functions are related in the following manner:

$$\beta_{KWW} = (\alpha\beta)^{1/1.23} \tag{4.36}$$

$$\ln\left(\frac{\tau_{HN}}{\tau_{KWW}}\right) = 2.6(1-\beta_{KWW})^{1/2} e^{-3\beta_{KWW}} . \tag{4.37}$$

The validity of the aforementioned equations was tested by means of dielectric measurements, performed around the primary relaxation. However, these relations are not analytical, since, as already mentioned, the HN and KWW relaxation functions are not exactly the Fourier transforms of each other. In any case these are the most widely used relations in the experimental results reported in the literature.

4.5.3 Kinds of relaxations

The contributions due to the relaxation are fundamental features in the dynamics studies of glass-formers near the glass transition point. Let us distinguish now between the types of relaxation that we find by analyzing the dielectric spectroscopy data (Figure 4.4). The precise explanation of the origin of the relaxation peaks needs a very careful approach.

In many glass-forming systems the relaxation spectrum shows different relaxation processes "traditionally" termed α, β, γ etc. beginning with the higher temperature peak. This notation however does not concern with the mechanism behind such relaxations. It is possible, in fact, to distinguish between two types of mechanisms that plausibly play a role in this cooling process: (*i*) slow mechanisms, mainly involving many molecules, that practically lead the structural relaxation, and (*ii*) fast interactions, which occur on a shorter timescales, that are characterized by relaxation processes that are quick enough to remain in thermal equilibrium lowering the temperature (Figure 4.10) [94].

Thus, another notation is to call α-relaxation the process that yields to the determination of the glass transition temperature, while the sub-T_g transitions are called secondary relaxations and can display an intra- or inter-molecular character.

The α-relaxation

This kind of relaxation is strongly connected with the glass transition and describes the structural cooperative and collective rearrangement of molecules. This structural α-peak displays an evolution to high frequencies with the increase of the temperature. The α relaxation is related with viscosity, that is perhaps the less understood of glass properties despite its ubiquitous operational use in industry.

As said in Chapter 1, the point at which the viscosity, or relaxation time, reach

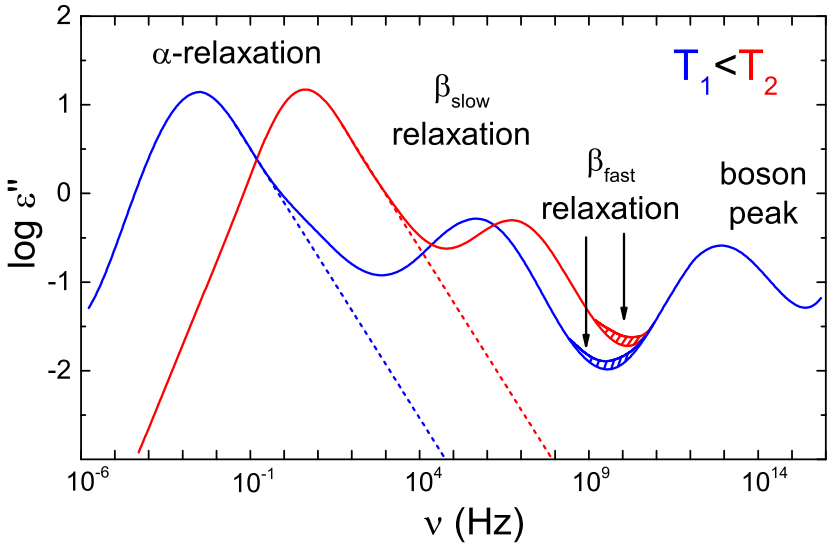

Figure 4.10: Diagram of the dynamics processes present in glass former. A dielectric loss spectrum for two temperatures is shown: the dynamic glass transition (α-relaxation), the slow β-relaxation, the fast β-process and the boson peak. It is important to note that not all these loss processes are always present in a glass-forming system [41].

10^{12} Pa s or 100 s, respectively, is called the glass transition temperature. This transition temperature discriminates between a glass and an undercooled liquid. There are two typical phenomenological behaviors of the viscosity as a function of the temperature, as temperature decreases towards the glass transition, that have been identified so far. The first one is the so-called Arrhenius relaxation, according to which the viscosity grows exponentially at a low temperature, whereas the second one is the Vogel-Fulcher law, that diverges even faster than the Arrhenius one. Both laws indicate a very large increase in viscosity or, equivalently, in relaxation time, preventing the material from reaching thermal equilibrium. During the last decades two categories of glasses have been distinguished according to the above-mentioned temperature dependence around the glass transition: the strong glasses and the fragile glasses. The materials belonging to the Arrhenius family are designated as strong, while the materials whose viscosity follows the Vogel-Fulcher law are designated as fragile.

Secondary relation processes

In dielectric loss spectra ε'', a second peak in addition to that related to the α relaxation is present. Depending on temperature, it is mostly observed in the Hz − MHz range, at frequencies beyond that of the α peak. All the processes that take place sub T_g are called secondary relaxations. Usually, these kind of relaxations show smaller strength with respect the α peak. In general, this secondary relaxation is called β relaxation and it can be divided in slow and fast relaxations. This subdivision depends on the values of their relaxation times [94].

Typically the slow secondary β process shows a symmetric loss profiles, an Arrhenius temperature dependence of the relaxation time and they they are also present below the glass transition temperature T_g. The origin of such process is frequently adduced to the motion of polar side groups or to some internal conformational molecular change, even if, Johari and Goldstein [95] have demonstrated that these kind of relaxations are present also in rigid molecules, where internal modes are absent and in some polymers where there are not rotable side group [96]. Such kind of relaxation is strictly connected to the glassy phase and is called JG β relaxation [94,97–100] (different from the relaxation caused by the internal motions). Currently there is no an accepted physical theory able to explain the origin of JG relaxation. A trial has been done considering the relaxation that comes from molecules with higher mobility in confined regions, the so-called "islands of mobility" [95,101–103].

Another process is present in the GHz − THz range. Such contribution is supposed to arise from the "rattling" movement of a particle in the transient confinement formed by its neighbors and is stable on a short time scale. It is called "fast β relaxation" [104–109]. It should be noted that the fast β process is not identical with the JG β relaxation.

A further peak, named Boson peak, is visible over the terahertz frequency region. Although it seems to be linked to the inter-atomic vibrational mode there are no satisfactory explanations of the origin of this relaxation. Several models have been proposed to explain its existence, among others the MCT [110].

Chapter 5

Analysis methods

An overview on the analysis methods used in the thesis will be given. Generally, data fitting is performed using a mathematical model that describes correctly the data and from which it is possible to extract the parameters which describe the physical process under consideration.

Typically this is done by a χ^2 minimization, that is fast and reliable when one has simple models, but that presents some problems in case of more complex models.

A Bayesian method for the exploration of the parameter space, that is based solely on the probability laws that underlie the χ^2 figure of merit, will be here presented. The ability to not get stuck in local minima of the parameter space, the possibility of taking into account the correlation between the parameters in a natural manner and the opportunity of showing the complexity of the problem by expressing the parameters through the probability distributions functions, make this method a very powerful tool for data analysis. The properties and the advantages of Bayesian approach contained in FABADA software, with which the fit procedure and the model selection have been performed, will be presented in the last part of this Chapter.

5.1 Frequentist vs Bayesian

Once the data have been corrected the process of data fitting is the common way to ascertain how well a model describes experimental data and get the parameters that characterize the physical processes. In the presence of various hypotheses one should

look to the one that better describes the results with the highest probability. However, it is necessary to take into account that increasing the number of elements of the hypothesis the description of data will be easier and more accurate. It is therefore necessary to find a hypothesis that has a good agreement with the data, but at the same time that is as simple as possible.

The most widely used methods are the Frequentist methods such as Levenberg-Marquardt, that are based on the minimization of a cost function, usually χ^2. In such cases the purpose is to obtain an agreement between the values of the parameters with their associated errors ($P_i \pm \varepsilon_i$) and the experimental data. To quantify the goodness of the agreement between the experimental data and the optimal values of the parameters it is used the minimum value of the cost function χ^2. Therefore one attempts to verify the validity of an hypothesis, which, in this case, can be described by a mathematical model. The problem arises from the fact that starting far away from global minimum or using a complex model, the Frequentist method could get stuck in local minima of the χ^2 hypersurfaces. This stems from the fact that such method assumes the existence of only one minimum in the $\chi^2\{P_i\}$ hypersurface, that the functional dependence of $\chi^2\{P_i\}$ is quadratic for each parameter (the error bars are therefore symmetrical) and that there is no correlation between the parameters.

Unlike Frequentist approximation, Bayesian inference does not make any assumption on the $\chi^2\{P_i\}$ landscape [111]. Bayesian analysis uses a completely different way to express the fitting parameters and a different figure of merit which describes the complexity of the problem under analysis. It makes use in fact of the probability distribution function (PDF) that can be obtained directly from the exploration of the $\chi^2\{P_i\}$ hypersurfaces.

The main differences between Bayesian approach with respect the Frequentist method are summarized in Table (5.1).

5.2 The χ^2 definition

Generally, to verify the goodness of the agreement between the experimental data and any model which describes them is done by the function called χ^2. Lower the value of χ^2 lower will be the difference between the data and the empirical model points.

Given a set of experimental data D_k ($k = 1, \ldots, n$), each one with its own error

Classical Method	Bayesian Inference
• Downhill changes of χ^2 are allowed	• Uphill changes of χ^2 are permitted
• Parameters expressed by $P_i \pm \varepsilon_i$	• Parameters are described by the PDF
• Correlations not considered	• Correlations are taken into account
• Invisible multiple minima	• Multiple minima are visible
• A χ^2 PDF is assumed	• No assumption is made on χ^2 PDF

Table 5.1: Main differences between Frequentist and Bayesian approaches.

σ_k $(k = 1, \ldots, n)$ and a set of points described by the hypothesis $H_k\{P_i\}$ $(k = 1, \ldots, n)$, which depend on the value of the parameters $\{P_i\}$ $(i = 1, \ldots, m)$, the χ^2 function is defined as:

$$\chi^2 = \sum_{k=1}^{n} \frac{(H_k\{P_i\} - D_k)^2}{\sigma_k^2} \ , \tag{5.1}$$

where k labels each point, n is the total points number and i labels the parameters to distinguish them each other.

The fitting procedure consists on finding a set of parameters $\{P_i\}$ that minimizes the value of the χ^2 function. The result of this procedure for each parameter is given by the parameter value accompanied by its own error $(P_i \pm \sigma_i)$ and by the χ^2 value that provides the quality of the agreement between the experimental points and the hypothesis.

5.3 The Bayesian method

Bayesian inference is a statistical inference approach in which probabilities are not interpreted as frequencies, proportions or analogous concepts, but rather as levels of confidence in the occurrence of a given event.

Unlike frequentist approach, where assumptions are somehow hidden, in the Bayesian method these are made explicit assigning to them a probability distribution (prior) and mixing with the information derived from experimental data, thus contributing to the final result (posterior).

Bayesian inference associates to the parameters fitted a probability distribution (prior) that must be known. This initial information given by the prior is subsequently

modified by the data and provides the posterior which is nothing more than a new probability distribution for the magnitude under examination. Therefore a Bayesian fit provides the probability distributions of the parameters, which indicate the probability that the parameter assumes within a confidence interval.

The method is based on the *Bayes theorem* [112], and it has the aim of finding the probability that a hypothesis is true given some experimental evidence. Bayes theorem can be written:

$$P(H_k|D_k) = \frac{P(D_k|H_k)\ P(H_k)}{P(D_k)}\ , \tag{5.2}$$

in which the probability $P(H_k|D_k)$ that the hypothesis describes the data is the *posterior* and the probability that data are described by the hypothesis $P(D_k|H_k)$ is called *likelihood*. $P(H_k)$ and $P(D_k)$ are, respectively, the knowledge expressed as probability density function we have about the hypothesis (*prior*), and a factor for normalizing the integrated posterior probability to unity.

Considering a mathematical model constituted by several parameters and a set of data D_k, the aim of the fit procedure is to determine the value of the parameters that best fit the mathematical model to the experimental data. Assuming the maximum prior ignorance, *i.e.* a lack of knowledge of the probability distribution of the measured quantities, Bayes theorem assumes a simpler form:

$$P(H_k|D_k) \propto P(D_k|H_k) \equiv \mathscr{L}\ . \tag{5.3}$$

In eq. (5.3), $\mathscr{L}$ indicates the likelihood, that is the probability of obtaining a specific set of points given a hypothesis considered true.

In a counting experiment, the probability that a single data $D_{k=i}$ is described by the hypothesis follows the Poisson distribution. However, one have to consider that increasing significantly the number of counts, such a distribution can be approximated with a Gaussian distribution. Thus for a single experimental point ($k = i$ with $i = 1, \ldots, n$) one gets:

$$P(H_{k=i}|D_{k=i}) = \frac{H_k^{D_k} \cdot e^{-H_k}}{D_k!} \approx \frac{1}{\sqrt{2\pi\sigma_k^2}} \exp\left[-\frac{1}{2}\left(\frac{H_k - D_k}{\sigma_k}\right)^2 \right]\ . \tag{5.4}$$

where $\sigma_k = \sqrt{D_k}$. The likelihood for a full set of data can be therefore written as:

$$\begin{aligned}
\mathscr{L} &= \prod_{k=1}^{n} \left[-\frac{1}{\sqrt{2\pi\sigma_k^2}} \exp\left[-\frac{1}{2}\left(\frac{H_k - D_k}{\sigma_k}\right)^2 \right] \right] \\
&= \left[\prod_{k=1}^{n} -\frac{1}{\sqrt{2\pi\sigma_k^2}} \right] \exp\left[-\frac{1}{2} \underbrace{\sum_{k=1}^{n} \left(\frac{H_k - D_k}{\sigma_k}\right)^2}_{\chi^2 \text{definition}} \right] \\
&\propto \exp\left(-\frac{\chi^2}{2} \right) . \qquad (5.5)
\end{aligned}$$

As one can see from eq. (5.5), the χ^2 function is closely linked to the likelihood ($\chi^2 \propto -2\ln\mathscr{L}$). Minimize the χ^2 is equivalent to maximize the likelihood $\mathscr{L}$. So the χ^2 gives a measure of the probability that the data are described by the model if data points follow a normal distribution. In the case in which the points follow a Poisson distribution, the likelihood assumes other forms [113].

Even though the method is general, in this thesis will be treated the case of measured data following a Gaussian distribution.

5.3.1 Markov chain Monte Carlo method

A stochastic markovian process or Markov process is a stochastic process in which the transition probability that determines the transition to a state of the system depends only on the previous state of the system and not by how it has come to such state.
The Monte Carlo methods based on Markov Chain (MCMC) are a class of algorithms for sampling from probability distributions based on the construction of a Markov chain having as equilibrium distribution (or stationary distribution) the desired distribution. The state of the chain after a large number of steps is then used as a sample of the desired distribution.

The exploration of the χ^2 hypersurface allows to get a set of parameters that can fit with the experimental data. Understanding χ^2 in a probabilistic way permits to define a unique method for the fitting procedure. The method is based in the Metropolis algorithm [114], properly modified in order to have a regulation system of the parameter changes, modification that is essential for finding the global minimum of $\chi^2\{P_i\}$ hypersurface. Starting from stochastic values of a set of hypothesis parameters P_{old}, the algorithm allows to generate a new set of parameters values P_{new} by changing randomly

one of them:

$$P^i_{new} = P^i_{old} + R \cdot P^i_{jump} \ , \tag{5.6}$$

where the parameter P^i_{jump} is linked with the parameter change and expresses the maximum change allowed for the parameter and R is a gaussian random number, generated from a distribution centered at 0 and with a unity standard deviation. New parameter sets is automatically accepted if χ^2 is lowered, but they are also accepted with a given probability if they increase the χ^2 value. The main consequence of this feature is that the algorithm can travel uphill along the hypersurface χ^2 in order to overcome small barriers. The probability of accepting a new set of parameters, given a particular set of old parameters, is the quotient of the likelihoods, and can be written as:

$$P = \frac{\mathscr{L}_{new}}{\mathscr{L}_{old}} = \frac{P(H_k\{P^i_{new}\}|D_k)}{P(H_k\{P^i_{old}\}|D_k)} = \frac{e^{-\chi^2_{new}/2}}{e^{-\chi^2_{old}/2}} = \exp\left[-\frac{1}{2}(\chi^2_{new} - \chi^2_{old})\right] . \tag{5.7}$$

Using the classical way of fitting the initialization of parameters is a crucial step for the convergence of the algorithm. Tuning the parameter jump P^i_{jump}, it is possible to adapt the sampling to the fitting parameter. Then, it is the jump parameter that decides the success of the fitting process and therefore the efficiency in finding the global minimum in the $\chi^2\{P_i\}$ hypersurface. If the jump is too small, there is the possibility of getting lost in no relevant details of the $\chi^2\{P_i\}$ landscape and the algorithm will always accept any change of the parameter, on the other hand, if the jump parameter is chosen to be too large, the parameters will hardly be accepted and the algorithm might get stuck. Before the algorithm starts the iteration, an assumption has to be made for the jump parameter P^i_{jump}, although this choice is not relevant since, for appropriate values, the algorithm converges quickly. One should note that after a number of iterations N carried out with this parameter jump, the acceptance ratio R^i_{real} of each parameter is evaluated and is performed a comparison with the desired one R^i_{des}. The maximum jump parameter is then changed according to the law:

$$\left(P^i_{jump}\right)_{new} = \left(P^i_{jump}\right)_{old} \cdot \frac{R^i_{real}}{R^i_{des}} = \left(P^i_{jump}\right)_{old} \cdot \frac{K_i/N}{R^i_{des}} \ , \tag{5.8}$$

in which K_i is the number of jumps accepted for the parameter i. If $R^i_{real}/R^i_{des} = 1$ the jump parameter is not changed.

This equation increases the jump of the parameters often accepted and decreases the jump of parameters which are rarely accepted, by setting different sizes of jump for

each parameter. This results in an efficient exploration of the parameters space in all directions.

Finally, we need a criterion that will tell us when the fit has reached the convergence. This is given by:

$$\frac{\chi^2_{old} - \chi^2_{new}}{\chi^2_{old}} < CC \ , \tag{5.9}$$

which says that the parameter i has converged when after a step in the algorithm, its change leads to a relative decrease of the χ^2 to below a certain value (CC = convergence criterion).

5.4 FABADA

FABADA (**F**itting **A**lgorithm for **B**ayesian **A**nalysis of **DA**ta) is a software that permits to perform Bayesian Data Analysis in a simple way [115]. The program is written in Fortran77, is an open code [116] and works for Windows and Linux operative systems. The graphics are generated from a data file, and then displayed using Gnuplot (not integrated). Recently FABADA has been implemented in the Mantid Project [56] that provides a support for computing and visualization of experimental data. At present Mantid is used at ISIS, SNS and HFIR, but other, such as PSI and ILL have joined lately.

The software is based on the MCMC method and Bayesian approach described in Section 5.3 [116]. The algorithm generate at every step a new set of parameters, that will be accepted or refused depending on its consistency with the experimental data and its error. It can be divided in two parts: the fitting procedure and the MCMC chain generation (Figure 5.1).

The first one leads the parameter to converge. In such process the parameters that better fit the data (parameters that minimize χ^2 or maximize the likelihood $\mathscr{L}$) are always accepted, but also parameters that leads to an increase of χ^2, but are compatibles with experimental error, are accepted. As already said, FABADA is able to move in any directions of the χ^2 hypersurface, avoiding that the program gets stuck in local minima. The MCMC chain generation permits to obtain the probability distribution functions related to the parameters and to the χ^2, leading to deeper analysis based on solid statistical background (Figure 5.2).

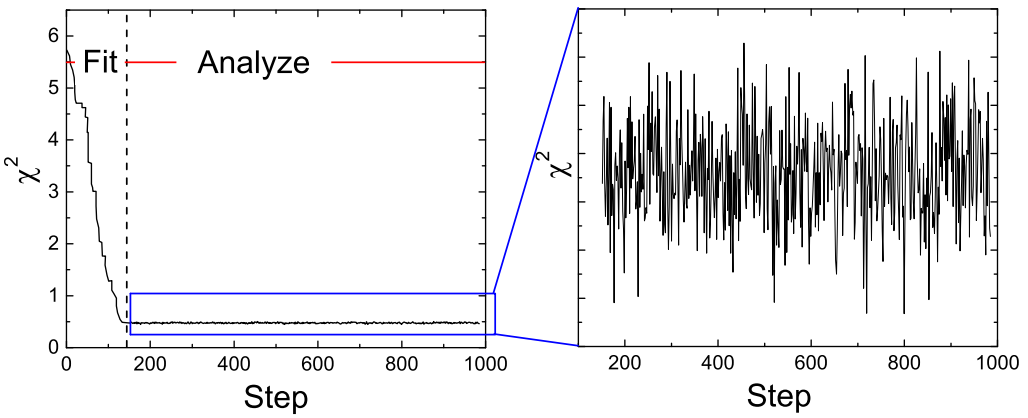

Figure 5.1: χ^2 plot as a function of the steps during FABADA process. It is possible to distinguish the fitting part in which all the parameters reach to convergence and the analyzing part that leads to the MCMC chain generation. In the right part an enlargement of the analyze part [117].

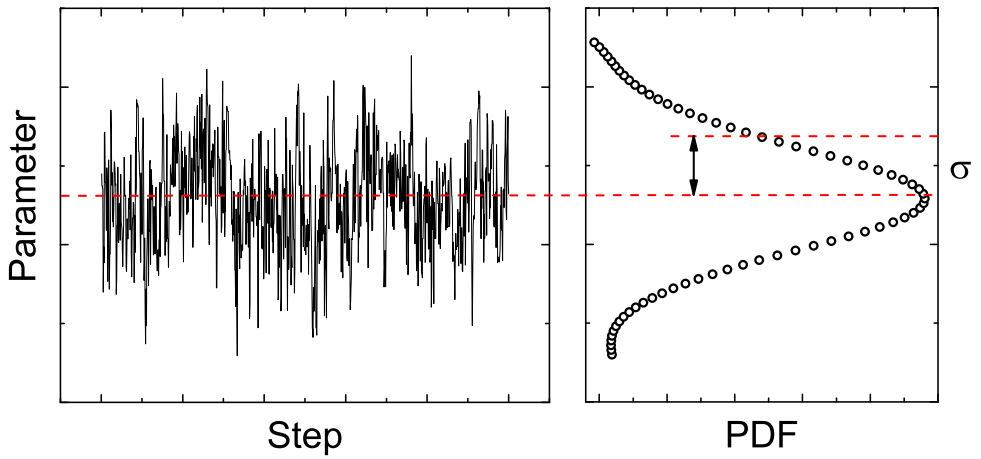

Figure 5.2: Example of MCMC chain for any parameter. The MCMC chain allows to describe the parameter using the probability distribution function (PDF) as shown in the right panel.

Using eq. (5.6) FABADA, after the parameters have reached the convergence, continues working (see Figure 5.1) to generate the MCMC chain. In order to prevent the correlation between two successive sets of parameters and to decrease the quantity of data it is possible to choose a saving rate that permits to save the parameters after a certain number of steps.
It is also possible to obtain an explicit representation of the correlation between the parameters plotting their chains as dependent on each other.

5.5 Model Selection

Generally it is always possible to analyze the experimental data using more than one interpretation. Inevitably this leads to consider several models that describe different physical mechanisms for the explanation of the results. It is therefore necessary to be able to choose between different models looking for a method to quantify the goodness of the chosen model.

Usually the criterion that is used for the selection of the model is based on the concept of "better fit", considering as "better fit" the one that leads to a lower value of χ^2 cost function, without adding any further explanation on the choice of a model over another. This assumption is valid only in case the under consideration models have the same number of parameters and these are completely uncorrelated. This means that in general it will be easier to get the best fit by increasing the number of parameters that describe any model. To avoid this problem, in the frequentist approach the reduced χ^2 is used to take into account the number of parameters. It is defined as:

$$\chi^2_{red} = \frac{\chi^2}{n - m - 1} \ , \tag{5.10}$$

in which n is the number od experimental points, m the parameters number and $n-m-1$ the number of degrees of freedom. So, if two models have the same value of the χ^2, the model with fewer parameters, *i.e.* the one that has the lowest value of the χ^2_{red} will be favored. This is nothing more than a manner of enunciating the Ockham's razor principle, which says that among competing hypotheses, the one with the fewest assumptions should be selected.

Model selection performed with the frequentist approach needs a number of assumptions with respect the χ^2_{red} space: there is a single minimum that has a square

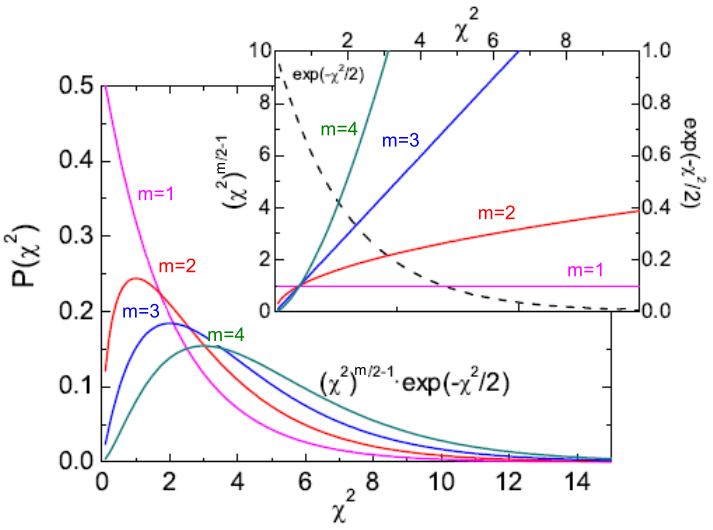

Figure 5.3: χ^2 distribution for a different number of fitting parameters m. The inset shows the terms associated with the goodness of the fit $\exp(-\chi^2/2)$ together with the one depending on the number of parameters m of the model $(\chi^2)^{m/2-1}$ [118].

dependence with all parameters, and the parameters are considered uncorrelated. In such case the probability distribution function takes the form [112]:

$$P(\chi^2) \propto \left(\chi^2\right)^{m/2-1} \cdot \exp\left(-\frac{\chi^2}{2}\right), \tag{5.11}$$

where m is the number of the parameters that describe the chosen model. The term $\exp(-\chi^2/2)$ is independent from the number of parameters and it decreases with the goodness of the fits or with increasing values of the errors associated with the experimental points. The term $(\chi^2)^{m/2-1}$ increases with the parameters number. Eq. (5.11) is shown in Figure 5.3.

On the other hand using FABADA that is based on the Bayesian method, χ^2 PDF is directly found exploring the parameter space, without the assumptions that are necessary in the frequentist approach. One has to note that the PDF, in this case, will not be exactly in the form of eq. (5.11), even if it will be similar. One should also make attention on the fact that all the advantages deriving on the use of the Bayesian approach could be lost if one considers only the minimum value of the χ^2 probability distribution. As shown in Figure 5.4, it is possible that a model presents a set of parameters that lead to a smallest value of χ^2 with respect to another model. However, considering all the

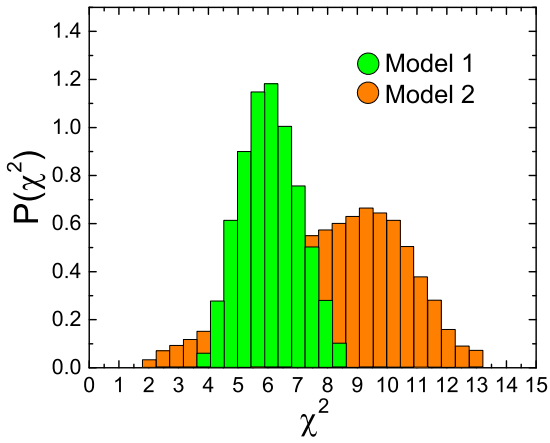

Figure 5.4: Probability distribution functions for two models. Model 2 presents the smallest χ^2 values, but the most probable values of model 1 are smaller (the peak of the distribution is at smaller χ^2 values) than probable values of model 2. With the frequentist approach one could wrongly choose model 2 as favorite model.

information contained in the probability distribution functions, the model that shows the peak of the χ^2 distribution at lowest values will be favored.

Therefore Bayesian model selection is a very powerful tool especially in the presence of complex models, in fact, using the PDF obtained by FABADA, the algorithm allows to get conclusions about models without the disadvantage of any frequentist supposition..

5.5.1 Example: How many lines are there?

Let us show the capacity of the Bayesian algorithm FABADA through an example that highlights the potentiality of this software [119]. The problem is to determine the number of processes that describe a given set of data.

The quasielastic (QENS) scattering spectra are generally quite complicated, this complexity derives from the fact that the number of processes remain unknown and that all of them are centered in the elastic response of the sample. The problem becomes more complex when the characteristics time scales of the various processes are comparable and therefore a selection based on the "better fit" visual check criteria is not sufficient. To solve such a problem and demonstrate the validity of the used method, a set of QENS data was generated as a sum of three Lorentzian processes and then convoluted

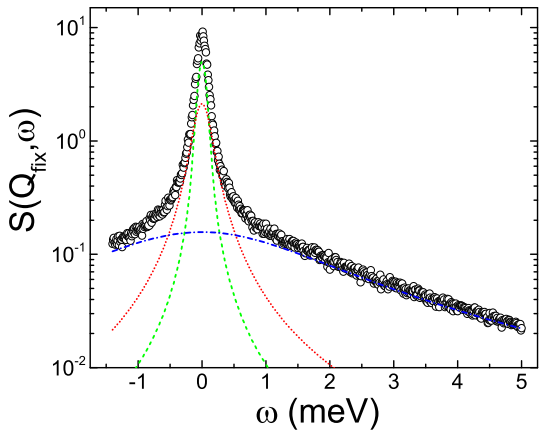

Figure 5.5: Synthetic QENS data. In Figure are shown the generated data with the associated errors (black circles) and the three components composing used. Lorentzians for data generation with three different FWHM values, 0.04 (dashed green line), 0.4 (dotted red line) and 2 meV (dash-dotted blue line) are shown [119].

with a gaussian resolution function with a FWHM of 0.01 meV. It was then carried out a model selection getting the χ^2 probability distribution functions in order to check whether the results are consistent with the already known information. Lorentzians for the generation of synthetic QENS data have been taken with three different FWHM values, respectively, 0.04, 0.4 and 2 meV, with the same amplitude ($A = 1$) and centered in $\omega = 0$. To make the data more realistic, after the convolution, a Gaussian-distribute relative error of 6% has been applied to the data (Figure 5.5).

The model selection was made considering 5 models, each with an increasing number of Lorentzian (from 1 to 5).

$$L_n = \sum_{i=1}^{n} L_i(\Gamma_i) \qquad \text{with} \qquad n = 1, \ldots, 5 \; . \tag{5.12}$$

All fit were performed under the same conditions. From the Figure 5.6 it is possible to see how the model with a single Lorentzian (L_1) does not describe well the data and can therefore be discarded. The same could be said for the model with two Lorentzian (L_2) looking in detail the peak, but we can not make assumptions about what concerns L_3, L_4 and L_5 which appear to be equally in accordance with the data. For this reason it is necessary deeper analysis using the probability functions (PDF) relating to the χ^2

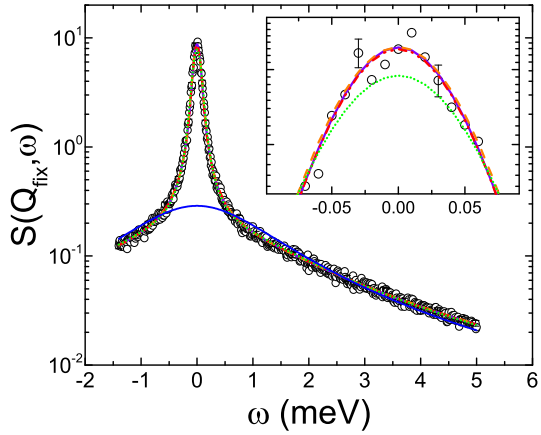

Figure 5.6: Fits to generated data with five different models composed by an increasing number of Lorentzians modes: L_1 (solid blue line), L_2 (dotted green line), L_3 (dash-dotted red line), L_4 (dashed orange line) and L_5 (solid purple line). Note that is not possible to distinguish, between L_3, L_4 and L_5 which the model that better describes the data [119].

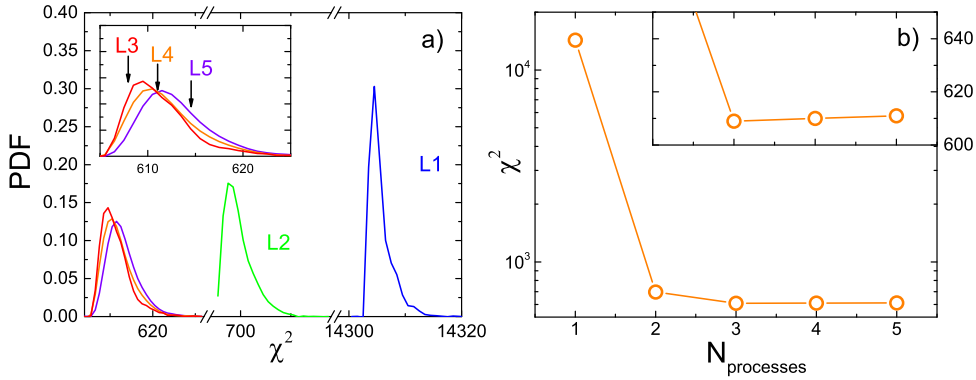

Figure 5.7: (a) Probability distribution functions relative to χ^2. In the inset an enlargement of L_3-L_5 PDF. The analysis of the spectra based on PDFs shows that L_3 is the best model to describe experimental data. (b) Values of the χ^2 PDFs relative to the peak of each distribution. In the inset it is evident that the addition of parameters does not lead to better fits [119].

cost function.

By analyzing the probability distribution function (Figure 5.7), L_3, L_4 and L_5 share the same area. We may note, however, as the peak position moves to the χ^2 values higher by increasing the parameters of the models used (from L_3 to L_5). So the addition of parameters over L_3 is not justified by the experimental data. We must also focus attention on the fact that L_2 PDF does not overlap with L_3 PDF, this indicates that there is no combination of two Lorentzian that gives a better fit than that obtained with three Lorentzian.

This simple example shows the strength and robustness of fitting procedure and model selection performed with FABADA.

Part IV

Scientific cases

Chapter 6

Dynamics and structural changes in plastic 1-Chloroadamantane

6.1 Introduction

In recent years great effort has been done to investigate the properties of the glass forming liquids to detect dynamical changes. Nevertheless, most of the good glass materials that allow "easy" investigations are molecular liquid in which translational, orientational and internal degrees of freedom contributions are strongly mixed and hardly decoupled. These facts make very difficult to investigate the detection of such dynamic transitions.

To have a clear view of distinct processes at the molecular level we need model compounds that not present mode-mixed dynamic. In order to gain some insights about the role of disorder in the properties of matter, systems with a constrained disorder are very interesting since they represent a series of phases hierarchized by the level of degrees of disorder. In the case of plastic phases, they lack only of orientational order, since the molecular centers of mass are forming an ordered lattice. This fact makes these systems very interesting models for canonical liquids. Specifically, they are useful to investigate if disordered phases are described by a single parameter, like density, or if

another order parameter describing molecular local ordering is necessary, the so called two order parameter descriptions of liquids [120–126]. In this work, we are interested if the same happens within plastic phases, such as that of ClA.

The plastic phase formed by the quasi-globular molecules of ClA is especially interesting since a maximum in specific heat reveals a change of the degrees of freedom of molecular movement, *i.e.* there is a disorder-disorder transformation that occurs without a first-order phase transition. This system can thus give some hints about the properties of the elusive liquid-liquid phase transition. In this Chapter the microscopic mechanisms behind this plastic to plastic transition by the concurrent use of Diffraction and Quasielastic Neutron Scattering experiments will be presented: the first one allowed us to determine if there are any changes in the structure, and the second in the dynamics along the calorimetric anomaly. These experiments show that together with a decrease of the density there is an increase of the freedom of rotation in the same temperature region where the calorimetric anomaly happens.

6.2 Previous works

Calorimetric experiments performed by Kobashi *et al.* found an anomaly in the temperature region where the plastic phase is stable: a broad heat capacity hump at a temperature $T \approx 330$ K [8] is seen. Considering the size of the abnormal heat capacity and the strong cooperativity of the compound under study, this jump does not seem to be related to a Schottky anomaly, as confirmed by Kobashi *et al.*, but rather to a change in the orientational arrangement or/and in its dynamics. ClA, together with some other adamantane derivatives, has been object of several studies by means of broadband dielectric spectroscopy (BDS) [5, 127], nuclear magnetic resonance (NMR) [128, 129], differential thermal analysis (DTA) [130, 131], x-ray scattering [132–136], IR experiments [137], calorimetry [8], quasi-elastic neutron scattering (QENS) [6, 138] and molecular dynamic (MD) simulations [139, 140].

For what concerns the microscopic dynamics, the studies of Bée *et al.* [6], stated that the motion of ClA in the plastic phase cannot be explained by an isotropic rotation. They described the molecular motion through a model that describes the dynamic structure factor as the sum of uniaxial rotations plus rotations around the [111] lattice directions instead. They found that there was no correlation between these two motions,

being the combination of both movements compatible with an isotropic rotation only at high temperatures. Dielectric spectroscopy has also been performed to study the dynamics of this compound [5, 127] finding a good correlation with the times obtained with the previous work of Bée *et al.* using QENS. Also NMR was performed to investigate the changes in the dynamics from the ordered crystalline phase to the plastic phase [128, 129]. None of these works found an indication of a change in the dynamics at a temperature of 330 K. On the other hand, a change in the dynamics within the plastic phase has been detected by the concurrent use of Molecular Dynamics NMR and Raman scattering [139, 140] that was associated in that work to a "local orientational ordering".

6.3 Properties of Adamantane and its derivatives

These hydrocarbons are ringed compounds with a diamond-like structure formed by a series of six carbon rings fused together. Adamantane and its derivatives have shown many applications in medicine, such as drug delivery and targeting, DNA directed assembly, the formation of nanostructures DNA-amino acid, and were used as models for crystallization of catalysts and synthesis of high-temperature polymers. It is therefore great the interest in these compounds both in the field of fundamental research and in applied research. Besides the interest they arise, these organic structures can cause serious problems in the production of oil and gas. Therefore to reduce the problems due to the precipitation of diamondoids in the oil production process, the knowledge of the phase behavior of these compounds with hydrocarbons is very important [141].

Diamondoid molecules are cage-like and hydrocarbons. The first and simplest member of the diamondoids group, adamantane (see Figure 6.1a), is a tricyclic saturated hydrocarbon. In the solid state these compuonds melt at much higher temperatures than other hydrocarbon molecules with the same number of carbons in their structure. Since they also possess low strain energy, they are more stable and stiff, resembling diamond in a broad sense. Many of the diamondoids possess structures rich in tetrahedrally-coordinated carbon, and they have a very high strength-to-weight ratio.

ClA ($C_{10}H_{15}Cl$), showed in Figure 6.1b, is a rigid spherical-like molecule. It is obtained from the adamantane cage-like molecule ($C_{10}H_{16}$) substituting a methane hydrogen with a chlorine atom. When heating the low temperature solid crystalline phase,

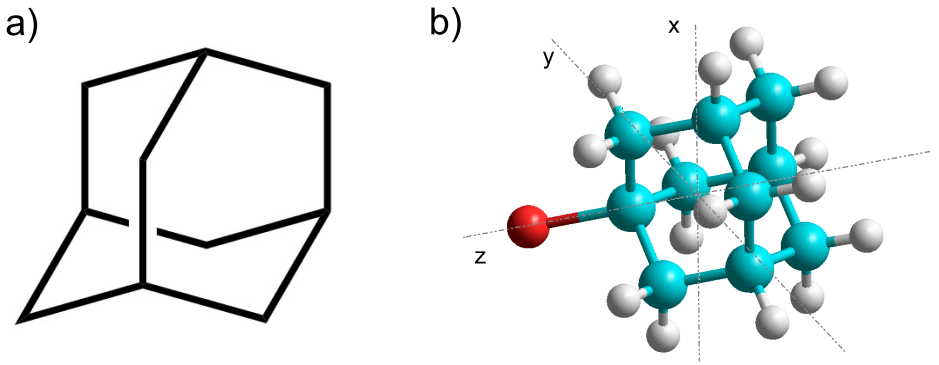

Figure 6.1: (a) Molecular structure of adamantane with chemical formulas $C_{10}H_{16}$. (b) $C_{10}H_{15}Cl$ molecular structure. Carbon atoms are in blue, hydrogens in white and chlorine atom in red. Dashed lines represent the molecular inertial axes. The z-axis is located in the bond direction between the chlorine atom and one of the carbons.

ClA displays a first solid-solid phase transition at 244 K, which on further heating transforms to the plastic phase (space group $Fm3m$) and a plastic-liquid transition at 442.5 K [136, 142]. The compound used for the experiments was purchased from Sigma Aldrich Chemical Co. with a purity grade of 98% and no further purification was performed. A deuterated sample was used in diffraction experiment, while a hydrogenated one for quasielastic measurements.

6.4 Experimental details

6.4.1 Neutron Diffraction

Diffraction measurements were performed using D1B diffractometer presented in Section 3.6.1 with a deuterated sample. The instrument is a two-axis spectrometer and the pyrolitic graphite monochromator provide a very high flux with a wavelength of $\lambda = 2.52$ Å focusing onto the sample [42]. Sample was held in a cylindrical aluminum cell with a thickness of 0.1 mm (Figure 6.3a). The temperature of the sample was controlled by a cryo-furnace and the measurements were performed between 220 K and 380 K using a scanning rate of 0.2 Kmin^{-1}. To take into account possible contamination a measurement of the empty container and of the empty instrument were performed to

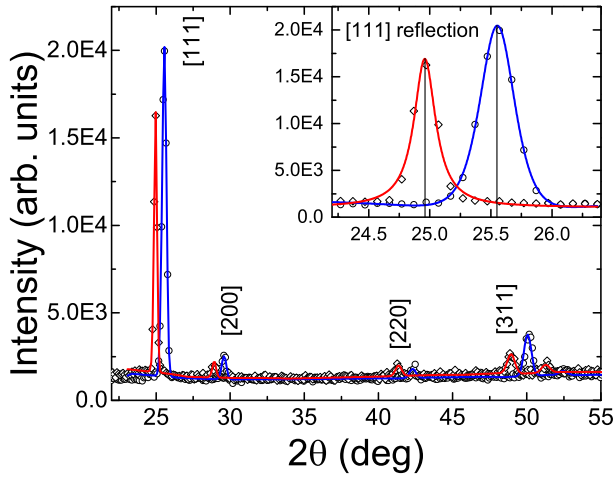

Figure 6.2: Two sets of ClA diffraction data at 260 K (open circles) and 360 K (open diamonds). Lines show the refinement pattern matching procedure performed with FullProf Suite, blue line for 260 K and red line for 360 K. In the inset an enlargement of the area relative to the peaks that correspond to [111] reflection.

subtract the spectra.

After correcting the data, as stated in Section 3.7, Bragg peaks have been indexed, their positions and subsequently the lattice parameters were refined and determined by the full pattern matching analysis of the neutron diffraction spectra by least-squares minimization. Figure 6.2 shows the refinement for two diffraction spectra of ClA.

6.4.2 QENS

Quasi-elastic neutron scattering (QENS) experiments were carried on IRIS time-of-flight spectrometer described in Section 3.3.1 with a hydrogenated sample. To minimize the effects of multiple scattering and achieving a transmission of $\approx 90\%$ a Chloroadamantane sample of 0.25 mm of thickness was kept in a flat aluminum container composed by two slabs with a thickness of 0.1 mm (Figure 6.3b). Sample holder was put in a closed-cycle cryostat at 45° respect the incident beam to collect data at $T = 260, 280, 300, 320, 340, 360$ K. The wavelength of incident neutrons used in the experiment was $\lambda = 2.52$ Å (12.88 meV) with an energy resolution of 17.5 µeV. The analyzer bank used the reflection [002] of pyrolitic graphite to record 51 neutron spectra

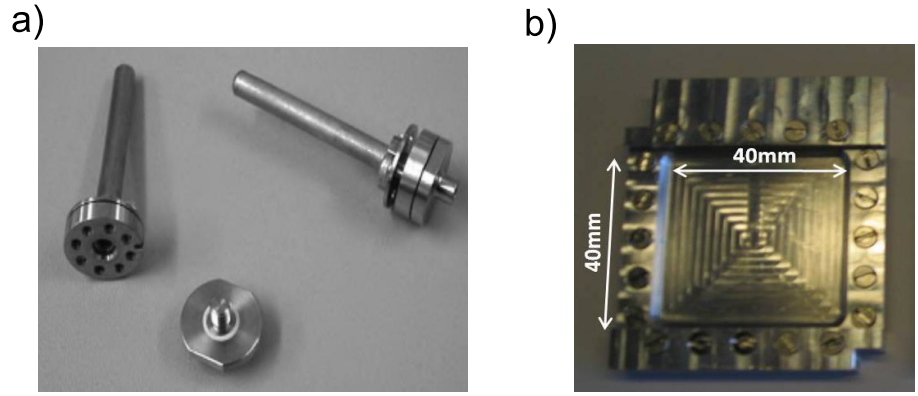

Figure 6.3: (a) Vanadium-aluminium cylindrical sample holders used in D1B. (b) Flat aluminum sample container used on IRIS.

simultaneously, corresponding to a scattering angle (2θ) range between $25° - 160°$ and then to a Q-range from 0.442 to 1.854 Å^{-1}. In energy, spectra were evaluated from -0.5 to 0.5 meV. Data reduction, including empty cell subtraction, calibration with a vanadium rod, and conversion into constant Q spectra, was performed with the program MANTID [56]. Calculating the momentum transfer Q from the scattering angle, spectra were then grouped together in bins of 0.1 Å^{-1}.

The structure factor maximum appears at ≈ 1.15 Å^{-1} [143], therefore, being interested in the study of the incoherent scattering related to the molecular dynamics, the spectra were analyzed in the Q-range $0.45 - 1.05$ Å^{-1}, where the coherent contribution can be neglected.

Analysis of QENS data has been performed using the software package FABADA (Section 5.4) [111,115,118,119,144,145]. Bayesian inference performed with this method is done in two parts. First of all the fitting leads to the set of parameters that better describes the data. To analyze the results, *i.e.* to obtain the PDFs associated with all parameters (that have into account their correlation) and to χ^2, in a second step the software generates a complete Markov chain. The adaptive algorithm and the Bayesian methodology has been described in Chapter 5 and in previous publications [111, 115, 118, 119, 144–148], and the readers are referred to them for technical details.

In order to avoid an over interpretation of QENS data on ClA we have first determined the optimal value of processes we can describe given the information content

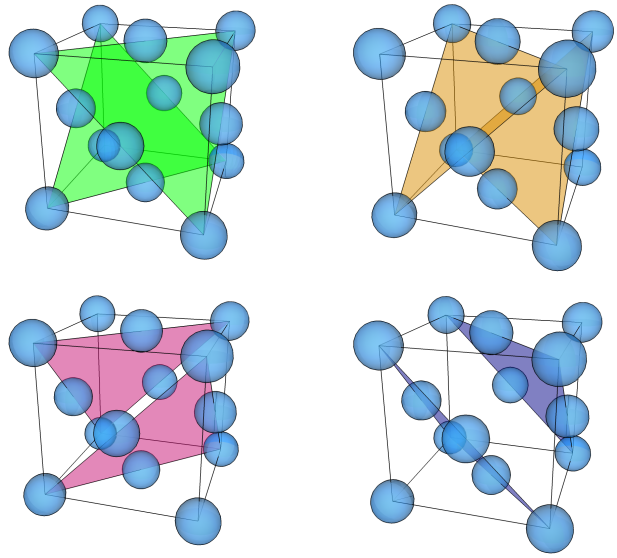

Figure 6.4: [111] reflection planes through a fcc Bravais lattice.

of data, basically determined by the errors and the limitation in energy and momentum transfer. To do that we have used a simple model consisting on a superposition of Lorentzian curves (L1, L2, L3). The scattering law $S(Q,\omega)$ can be then described as a function of momentum ($\hbar Q$) and energy ($\hbar\omega$) transfer by:

$$S(Q,\omega) = A_0\delta(\omega) + \sum_{i=1}^{n} A_i \frac{1}{\pi}\frac{\Gamma_i}{\omega^2+\Gamma_i^2} \ , \tag{6.1}$$

where Γ_i is the width of the i-th Lorentzian function and A_i are the weights for each Lorentzian.

The models containing physical information about the microscopic dynamics of ClA tested on the obtained data were two: an isotropic rotation and an anisotropic rotation (Section 3.5.3). The first model reads:

$$S_{inc}^{iso}(Q,\omega) = A_0\delta(\omega) + \sum_{l=1}^{\infty} A_l \frac{l(l+1)D_R}{(\omega)^2+[l(l+1)D_R]^2} \ , \tag{6.2}$$

with $A_l(Q) = (2l+1)j_l^2(Qr)$. D_R is the isotropic rotational diffusion and $j_l(Qr)$ the Bessel spherical functions. The isotropic rotational model has into account that there is not a preferred axis of rotation around any of the principal axis of the molecule. However, on regards the molecular shape it is more plausible that the rotation resembles that of

a symmetric top. For this reason we have taken an anisotropic model [7] adapting it to the description of QENS data, obtaining the following scattering law:

$$S_{inc}^{anis}(Q,\omega) = A_0\delta(\omega) + \sum_{l=1}^{\infty} A_l \cdot \sum_{m=-l}^{l} \frac{\Gamma_l^m}{\omega^2 + (\Gamma_l^m)^2} \ , \tag{6.3}$$

with $\Gamma_l^m = l(l+1)D_x + m^2(D_z - D_x)$. D_z is the uniaxial rotational coefficient along the molecular symmetry axis, and D_x is the rotation around the perpendicular axes (see Figure 6.1b). The use of this model is justified by the values obtained for the inertia momenta around each of the principal axes since $I_x \approx I_y$ ($I_z = 295\ a.u. \cdot \text{Å}^2$, $I_x = 591\ a.u. \cdot \text{Å}^2$ and $I_y = 589\ a.u. \cdot \text{Å}^2$). The scattering laws of these two models are calculated as a series of infinite terms. If expanded only up to the second term they read (the utility of that will be seen later on):

$$S_{inc}^{iso}(Q,\omega) = A_0\delta(\omega) + A_1 L(2D_R) + A_2 L(6D_R) \tag{6.4}$$

$$S_{inc}^{anis}(Q,\omega) = A_0\delta(\omega) + 2A_1 L(D_x + D_z) + A_2 L(2D_x). \tag{6.5}$$

It is important to note that the fits to these physically relevant models have been performed using the whole scattering law, *i.e.* a single function has been used to fit all Q-values, *i.e.* the fit has been performed using the complete two dimensional function $S_{inc}(Q,\omega)$. This point is very important since the obtained results are robust and so are the conclusions obtained from the fits, since more data is described with a minimum number of parameters.

6.5 Results

6.5.1 Structural change

The results obtained from the analysis of diffraction measurements show a step-like evolution of the peak position relative to the reflection [111] as shown in Figures 6.4 and 6.5b. The peak position moves to lower angles increasing the temperature and exhibits an abrupt change in its slope in the same temperature range where an anomalous heat-capacity hump, measured by Kobashi *et al.* [8] takes place. The lattice parameter obtained from the pattern-matching process previously described show also a step-like shape when increasing the temperature.

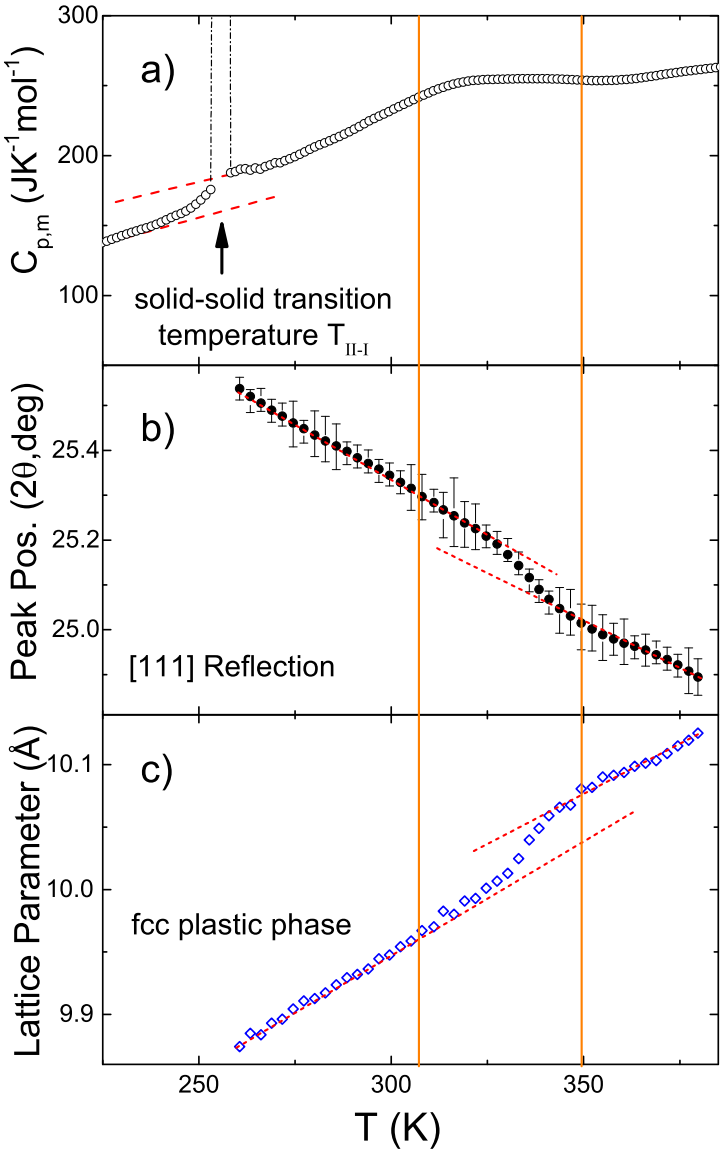

Figure 6.5: (a) Zoomed region making evident the heat-capacity anomaly. Digitize from [8]. (b) Peak position relative to the [111] reflection. Peak moves to lower angle increasing the temperature and shows an abrupt change in the same T-range where the anomalous heat-capacity hump takes place. (c) Lattice parameter of the cubic cell. It is evident a step-like behavior in the same range in which the calorimetric hump was seen.

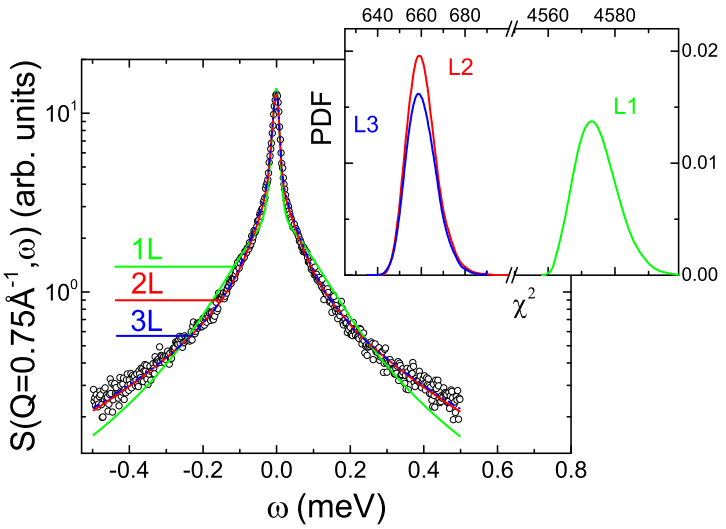

Figure 6.6: Data fits for 1−Chloroadamantane at $T = 340$ K and $Q = 0.75$ Å^{-1} using different models: one lorentzians (L1, green line), two lorentzians (L2, red line) and three lorentzians (L3, blue line). Using the same colors, the inset shows the corresponding χ^2 PDFs.

6.5.2 Dynamical scenarios

The first question to be answered about the obtained results of QENS is to know the maximum amount of processes that are justified to use to describe the data. In order to determine the optimal number of lorentzians that describe our data we have calculated the χ^2 PDFs for one, two and three lorentzians. To perform model selection we can find three scenarios:

- When two non-overlapping PDFs are found this means that the model with lower values of χ^2 is clearly preferred since any combination of parameters of the best model is able to describe better the data than with the competing model
- When the PDFs of two models overlap, the maximum of the χ^2 distribution should be chosen as a criterion to find the best model. However, in this case we should be aware that it is possible that any new piece of information or data can reverse the model selection
- If the two PDFs are so similar that no clear difference in minima is to be seen,

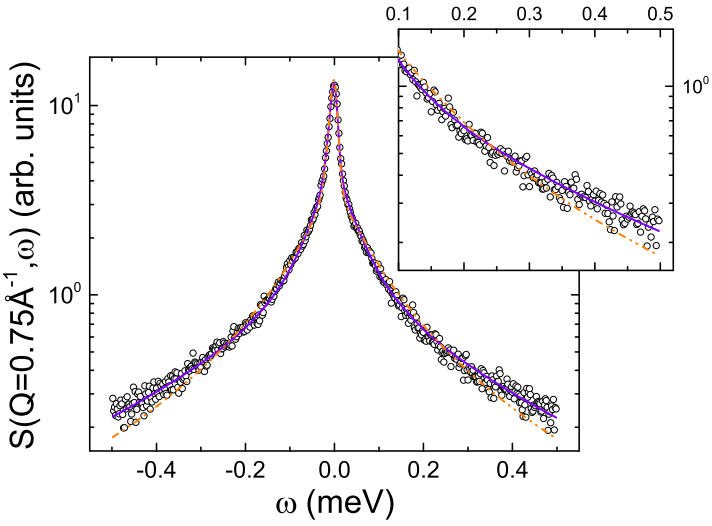

Figure 6.7: Anisotropic (purple line) *vs* Isotropic (dashed orange line) models for $C_{10}H_{15}Cl$ data set at $T = 340$ K and $Q = 0.75$ Å. The models are presented with two contributions (isotropic model has been truncated at $l = 2$. It is evident, even at first glance, that the anisotropic model better describes the data). In the inset an enlargement of the tail, confirming the better accordance of anisotropic model with respect the isotropic one.

following Occam's razor criterion, the model with less parameters should be chosen.

A first glance at Figure 6.6 makes evident that one peak is not able to correctly describe the data (both looking at the fit and the χ^2 PDF in the inset). The problem arises when determining if two or three lorentzians should be chosen to describe the data since they describe correctly the data and also have a similar PDF with maxima located at more or less the same position. We have chosen the model with only two lorentzians following the aforementioned criteria. In order to gain some insight about the microscopic mechanism that is ruling the dynamics of ClA in the plastic phase we have used two models to describe QENS data: an isotropic rotation and an anisotropic one. In Figure 6.7 we show the fits of both the isotropic and anisotropic models at a relatively high temperature. First of all we should point out that the values obtained for D_R (≈ 0.03 meV at $T = 340$ K) from the analysis of the isotropic model show agreement with the results

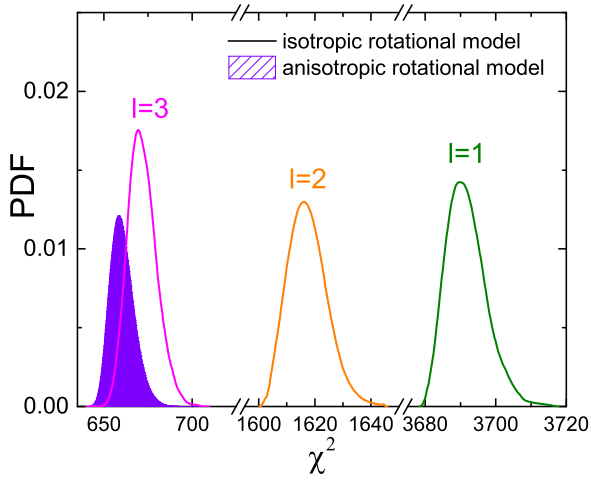

Figure 6.8: PDFs obtained from global fits over the entire scattering function. Solid area describes the anisotropic model while lines describe isotropic ones.

obtained in the previous work of Bée [6] (from 0.042 to 0.056 meV at $T = 353$ K). As it can be seen the anisotropic model is able to better describe the experimental data. We would like to point out that, although we show only one instance, the fit was performed using the whole scattering law. For this reason and also to be sure that the added complexity of the anisotropic model is justified we show in Figure 6.8 the χ^2 PDFs for the isotropic and anisotropic models. When truncated at the second term it is clear that the anisotropic model describes the data much better that in the isotropic one: there is not an overlap of the distributions. Even if expanded to three terms (Figure 6.8) the anisotropic model is a better option to describe the data. This model selection has been performed for all temperatures getting the same result, for this reason even at high temperatures the isotropic model is not able to describe the data correctly in comparison with the anisotropic model. Once the anisotropic model is established to describe better the data than an isotropic model for all the temperature range studied we can study the physical parameters obtained from that model. The rotational diffusion coefficients values D_x and D_z obtained by the anisotropic model differ about one order of magnitude (Figure 6.9), describing a rotational around z-axis much faster than around the perpendicular axes, as expected. Also as expected the difference between them decreases with an increase of the temperature, however

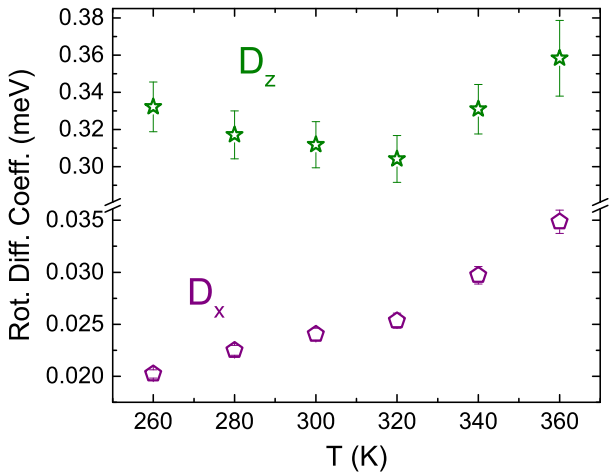

Figure 6.9: (color online) Rotational diffusion coefficients for all the measured temperatures. It is evident that rotational diffusion coefficients D_x and D_z obtained for the anisotropic model exhibit a kink at ≈ 320 K

even at the highest temperature they still differ about a decade. Rotation around the symmetry axis z (see Figure 6.1b) seems to have a small temperature dependence in the low temperature region, but at higher temperatures this behavior changes leading to an increase of the rotational diffusion coefficient D_z. This change in the behavior of the dynamics goes along with a change of slope of D_x as it is seen in Figure 6.9.

6.6 Discussion and conclusions

It is clear from Figures 6.5, where the evolution of the lattice parameter is shown, and from Figure 6.9, where the rotational coefficients are shown as a function of temperature, that there is a change in structure and dynamics where the calorimetric hump is seen.

Concerning the structure, the slope of the lattice parameter as a function of temperature both at high and low temperature seems to be similar, and therefore there is not a significant change in the expansivity of the material in these two regions. However there is a jump in the lattice parameter at about 330 K. Therefore it seems that the degrees of freedom increase in these region causing both the jump in density and in specific heat.

Figure 6.9 shows the change in the dynamics of the rotation of the molecule around

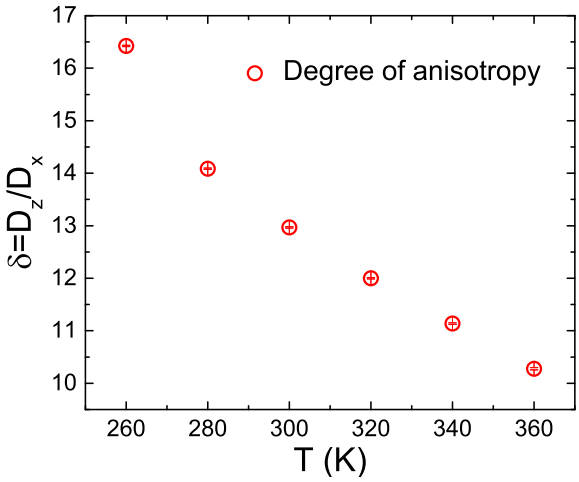

Figure 6.10: Degree of anisotropy $\delta = D_z/D_x$. This quantity tells us how far the ClA molecule is from free rotation around its principal axes.

its symmetry axis z, and the rotation associated with the jumps between equivalent orientations of the molecule in the lattice. Taking into account the momentum of inertia of the molecule, we can calculate the value that should be obtained for the ratio D_z/D_x if this molecule was performing a free rotation around each of its principal axes: $D_z/D_x = \sqrt{I_x/I_z}$. This calculation leads, for ClA a value of $D_z/D_x = 1.4$. In order to figure out how far away for free rotation around its principal axes the molecule of ClA is, we show in Figure 6.10 the value for D_z/D_x in all the temperature range getting values much bigger than those expected from molecular geometry. It is clear thus that the dynamics of the molecule is affected by its structure. Indeed together with the jump in density there are changes both in the uniaxial rotation around z-axis and in the crystal reorientations quantified by D_x and D_z: there is an increase of the slope as function of temperature, and thus an increase of mobility.

The changes in the structure of the plastic phase of ClA go along with changes of the dynamics associated both with the uniaxial molecular rotation and with that of the molecular reorientations. Three main conclusions can be obtained from the results of our work. First of all, that there is a clear interplay between structure and dynamics associated with the calorimetric effect detected by Kobashi *et al.* [8]. The second conclusion is that, contrary to the findings of Bée *et al.* [6], it seems to be a correlation

between uniaxial rotation and reorientation motions. Finally, our results indicate that within a disordered phases there might be changes associated with the structure and dynamics that must be described by the addition of a second parameter to describe them. Our results thus support a two order parameter theory of disordered phases.

Chapter 7

The most fragile plastic crystal: Freon113

7.1 Introduction

In plastic phases molecules rotate in a more or less free way, being their centres of mass ordered in a crystalline structure. As it happens with canonical glasses, it is possible to freeze the rotation of the molecules by lowering the temperature at a fast enough pace. Because only a degree of freedom is frozen, plastic phases are simpler to study with respect canonical glasses.

Freon113 provides a well-known example of compound exhibiting plastic crystal phases [145, 149–153]. This simple molecule displays internal molecular degrees of freedom which promote the appearance of distinct conformers (trans and gauche (Figure 7.1)), with low frequency internal modes that are able to couple with lattice motions, giving rise to a complex energy map [145, 149].

Moreover, because of these degrees of freedom, nucleation of the ordered phases is hindered, and the high-temperature disordered (plastic) phase is easily supercooled. The easiness to arrest these orientationally-disordered phases has indeed been linked to the existence of internal molecular degrees of freedom for a similar compound, Freon112 (1,1,2,2-tetrachloro-1,2-difluoroethane, $CCl_2F{-}CCl_2F$). Interestingly, for Freon112 the value for the fragility was reported to be the highest for a plastic crystal ($m = 68$) [154].

In addition, a previous study on thermal conductivities of Freon112 and Freon113 compounds [152] shows that quasilocalized low-energy vibrational modes emerge at very low energy, lower than the values of the maximum of the boson peak, when compared to other OG. These low-energy modes in glassy systems promote additional scattering that leads to a decrease of the mean free path of vibrations and then to an increase of the vibrational density of states $g(\omega)$ and, consequently, of the heat capacity excess ($C_{p,exc}$) over the classical Debye behavior $C_D \propto T^3$.

Interestingly, some authors [155] proposed a correlation between the $(C_{p,exc})_{max}/C_D$ ratio, $(C_{p,exc})_{max}$ being the maximum of the excess specific heat, and the fragility for glass-forming systems. They seem to have a linear correlation, the higher the fragility index, the smaller the ratio.

In this Chapter a dynamic and thermodynamic study of the orientational glass former Freon113 will be presented, in order to analyze its kinetic and thermodynamic fragilities. Its orientational dynamics studied by means of dielectric spectroscopy together with the microscopic origin of its specific heat and the vibrational density of states determined by inelastic neutron scattering have revealed the highest fragility value, both thermodynamic and kinetic, found for this orientational glass former.

The excess in both Debye-reduced specific heat and density of states (boson peak) evidences the existence of glassy low-energy excitations. We demonstrate that the proposed correlations between the boson peak and the Debye specific heat value are elusive as revealed by the clear counterexample of the studied case.

7.2 Previous studies

Plastic crystals show typically low kinetic fragility, as cyclooctanol ($m = 33$) [156, 157], cycloheptanol ($m = 22$) [158], ortho-carborane ($m = 20$) [159], cyano-adamantane ($m = 17$) [5, 160], adamantanone ($m \approx 16$) [5, 161], ethanol ($m = 48$) [5], or mixed molecular crystals $NPA_{0.7}NPG_{0.3}$ ($m = 30$) [162–164]. The most fragile OG known to date are the Freon112 ($CCl_2F - CCl_2F$) with $m = 68$ [154] and a solid-solution of succinonitrile (60%) and glutaronitrile (40%) with $m = 62$.

In the investigation for understanding the glass transition, many attempts to connect the kinetic fragility associated with the relaxation time behavior as a function of temperature, with the thermodynamic behavior have been reported [22, 23, 26, 165–168]. In

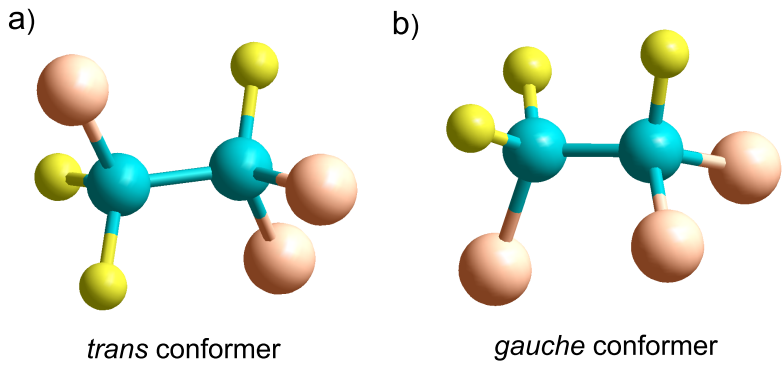

Figure 7.1: 3D diagram two geometrical conformations of Freon113. Carbons are in blue, fluorine atoms in yellow and chlorine in orange. The two structural conformations are linked to each other by a rotation of about 120 ° around the $C-C$ bond. The conformers that exhibit a *trans* position of two $C-Cl$ and $C-F$ bonds have a C_1 symmetry, whereas the ones that show a *gauche* position of all the $C-Cl$ and $C-F$ bonds, have a C_s symmetry.

his studies on glass-forming systems, Angell [165] showed that more fragile liquids (and also plastic crystals) exhibited larger and sharper jumps in their relative specific heat curves at the glass transition, associated with larger configurational excess entropies. The only exception was found for some alcohols, which although having intermediate fragilities presented larger heat-capacity changes than for the fragile liquids, a fact which was attributed to the peculiarities of hydrogen bonding.

To quantify such correlation, *kinetic fragility* $F_{1/2}$, defined in eq. (2.15), is compared to the thermodynamic fragility $F_{3/4}$ defined in eq. (2.16).

Furthermore, a more extensive compilation of data for small organic molecule, polymeric, and inorganic glass-forming liquids by Huang and McKenna [166] revealed many deviations from the earlier claimed correlation between kinetic and thermodynamic fragilities. Specifically, they compare the kinetic fragility index m (eq. 2.3) with the ratio of the liquid to the glass specific heats at T_g, $C_{p,liq}/C_{p,gl}$, as a measure of thermodynamic fragility. Although they confirmed the positive correlation between m and $C_{p,liq}/C_{p,gl}$ for inorganic glass formers, the opposite correlation was observed for polymeric glass formers, whereas m was found to be nearly constant and independent of

$C_{p,liq}/C_{p,gl}$ for small organic and hydrogen-bonding molecules.

7.3 Freons

Chlorofluorocarbons (CFC) are organic compounds that typically contain carbon, chlorine, and fluorine atoms. Freon is a trade name, often used to refer to CFCs, which have been used in a wide range of applications. They are produced as a volatile derivative of methane, ethane, and propane. CFCs are highly effective refrigerants that were developed in response to the pressing need to eliminate toxic and flammable substances, such as sulfur dioxide and ammonia, in refrigeration units and air conditioners. Used also as aerosol propellants, solvents, cleansing agents for electrical and electronic components and foaming agents in shipping-plastics manufacturing they are odorless, colorless, nontoxic, and nonflammable.

Freon113 or CFC-113 is a chlorofluorocarbon and belongs to the halogen-ethane series ($C_2X_{6-n}Y_n$, with X, Y= H, Cl, F, Br). Its formula is: $Cl_2FC - CClF_2$. Such a molecule has gained great interest for its role in the depletion of stratospheric ozone. CFC-113 is very unreactive and remains in the atmosphere about 90 years, sufficiently long that it will cycle out of the troposphere and into the stratosphere, where it can be broken up by ultraviolet radiation ($190 - 225$ nm, UV-range), generating chlorine radicals ($Cl\cdot$), which start the degradation of ozone.

Freon113 used in our experiments has been purchased from Aldrich Chemical Company with a purity of 99%. It is liquid at room temperature and presents a melting point at $T = 238$ K and a boiling point at $T = 320$ K.

7.4 Experimental details

The broadband dielectric spectroscopy measurements were performed using a Novocontrol Alpha-analyzer (10^{-2} to 10^7 Hz) equipped with a Quatro temperature controller (± 0.1 K) working down to 100 K and a closed-cycle helium cryostat for lower temperatures (see Section 4.3). The prepared sample were located into a parallel-plate stainless steel capacitor with the electrodes separated by 50 µm-thick silica spacers (Figure 7.2). The volume of the sample is determined using glass fibers spacers (50 µm or 100 µm are available) in such a way that there is no contact between the capacitor faces.

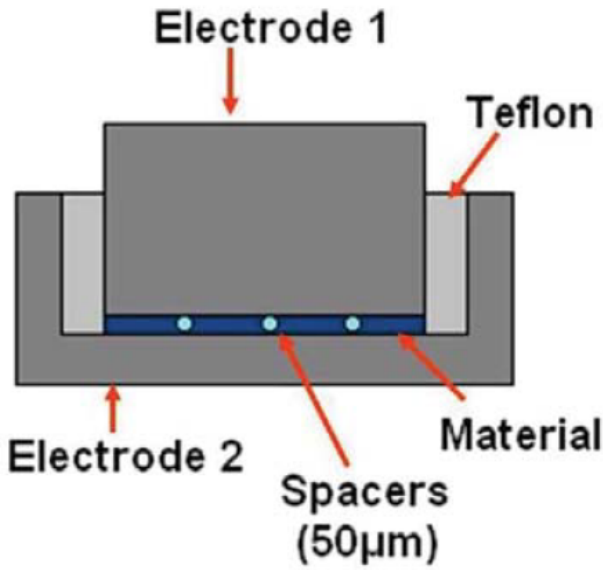

Figure 7.2: Diagram of the sample cell with the features used in the experiments.

Spectra were taken in the temperature ranges between 118 K and 94 K every 4 K and between 90 K and 70 K every 2 K with the helium cryostat and the Alpha analyzer. Broadband dielectric spectroscopy spectra have been fitted by means of FABADA software (Section 5.4). Figure 7.3 shows imaginary part of the dielectric permittivity at $T = 88$ K. Dielectric loss spectra were fitted according to a superposition of one Havriliak-Negami and two Cole-Cole functions, giving the relaxation time of the different dynamic processes. Then, the fitting function is given by:

$$\begin{aligned} \varepsilon^*(\omega) - \varepsilon_\infty &= d_{CC1}\left(\frac{\Delta\varepsilon_{CC1}}{1+(i\omega\tau_{CC1})^{\alpha_{CC1}}}\right) + d_{CC2}\left(\frac{\Delta\varepsilon_{CC2}}{1+(i\omega\tau_{CC2})^{\alpha_{CC2}}}\right) \\ &+ d_{HN}\left(\frac{\Delta\varepsilon_{HN}}{[1+(i\omega\tau_{HN})^{\alpha_{HN}}]^{\beta_{HN}}}\right), \end{aligned} \tag{7.1}$$

where τ_{CC1}, τ_{CC2} and τ_{HN} are the relaxation times for the different dynamical motions.

In order to quantify the thermodynamic fragility of Freon113, we have obtained the corresponding entropy curves for the OG/plastic crystal (crystal I) phases from specific-heat measurements performed by means of adiabatic calorimetry.

The boson peak that dominates the low-frequency vibrational spectrum of glasses has been measured by both inelastic neutron scattering and specific heat. Inelastic

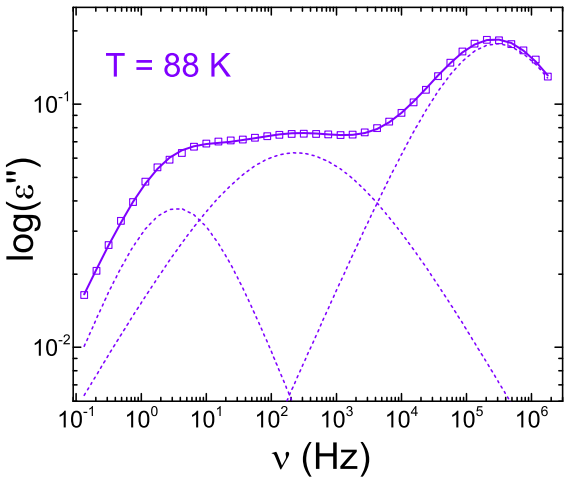

Figure 7.3: Solid line is an example of the fits using Havriliak-Negami and Cole-Cole fitting functions. Dashed lines show the contributions of the main α-relaxation and the slower processes for the spectrum at 88 K.

neutron scattering data were acquired using the chopper spectrometer MARI at ISIS neutron facility in Oxford, UK.

7.5 Results

7.5.1 Dynamical processes and kinetic fragility determination

The dielectric loss spectra were fitted according to eq. 7.1 with a β_{KWW} exponent. Fittings to the imaginary part of the dielectric permittivity are shown in Figure 7.4a. The main non-Arrhenius α-relaxation process is accompanied by two slower processes associated with internal degrees of freedom (Figure 7.5). They show an Arrhenius behavior with a very similar energy barrier (see Figure 7.5). We can tentatively relate this behavior to the jumps between trans and gauche configurations, being the difference in time due to a different dynamics caused by different molecular surroundings. In order to confirm such hypothesis, molecular dynamic simulation with a variable energy barrier between configuration would be needed.

The β_{KWW} exponent was calculated according to the Alvarez-Alegria-Colmenero equation ($\beta_{KWW} = (\alpha\beta)^{1/1.23}$) [93], and the so-obtained values were ranged between

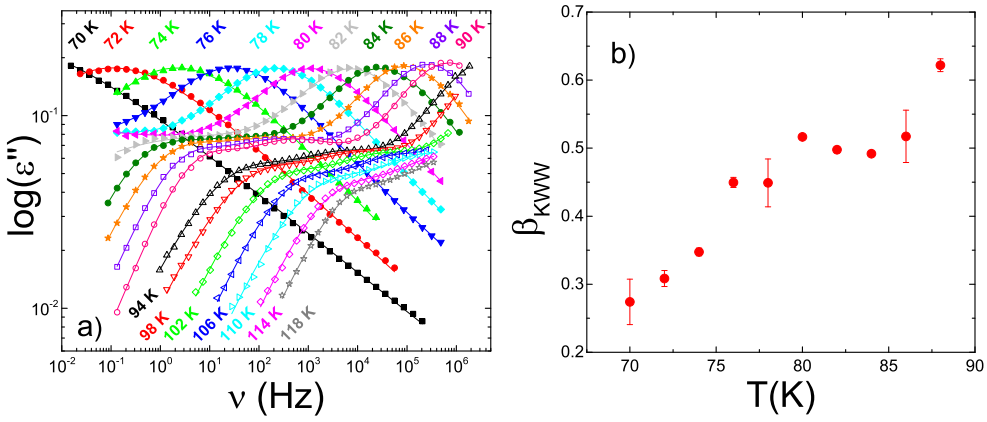

Figure 7.4: (a) Obtained dielectric spectra for several temperatures ranging from 70 to 118 K. (b) β_{KWW} exponent as a function of temperature.

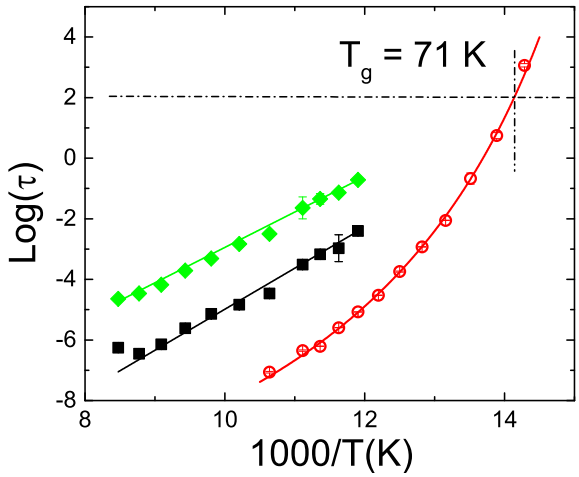

Figure 7.5: Relaxation time as a function of reciprocal temperature for both α (red circles) and other slower relaxations (23.24 kJmol^{-1} for green diamonds and 23.26 kJmol^{-1} for black squares) .

between 0.27 (at 70 K) and 0.62 (at 90 K). It strongly decreases with decreasing temperature, thus highlighting the increase of cooperativity due to strong orientational correlations between nearest neighbors. The temperature dependence of the α-relaxation time τ_α is much more pronounced than a (simply activated) Arrhenius behavior, and it was modeled with the VFT equation.

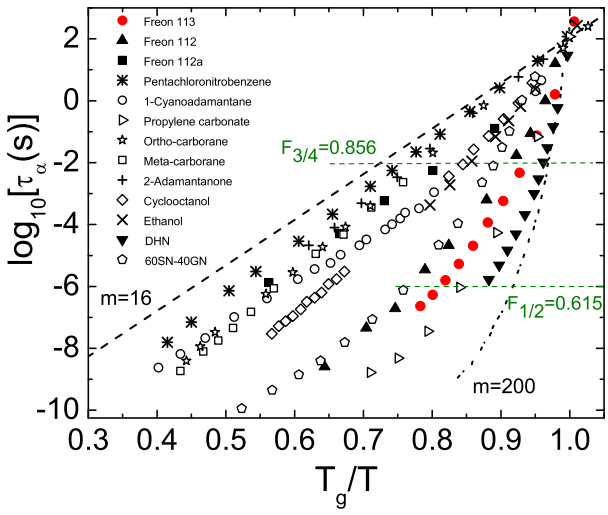

Figure 7.6: Relaxation time as a function of reciprocal of temperature scaled with T_g (Angell plot). VFT parameters for Freon113 are: $T_0 = 58.9 \pm 0.6$ K, $\tau_0 = (2.9 \pm 1.6) \cdot 10^{-12}$, $D = (6.4 \pm 0.5)$. Fragility calculated according to eq. (1) is $m = 127$.

Moreover, the α-relaxation time reaches 10^2 s, the conventional relaxation time for glass transition, at 71 ± 1 K. The calculated kinetic fragility index (eq. 2.3) provides a value of $m = 127$. Such value is the highest so far reported for an OG, as can be seen in Figure 7.6, in which relaxation time for several plastic crystals and some highly-fragile canonical glass formers are plotted as a function of the normalized temperature T_g/T. As far as the kinetic fragility $F_{1/2}$ and $F_{3/4}$ concerns, values of 0.615 and 0.856, respectively, are found.

7.5.2 Thermodynamic fragility

In Figure 7.7, we present previously published data [152] focused on the temperature range relevant here, around the glass-like transition between the OG and the plastic crystal, that is $T_g = 72$ K. They are in close agreement with the value obtained by dielectric measurements 71 ± 1 K. The inset shows for several substances a frequently used measure of thermodynamic fragility, namely the heat capacities C_p curves around T_g normalized to their corresponding values in the glassy state $C_{p,gl}$. A large $C_{p,liq}/C_{p,gl}$ ratio would indicate a high "thermodynamic fragility" whereas a low one would corre-

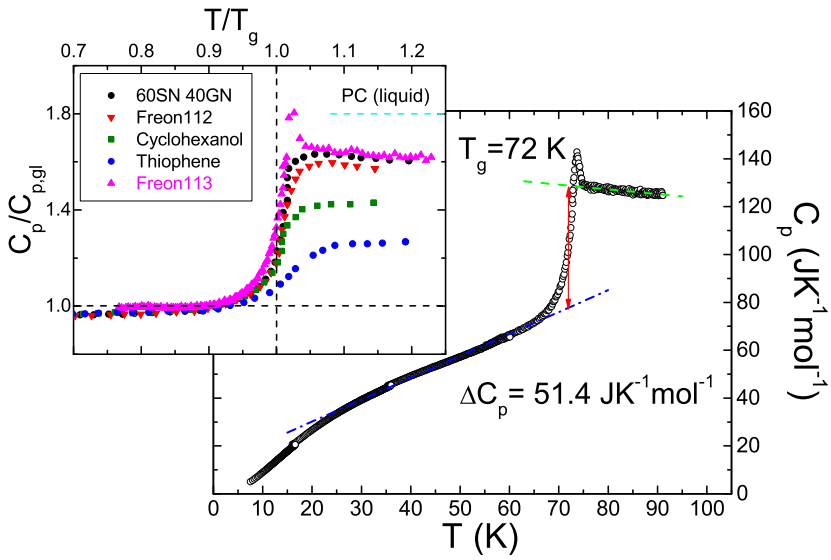

Figure 7.7: Measured specific heat of Freon113 [152] around the glass-like transition between the orientational glass and the plastic crystal around $T_g = 72$ K. In the inset is shown the specific heat jumps at the glass transition of several plastic crystals (or liquids) normalized to that of glass (orientational or structural). From top to bottom: succinonitrile 60 - glutaronitrile 40; Freon112; cyclohexanol; thiophene; Freon113. (Adapted from [168], also including data for Freon113).

spond to a "thermodynamically strong" glass former [166].

The entropy curve for the glassy crystal/plastic crystal (crystal I) phase below 125 K is shown in the inset of Figure 7.8, obtained after numerical integration of the corresponding specific heat curve of Figure 7.7, whereas the entropy data for the reference stable crystal II is taken from Kolesov *et al.* [169]. By subtracting the latter from the former one obtains the excess entropy $S_{exc}(T)$ of the glassy phase. The so-obtained excess entropy for Freon113 is presented in Figure 7.8 following the thermodynamic fragility plot introduced by Martinez and Angell [22]. One can see that Freon113 behaves as a very fragile glass-former thermodynamically too, with $T_g/T_{3/4} = 0.988$ and hence $F_{3/4} = 0.976$.

Debye-reduced vibrational density of states $g(\omega)/\omega^2$ and specific heat C_p/T^3 are plotted in Figure 7.9 for both Freon112 and Freon113. The boson peak of Freon113 is higher and occurs at a higher energy (1.9 meV, 5 K) than that of Freon112 (1.5 meV,

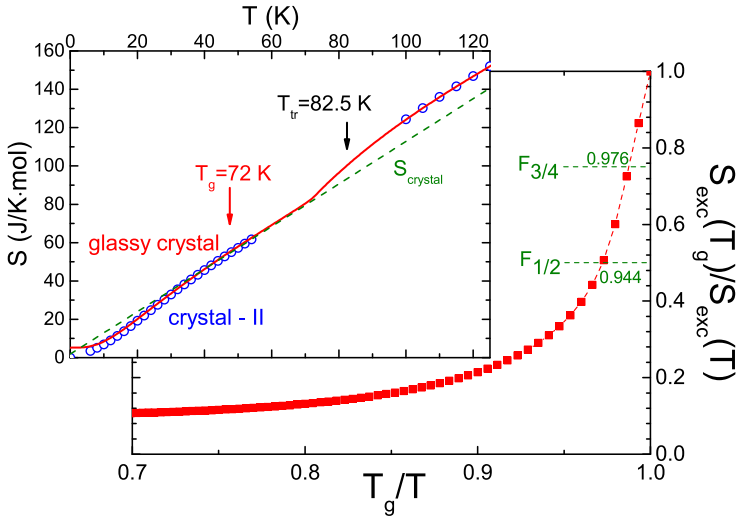

Figure 7.8: Reciprocal of the excess entropy, normalized by the excess entropy at T_g, as a function of reciprocal temperature scaled with T_g. Inset: Entropy for the plastic/glassy crystal phase (red solid line) and for the stable crystal II and the liquid (blue points, from [169]) as a function of temperature. The green dashed line indicates the extrapolation of the crystal II as a reference for higher temperatures. In both figures, the dashed lines drawn at the 1/2 and 3/4 marks are used to obtain either kinetic or thermodynamic fragilities $F_{1/2}$ and $F_{3/4}$, respectively.

4.5 K).

7.6 Discussion and conclusions

The fragility of glass-forming liquids has been correlated with their low-energy anomalous behavior in the glass state, as mentioned above. Sokolov et al. [155] found a negative correlation between the height of the boson peak in C_p/T^3 relative to the reference Debye level and the degree of fragility of the liquid, that is, the stronger the glass-forming liquid the higher its boson peak. We have plotted in Figure 7.10 the data tabulated by Sokolov et al. [155] as $(C_{p,exc}/T^3)_{max}/C_D$, where the numerator stands for the maximum C_p/T^3 at low temperature whereas the denominator stands for the Debye specific heat, as a function of the usual fragility index m.

In addition to those data from structural glasses, we have also plotted some data

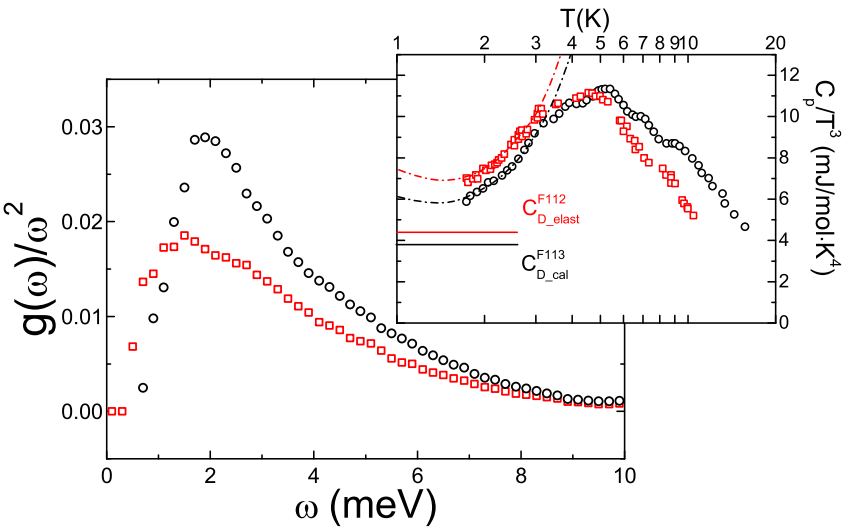

Figure 7.9: Debye-reduced vibrational density of states divided by $g(\omega)/\omega^2$ for Freon112 (open red squares) and for Freon113 (open black circles) determined at 5 K by means of inelastic neutron scattering at MARI spectrometer. Inset shows the molar heat capacity divided by T^3 for Freon112 and Freon113 [152] together with the calculated Debye values and the fits (dashed lines) corresponding to the soft potential model in a semi-log plot.

for OG including our current data for Freon113. The clear excess of low-frequency excitations in the density of states (Figure 7.9) for both Freon112 and Freon113, together with the evidence of their scattering with thermal acoustic phonons found through the thermal conductivity measurements [152] reveals the hybridization between intramolecular (torsional) degrees of freedom and acoustic phonon branches, an experimental fact that gives rise to the broad maximum in the reduced specific heat C_p/T^3 (inset in Figure 7.9).

Within the framework of the multidimensional energy landscape [174], the potential energy function $\phi\{r_i\}$ of the whole system which depends on the spatial location r_i for each of the pertaining particles, represents the "topography" of the configuration space of the many-body system, the minima being the stable arrangements of the system. These minima, their number and their depth, depend on the specificities of the system and, mainly, on the molecular structure and the inter- and intra-molecular interactions. Thus, the higher the number of distinct accessible states, the higher the number of

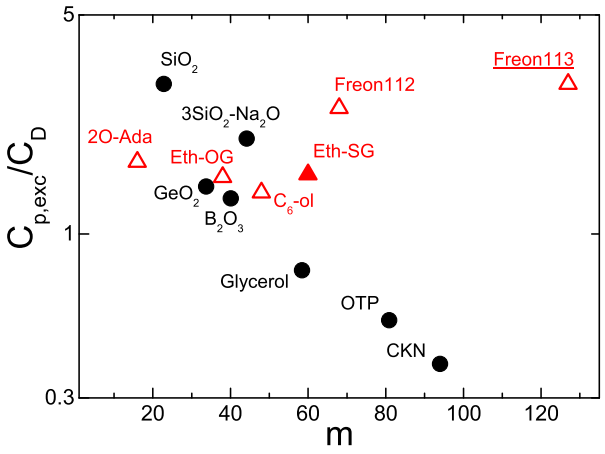

Figure 7.10: Excess heat capacity over the Debye value C_D at the boson-peak maximum $(C_{p,exc})_{max}$ scaled to C_D, as a function of the fragility index m in a semi-log scale. Black circles correspond to canonical glasses, taken from [155]. Red triangles show the present work on Freo113 and earlier works: adamantanone (2O-Ada) [170], cyclohexanol (C6-ol) [171], Freon112 [149], and ethanol both as orientational (Eth-OG) and structural (Eth-SG) glass [172, 173]. Solid symbols are structural glasses and open symbols are orientational glasses.

minima on the potential energy hypersurface. In other words, an increase in the configurational entropy, due to the vibrational contributions or to the existence of other excitations, in excess over the crystal, as those coming from the different conformers and torsional degrees of freedom, should provide a faster decrease of the relaxation time τ (according to the Adam-Gibbs equation). As demonstrated by means of molecular dynamics simulations [175] fragility depends on changes in the vibrational properties of individual energy minima and how the number of minima is spread in energy. This would mean that the low-energy intramolecular excitations increase such modes and consequently, increase the configurational entropy. The material studied is representative of systems with a high value of the configurational entropy due to the intramolecular modes, clearly emerging at the dielectric susceptibility as slower processes than the main α relaxation (Figure 7.5), as well as in the density of states (Figure 7.9).

As stated in Section 2.1.3, it is a common belief that the Kauzmann temperature T_K and the Vogel-Fulcher-Tammann temperature T_0 are close together, and that this

similarity connects the similar values between thermodynamic and kinetic fragility [22]. The easiest way for such connection is provided by the Adams-Gibbs equation (eq. 2.9), through the assumption that the configurational entropy $S_c \approx S_{exc}$ (*i.e.*, the vibrational entropy of the supercooled phase is approximately equal to that of the crystal phase) can be calculated by means of the specific heat difference between the glass and the supercooled liquid as a reciprocal function of temperature, $\Delta C_p = K/T$, K being a constant. Within these assumptions, VFT equation is directly obtained with $T_0 = T_K$ and $D = C/\Delta C_p(T_K)$ [176]. Despite such an analytical approach, Tanaka revealed the existence of a linear correlation between fragility and T_K/T_0, from which fragility decreases with the increase of T_k/T_0. The correlation, based on the two-order-parameter model [177,178], ascribes the decrease of the fragility with the increase of T_K/T_0 to the increase of the of short-range bond ordering which gives rise to a decrease in the entropy.

The Freon compounds here presented are representative cases of van der Waals molecular interactions but with strong short-range order [145] due to strong orientational correlations. These correlations are the result of the small energy difference between conformers but put apart by a large energy barrier, which strongly decreases with temperature, giving rise to strong coupling between these low energy frequency modes and the lattice motions. A consequence of the strong orientational correlation is evidenced by the extremely low value of the β_{KWW} exponent close to T_g (see Figure 7.5c). Such a picture would indicate that, on one hand, strong orientational correlation produces high kinetic fragility and, on the other, the low-energy excitations gives rise to an extra contribution to the excess entropy.

Moreover, the excess of low energy frequency modes contributing to the excess heat capacity over the Debye value C_D at the boson-peak maximum $[C_{p,exc}]_{max}$ (see Figure 7.10) are not related to the acoustic modes of the ordered phase (C_D) and thus, correlation between $[C_{p,exc}]_{max}$ as a function of the fragility index m (Figure 7.10) can break up.

The activation energy, which is found to decrease upon approaching T_g for these low-temperature glasses, increases in Freon113 as usually found for normal glasses. As a conclusion, we have demonstrated that the high values of kinetic and thermodynamic fragilities of Freon113 (the highest values found in a plastic crystal to the best of our knowledge) are accompanied by a strong coupling between low-energy modes due to the high number of intramolecular degrees of freedom and acoustic phonon branches.

Such modes contribute to the low temperature specific heat and to the density of states and, thus, to the excess (configurational) entropy, which makes the system thermodynamically and kinetically fragile. Finally we conclude that low energy frequency modes, which in an obvious way appear in the excess heat capacity over the Debye value C_D at the boson-peak maximum, are in most cases uncorrelated with those of the modes of the ordered phase, this making difficult a correlation between fragility and the excess specific heat, *i.e.*, the boson peak.

Chapter 8

Dynamical Scenarios in a Glass-forming Liquid

8.1 Introduction

The lack of a unique and shared theory in the microscopic description of liquid phase dynamics has led us to conduct a study, based on Bayesian inference methods through which a new perception about the sub-nanosecond dynamics has been given. The sample used for this purpose has been one of the prototypical glass-forming liquid, glycerol. This material is a structural glass former and, since it is used in wide range of applications, arouses a great scientific interest.

To this end, QENS data as a function of temperature have been analyzed using a minimal set of physical assumptions. On the basis of this analysis, we prove the presence of three distinct dynamical processes in glycerol, *i.e.*, a translational diffusion of the molecular centre of mass and two additional localized and temperature-independent modes. The neutron data also provide access to the characteristic length scales associated with these motions in a model-independent manner, from which we conclude that the faster (slower) localized motions probe longer (shorter) length scales. Careful Bayesian analysis of the entire scattering law favors a heterogeneous model for the dynamics of glycerol, where molecules undergo either the faster and longer or the slower and shorter localized motions.

In this Chapter we will first examine the characteristic time scales of these processes. Since our experiments have been performed as a function of temperature, we will also compare relaxation times with those obtained from dielectric spectroscopy, in order to gain additional insights into the nature of β_{JG}-relaxation phenomena. Finally, we ask whether our QENS data are better described by the HG or HT via recourse to two first-order models built with a minimum number of assumptions.

8.2 Previous works

Glycerol has been the object of several experimental investigations [179, 180]. The dynamics of glycerol have been studied by dielectric spectroscopy (DS) [81, 82, 181–183], depolarized light scattering [184], Nuclear Magnetic Resonance (NMR) [185, 186], and QENS [187–191]. Moreover, Molecular Dynamics (MD) simulations have been performed in order to explore the dynamics of this glass-forming liquid [192]. An early and quite extensive analysis of QENS data on glycerol was performed by Wuttke *et al.* [109, 193, 194] in the context of Mode Coupling Theory (MCT). This study made extensive use of phenomenological Kohlrausch-Williams-Watts (KWW) line shapes to describe the slow dynamics.

Despite such a high scientific efforts, a comprehensive, model independent, theoretical explanation of the microscopic driving mechanisms is still elusive. Many experiments were done using neutron scattering, but obtaining the diffusion coefficients from the measured quasielastic spectra requires a very high experimental care.

Very recently, Cicerone et al. [13] have shown that the picosecond (ps) dynamics of glycerol and other glass-forming liquids might be studied by recourse to a two-state scenario where tightly and loosely caged domains coexist. Moreover, the liquid dynamics seem to be driven primarily by structural features.

8.3 The properties of glycerol

Glycerol is an exceptional utility material with many application areas. The key of its versatility is a unique combination of physical and chemical properties, the compatibility with many other substances, and the non-toxicity to human health and to the environment. Due to its combination of not common properties, glycerol finds appli-

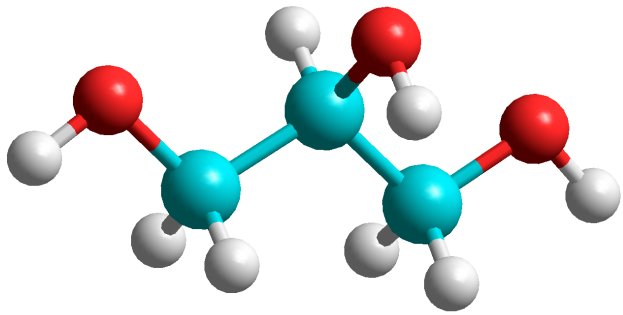

Figure 8.1: 3-D sketch of $C_3H_8O_3$ molecular structure in the vacuum. Carbon atoms are in blue, hydrogens in white and oxygen atoms in red.

cation in a wide variety of end uses, whose applications include some variety of areas ranging from food, to medicine, to urethane foams.

Glycerol has an important role in nature and is closely linked to the same processes on which life is based, being a fundamental component of all the cells. It occurs naturally in the form of triglycerides, the chemical combinations of fatty acids and glycerol which are the main constituents of almost all vegetable and animal fats and oils.

Chemically, Glycerol ($C_3H_8O_3$), shown in Figure 8.1, is a simple polyol compound (sugar alcohol) extremely stable in different conditions, and capable of producing multiple reactions, in fact because of its hydroxyl groups, it may react to form a unusually high number of derivatives. Glycerol is a clear, almost colorless, viscous liquid with a high boiling point and miscible in water and alcohol, and it is a good solvent. Among its most important features there are: the hygroscopicity, *i.e.* the ability to absorb humidity from the atmosphere, and the low vapor pressure, a combination that produces an exceptional plasticity.

The low vapor pressure allows the permanence of the glycerol in the products and it is closely linked to the hygroscopicity in the efficacy of glycerol to attract and retain the humidity (humectant). It is practically non-volatile at normal temperatures of use. In addition, between 0°C and 70°C temperature changes have little effect on the relative vapor pressure of glycerol solutions.

A direct plasticizing effect is produced, in most of the applications for glycerol, as a humectant-plasticizer because glycerol and water act together to increase the softness

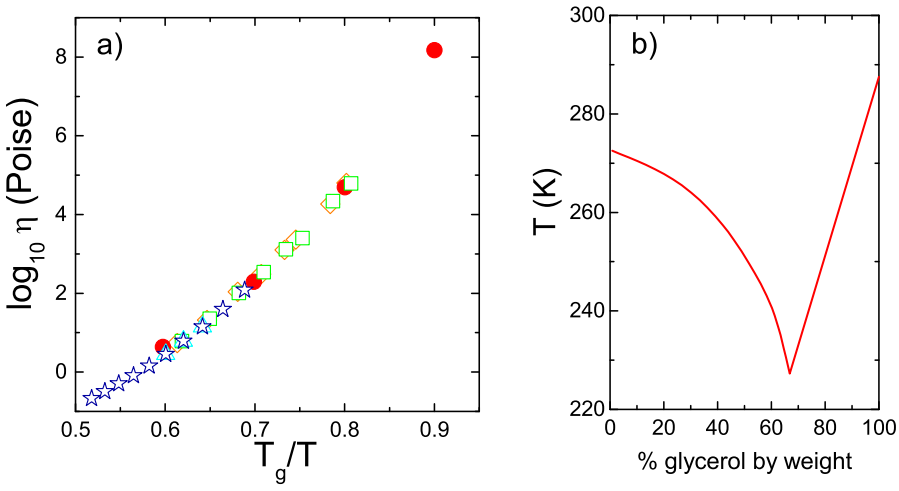

Figure 8.2: (a) The T_g scaled Arrhenius presentation of viscosity data for glycerol. The scaling temperature is the calorimetric glass transition temperature [195]. Data were collected from different sources: orange diamonds [196], full red circles [195], green squares [197], light blue triangles [198] and blue stars [199]. (b) Sketch of freezing points of glycerol-water solutions [200].

and flexibility and to prevent drying. The plasticizing effect, however, is more than just the result of glycerol to retain water. Even when there is not presence of water, glycerol can perform a direct function of plasticizing effect [201].

The high viscosity (Figure 8.2a) is one of the most characteristic traits of glycerol, such quality is of great worth in various mechanical applications that use glycerol as a hydraulic fluid or special lubricant, but the most important commercial use, given its viscosity, is the ability of densification for liquid preparations, syrups, emulsions and gels. At low temperature, concentrated glycerol solutions tend to a supercooled regime. In this regime, at first its viscosity increases slowly, and then have an abrupt increase, up to the glass transition which occurs at about 185 K.

Hence, through the use of glycerol, it is possible to avoid the crystallization, the phenomenon that adversely affects the quality and preservation of the products. The freezing points of various glycerol concentrations are shown in Figure 8.2b. These values explain why the pure glycerol, with a freezing point of about 291 K, is rarely seen in the crystalline state. As it is evident from these data, even the small amount of water

generally present in most of the formulations of glycerol depress the freezing point. A combination of two parts of glycerol to one part water form a eutectic mixture (a mixture of substances whose melting point is lower than that of the individual substances that compose it) which freezes at 227 K [201].

In the present study, all measurements were performed using a glycerol sample purchased from Sigma Aldrich with a purity greater than 99%.

8.4 Experimental details

QENS experiments were performed using the TOFTOF spectrometer, described in Section 3.3.2, using a resolution of 55 µeV (full width at half maximum) [202]. The samples were kept in hollow aluminium cylinders with a sample layer thickness of 0.1 mm. This thin layer ensures a transmission of $\sim 85\%$, thereby rendering multiple scattering effects small. The sample temperature was controlled with a closed-cycle refrigerator, to collect QENS data at $T = 292, 316, 345, 380$ K, corresponding to $T_g/T = 0.65, 0.60, 0.55, 0.50$.

The program FRIDA [55] was used for data reduction. From the time-of-flight of the neutrons, the energy transfer between neutron and sample was calculated; the measured double differential neutron scattering cross section was transformed into the scattering function; an angle- and energy-dependent absorption correction was performed on both, the sample measurements and the measurement of a vanadium standard which was used to determine the detector efficiencies and the instrumental resolution; the detector efficiencies were normalized; and finally the momentum transfer Q was calculated from the scattering angle and the energy transfer and slices of constant Q were grouped together in bins of 0.1 Å^{-1}. As shown in Figure 8.3, the Q-range analyzed is between $0.6\,\text{Å}^{-1}$ and $1.3\,\text{Å}^{-1}$ where the coherent contribution is negligible. In energy, the spectra were evaluated in the whole accessible region.

The analysis of the data has been performed using a Bayesian approach described in [39,111,115,203] and in Chapter 5. Model selection is then performed by considering the information content of entire χ^2 probability density functions (PDFs). All data analysis presented herein have been performed using the FABADA (Section 5.4).

QENS data have been fitted with a free or parametrized distribution of modes so that the scattering function $S(Q,\omega)$ can be described as a function of momentum ($\hbar Q$)

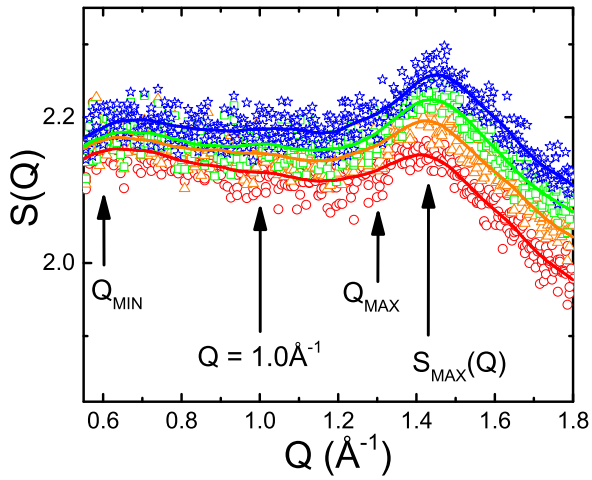

Figure 8.3: Static structure factor $S(Q)$ for glycerol at $T = 380$ K (red circles), 345 K (orange triangles), 316 K (green squares) and 292 K (blue stars). The Q-range analyzed is $Q_{\min} = 0.6$ Å^{-1} to $Q_{\max} = 1.3$ Å^{-1}. This region is sufficiently far away from the structure factor maximum $S_{\max}$ at around 1.4 Å^{-1} to avoid strong contributions of coherent scattering. $Q = 1.0$ Å^{-1} is shown because the dynamic range is maximal for this momentum transfer, and so is the amount of information contained in the data. The solid lines are guides to the eye.

and energy ($\hbar\omega$) transfer by [204]:

$$S(Q,\omega) = A(Q)\delta(\omega) + \sum_{i=1}^{n} B_i(Q,\Gamma_i)\frac{1}{\pi}\left(\frac{\Gamma_i}{\omega^2+\Gamma_i^2}\right) \tag{8.1}$$

where Γ_i is the energy width of the i-th Lorentzian function and $B_i(Q,\Gamma_i)$ is the weight for each Lorentzian, being thus the collection of $\{B_i(Q,\Gamma_i)\}, i = 1, ..., N$ the normalized probability distribution function describing the dynamics of the system. $B_i(Q,\Gamma_i)$ can be easily transformed to the time domain so that the intermediate scattering function $I(Q,t)$ can be written down as a distribution of simple exponential functions weighted by $B_i(Q,\tau_i)$ [204].

In order to perform the analysis, the theoretical function $S(Q,\omega)$ must be convolved with the instrumental resolution $R(Q,\omega)$ in the energy dimension before comparison to the measured data. When the width of the theoretical function Γ is close to the width of the energy bins of the data $\Delta\omega$, the convolution process artificially increases the broadening Γ [205]. This artifact is especially prominent when fitting a diffusion

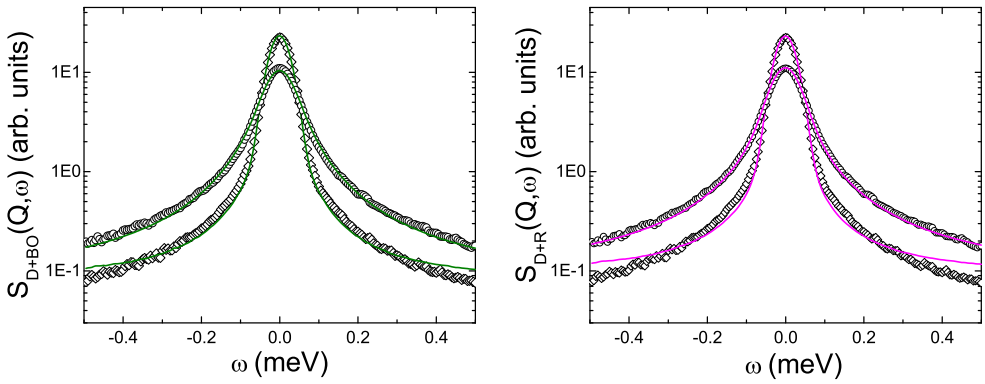

Figure 8.4: Experimental data together with the bests fit to two different models: Diffusion + Brownian oscillator (left) and Diffusion + Rotational motion (right) for Glycerol at $T = 380$ K with a resolution of 55μeV. For these two models are presented two spectra and relative fits at the same Q values (open diamonds for $Q = 0.5$ Å^{-1} and open circles for $Q = 1.1$ Å^{-1}).

process, since in this case Γ is proportional to Q^2. The calculated value of Γ is therefore larger than the true one in the low Q region. In other words, as soon as the line width Γ is similar to the energy bin width $\Delta\omega$, a deviation from the Q^2 behaviour is observed which is not related to any physical process, but to a numerical problem of the convolution. In order to avoid this effect, the bin width must be chosen smaller than twice the extracted line width, *i.e.* $\Delta\omega \leq 2\Gamma$ [205].

8.5 Results

8.5.1 Preliminary analysis

The first stage of our analysis has been based on the large amount of information in the literature concerning the dynamics of glycerol in the liquid phase [103, 109, 180–182, 185, 187–190, 206]. On these basis spectra were evaluated in the region between -0.5 to $+0.5$ meV. In order to investigate which motions are taking place at a microscopic level. We have tested two physical models, both including a diffusion term and a confined motion.

First of all we checked in model where the particle executes a Brownian motion in

an harmonic potential, the so called Brownian Oscillator (BO) [207]. The quasielastic scattering function is thus described in terms of a Lorentzian function related to the diffusion (D) with a broadening $\Gamma_D(Q) = DQ^2$, and the broadening related to the Brownian oscillator, Γ_{BO}. The scattering law can be written as:

$$S(Q,\omega) = L(\Gamma_D) \otimes \left(A_0(Q) + \sum_{m=1}^{\infty} A_m(Q) \frac{1}{\pi} \frac{m \cdot \Gamma_{BO}}{\omega^2 + (m \cdot \Gamma_{BO})^2} \right) \tag{8.2}$$

$$\text{with} \qquad A_0(Q) = e^{-Q^2\epsilon^2} \qquad \text{and} \qquad A_m(Q) = (Q^{2m}\epsilon^{2m})/m! \ .$$

For the second model a rotational motion has been assigned to the confined motion. We called this model Diffusion + Rotational motion (D+R) and the scattering law can be expressed as:

$$S(Q,\omega) = L(\Gamma_D) \otimes \left(A_0(Q) + \sum_{l=1}^{\infty} A_l(Q) \frac{1}{\pi} \frac{\Gamma_{rot}}{\omega^2 + (\Gamma_{rot})^2} \right) \tag{8.3}$$

$$\text{with} \qquad A_0(Q) = j_0^2(QR) \qquad \text{and} \qquad A_m(Q) = (2l+1) j_l^2(QR) \ ,$$

where $\Gamma_{rot} = l(l+1)D_{rot}$ and j_l are the spherical Bessel functions of l-th order.

Fits were performed to the data at all Q-values simultaneously, in a way to fit, at once, both processes and avoid cumulative errors. In Figure 8.4, we show two examples of the best fits to the data at two values of momentum transfer ($Q = 0.5$ Å^{-1} and at $Q = 1.1$ Å^{-1}).

As can be seen, at first glance, both models are able to fit the data reasonably well in the quasielastic peak region ($\omega \approx 0$), however, the low quality of the fit on the tails is also evident. This has inevitably caused questions on the effectiveness of the used models, and especially on the number of modes present in glycerol dynamics.

Furthermore, given the absence of inelastic contributions in the energy range measured, lead us us to reconsider the whole energy range in which to perform the fit procedure.

8.5.2 Determination of the number of processes

To determine how many dynamical processes are present in the measured dynamics of glycerol, a series of plausible and widely used models has been analyzed, namely: a

two Lorentzian model (2L), a distribution of modes described by two Gaussian PDFs, and another one described by a KWW plus a Gaussian PDF (G+KWW). We have also compared all of these two-component models with a simple three-Lorentzian model (3L) and, for the sake of consistency, also to a single KWW distribution. In all cases, fits to the data were performed after convolution with the spectral resolution of the instrument. Figure 8.5 shows the results of such analysis and the resulting χ^2 PDFs at $T = 380$ K and $Q = 1.0$ Å^{-1}. Model selection has been performed with FABADA [111,115,144] at $Q = 1.0$ Å^{-1} because the dynamic range and, therefore, the information content of QENS spectra are maximal at this particular Q. This momentum transfer is dominated by incoherent scattering, as it lies significantly below the first and most pronounced maximum of the measured structure factor located at $Q_{max} = 1.4$ Å^{-1} (see also Figure 8.3).

Inspection of the resulting χ^2 PDFs evinces that the 3L model provides the best description of the experimental data (see Figure 8.5). Although one might argue that this conclusion could very well be the result of an increase in the number of fit parameters relative to simpler models, inspection of the underlying and well-separated χ^2 PDFs rules out this possibility in glycerol. In other words, the two-component model fits using any combination of parameters are invariably worse than those corresponding to the 3L model.

Given the popularity of the G+KWW model, we have also performed a series of additional fits to obtain values for the "stretching" parameter β_{KWW} at $Q = 1.0$ Å^{-1} as a function of temperature. At the lowest (highest) temperature, we find $\beta_{\mathrm{KWW}} \approx 0.5$ (0.7). These values are in closer agreement with dielectric spectroscopy [81,181–183] than previous QENS studies [194]. Notwithstanding this encouraging result, we stress that our Bayesian analysis does not favour this particular model, as evidenced by the results shown in Figure 8.5.

8.5.3 Model comparison: homogeneous vs. heterogeneous

In order to gain further insights into the physical basis of the three processes described by the 3L model in glycerol, we have performed further model selection on the *entire scattering function* $S(Q,\omega)$ accessible in the QENS experiments. The aim is to elucidate whether, in addition to the expected translational diffusion of the molecular centre of

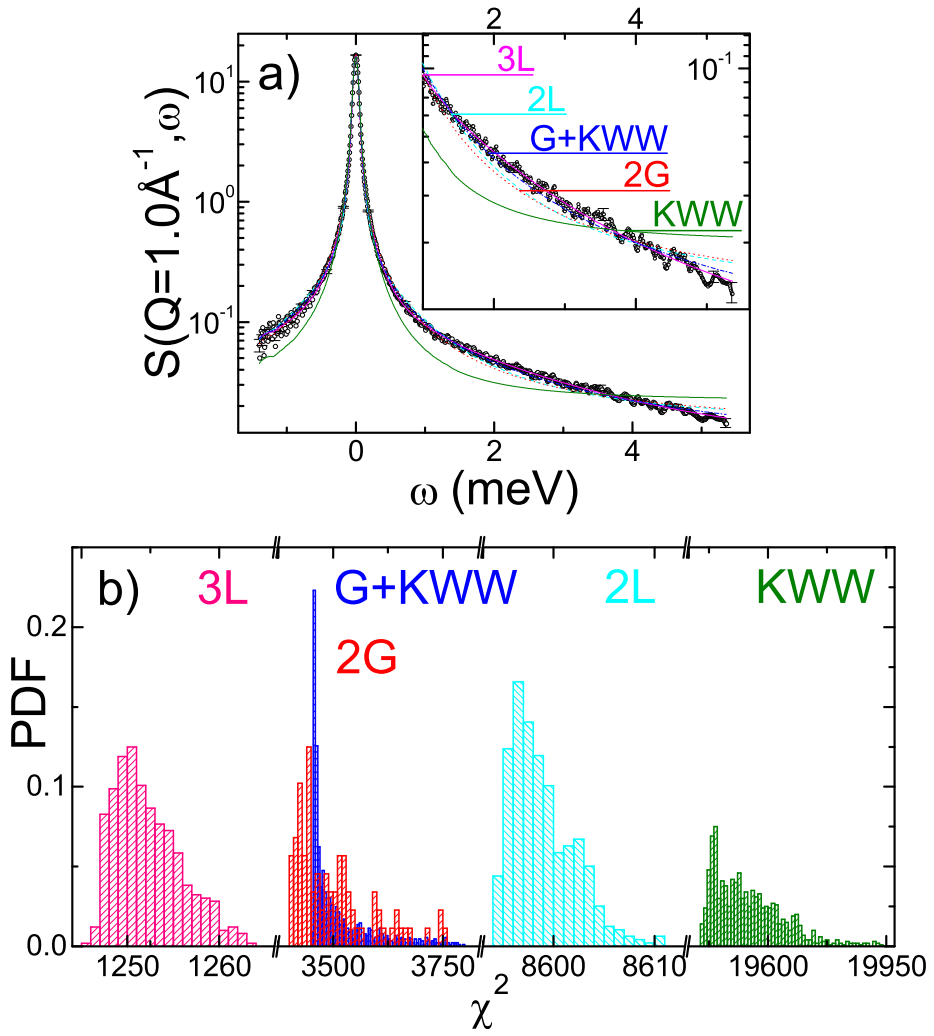

Figure 8.5: (a) Data fits for glycerol at $T = 380$ K and $Q = 1.0$ Å^{-1} using different models: two lorentzians (2L), three lorentzians (3L), a single KWW relaxation (KWW), KWW plus a Gaussian distribution of relaxation times (KWW+G), and two Gaussian distributions (2G). Using the same colors, panel (b) shows the corresponding χ^2 PDFs.

mass, all molecules are subjected to: either two additional (and distinct) relaxation processes affecting the entire ensemble (HG); or if some molecules are moving faster than others giving rise to so-called islands of mobility (HT) [95, 208]. Let us recall the two models presented in Section 3.5.2. Mathematically the HG can be described by a multiplicative ansatz of dynamical processes in the time domain and, as such, it affects

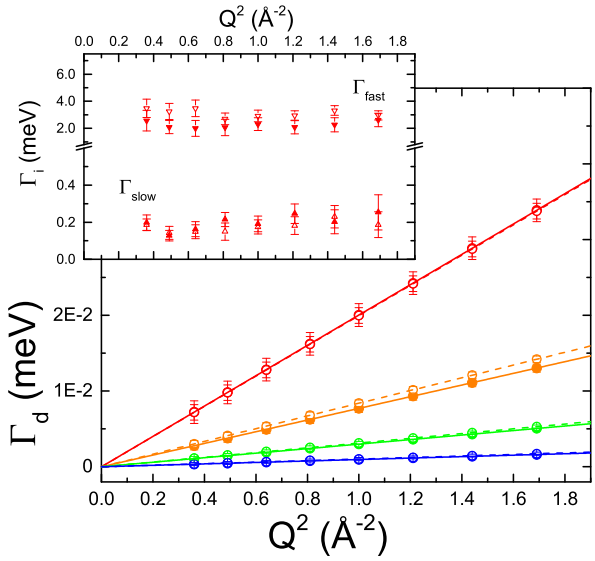

Figure 8.6: Q-dependent linewidth Γ_d (HWHM) of $S(Q,\omega)$ for different temperatures. At each temperature, a clear Q^2 dependence of Γ_d is observed, compatible with a diffusive motion. The lines show the best fits of the function $\Gamma_d = DQ^2$ to the data. It is evident that diffusion coefficients D obtained for the two models HG (full symbols and solid lines) and HT (open symbols and dashed lines) are very similar.

all molecules on the time scale of the α-relaxation. The HT, on the other hand, is based on the arithmetic sum of two processes, each one affecting a certain percentage of molecules at α-relaxation time scales. With these considerations in mind, the simplest (two-state) incoherent scattering functions for the HT and HG read, respectively,

$$\begin{aligned} S(Q,\omega)_{HG} &= y_0 + L_D \otimes [a(Q)\cdot\delta(\omega) + (1-a(Q))\,L_a] \otimes \\ &\quad [b(Q)\cdot\delta(\omega) + (1-b(Q))\,L_b] \end{aligned} \tag{8.4}$$

$$\begin{aligned} S(Q,\omega)_{HT} &= y_0 + L_D \otimes \{P\,[a(Q)\cdot\delta(\omega) + (1-a(Q))\,L_a] + \\ &\quad (1-P)\,[b(Q)\cdot\delta(\omega) + (1-b(Q))\,L_b]\}. \end{aligned} \tag{8.5}$$

where L_D is a Lorentzian line describing translational diffusion with a spectral width proportional to the square of the momentum transfer, that is, $\Gamma = DQ^2$, where D is the translational diffusion coefficient. We note the intrinsic (linear) dependence of D on Q^2, a relation that has been used to describe the experimental data as a function

of Q using a single fit parameter D. The remaining (localized) motions are described by $[P_i(Q) \cdot \delta(\omega) + (1 - P_i(Q))\, L_{P_i}]$ with $P_i = a, b$. The dependence of the form factors $a(Q)$ and $b(Q)$ on Q provides a measure of the associated length scales for these motions.

In order to establish whether the spectral widths Γ_i associated with localized motions are Q-independent, we have allowed these to vary across Q at all temperatures.

Results for $T = 380$ K are shown in the inset of Figure 8.6 and demonstrate that, within experimental uncertainties, they are Q-independent. In view of the above, we have replaced a total of 16 parameters (2 Lorentzian widths across 8 independent Q-values) by 2 Q-independent spectral widths which were then fit simultaneously across all Q slices. This reduction in the number of adjustable parameters results in a drastic decrease in error bars of parameters. As explicitly shown by eqs. (8.4)-(8.5), the use of Q-independent spectral widths to describe the localized modes does not imply that the resulting Lorentzian modes present a constant width, since convolution with the translational component necessarily leads to spectral features of width $\Gamma_i + DQ^2$.

The results of this analysis at two Qs are shown in Figure 8.7a (an overview over all fits are shown in Figure 8.8), demonstrating that both scenarios can describe the QENS data well. The resulting χ^2 PDFs are shown in Figure 8.7b, where χ^2 values correspond to global values across all energy and momentum transfers probed by QENS. Figure 8.7b serves to highlight a significant overlap of the χ^2 PDFs for both models, which means that model selection in this particular case is certainly more ambiguous than in the previous case dealing with a determination of the total number of distinct dynamical processes. Although in this case the HT is preferred (both the minimum and maximum of the χ^2 PDF are located at lower values), it is still possible that additional information encoded in an improved prior (or new measurements over a wider range of length and timescales) could change the above conclusion. In any case, given the information at hand, *the HT is favored.*

Physical parameters

In both models, the peak is described by a Lorentzian line shape with a half width at half maximum (HWHM) Γ_d which is related to the diffusion coefficient D by $\Gamma_d = DQ^2$. The diffusion coefficient is obtained for each temperature and for the two tested models (see Figure 8.6). Across the whole temperature range, the value of the diffusion coefficient is basically independent of the employed model (HG or HT).

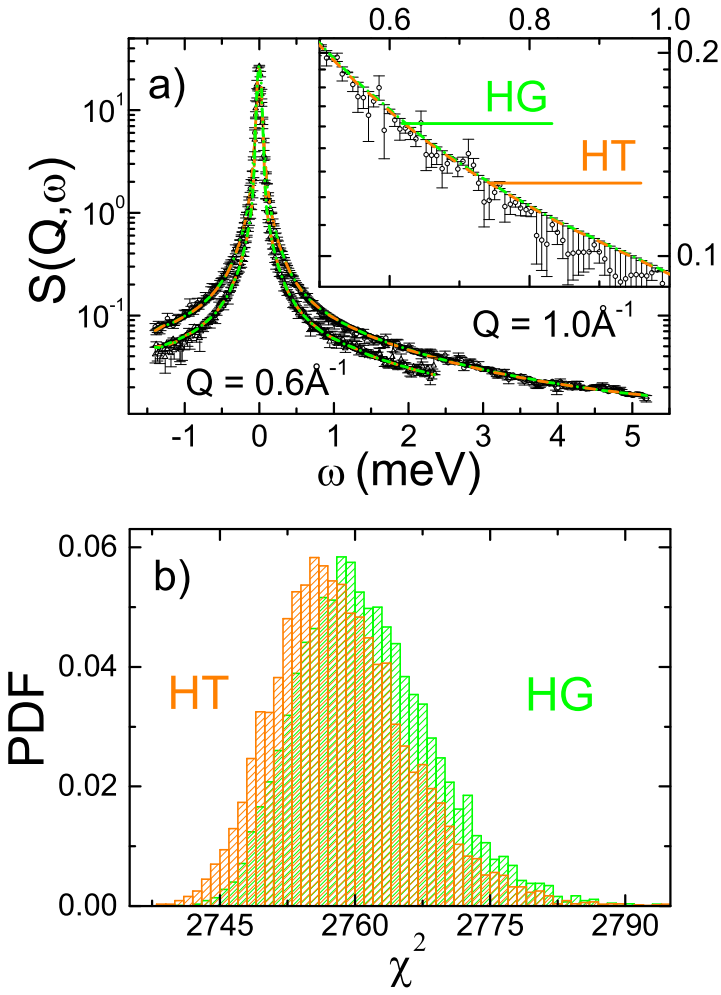

Figure 8.7: (a) Representative QENS spectra for glycerol at $T = 380$ K and associated fits for the HT/HG (solid/dashed lines); (b) χ^2 PDFs obtained from global fits over the *entire scattering function* as discussed in the main text.

Figure 8.9 reports the relaxation times $\tau_i = \hbar/\Gamma_i$ obtained for all three processes of the HT and HG model. First of all, we find that the obtained τ_is are independent of the model chosen and, therefore, their determination is robust. In addition to the relaxation times τ_{slow} and τ_{fast} associated with the two localized processes, we also show the relaxation time τ_{max} at Q_{max}, a dynamical quantity that describes the collective dynamics. As shown in Figure 8.9, the temperature dependence of τ_{max} is in good

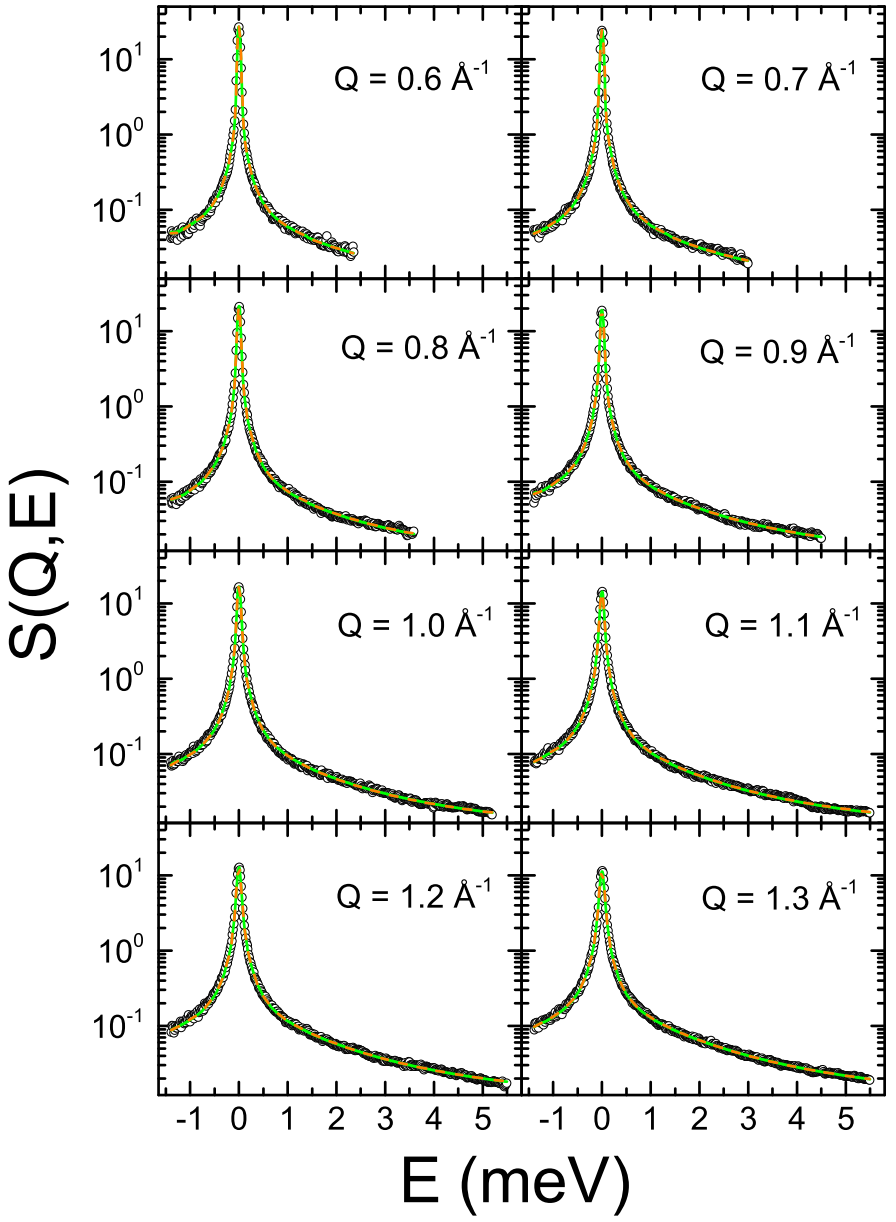

Figure 8.8: The quasielastic scattering function $S(Q,\omega)$ of glycerol (at 380K) for all values of Q evaluated in this work. Also shown are the best fits with the two models HG (solid green line) and HT (dashed orange line).

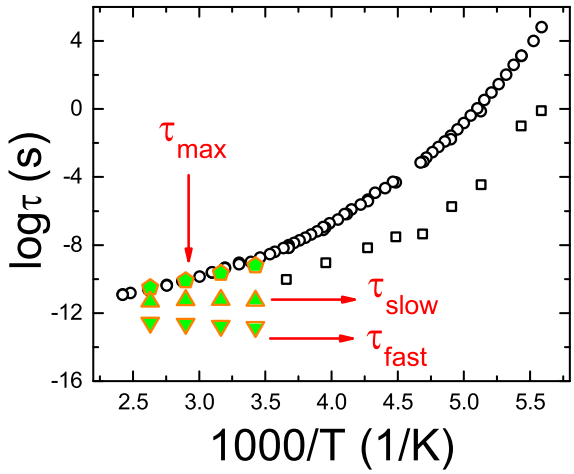

Figure 8.9: Relaxation map of glycerol as a function of reciprocal temperature. Open (filled) symbols represent DS (QENS) data. On the scale of this map, relaxation times for the HT and HG are indistinguishable.

agreement with collective α-relaxation data measured with DS [81, 181–183]. These two datasets deviate slightly from each other as the temperature is lowered because the timescales associated with translational diffusion increase and, as a result, they approach the intrinsic energy resolution of the QENS experiments [53]. As discussed previously [209], the translational diffusion coefficients obtained from the QENS data are in line with literature values. Thus, we may conclude that our quantitative determination of translational diffusion coefficients is robust, further corroborating the physical validity of the priors defined by eqs. (8.4)-(8.5). Concerning the localized modes, we find $\tau_{\mathrm{fast}} = 0.2\,\mathrm{ps}$ and $\tau_{\mathrm{slow}} = 5.5\,\mathrm{ps}$, and both are insensitive to temperature.

This insensitivity to temperature has been observed in other prototypical strongly associated liquids like hydrogen fluoride [210, 211]. Whether this behavior is characteristic of this family of complex liquids remains an open question. On the basis of these considerations, it is unlikely that the β_{JG} relaxation measured by DS [82] is related to these dynamical processes probed by QENS (see Figure 8.9).

The analysis of the neutron scattering spectra does not only allow to extract the rates or relaxation times of the processes but it is also possible to determine the length scale of the two confined motions. The terms describing these motions of the molecule

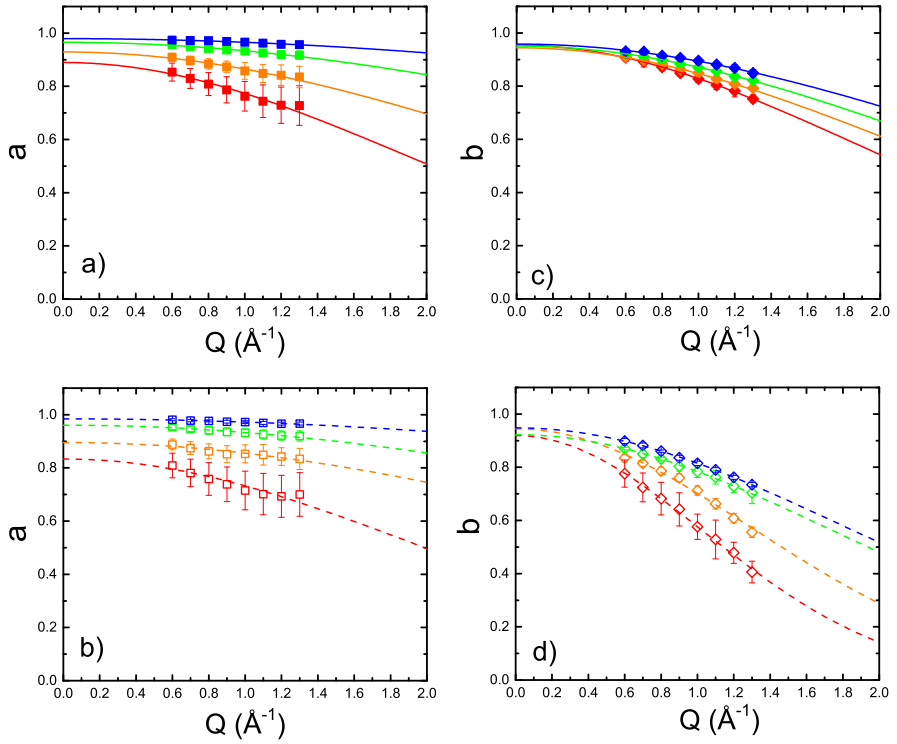

Figure 8.10: Q-dependence of the parameters a (panels a and b) and b (panels c and d) for each temperature extracted from both, the HG model (panels a and c) and HT model (panels b and d). Also shown are fits of $C\exp(-\pi^2\sigma^2Q^2)$.

and tagged as *slow* and *fast*, respectively, are given in the scattering function by $[P_i(Q)\cdot\delta(\omega)+(1-P_i(Q))L_{P_i}]$ where $P_i=a,b$. In Figure 8.10 we present the Q-dependence of parameters a and b for the two models and at all temperatures. These parameters exhibit the same overall behaviour, namely they decrease with increasing Q or T. Length scales σ associated with slow (τ_{slow}) and fast (τ_{fast}) dynamical processes have been obtained by considering the first term of the cumulant expansion of the structure factor [212,213], a Gaussian term in Q that may be written as $C\exp\left(-\pi^2\sigma^2Q^2\right)$. The prefactor C in this cumulant expansion is used to account for multiple-scattering effects, which translate into an effective reduction of the Elastic Incoherent Structure Factor obtained from the QENS data [205]. The fits to the data can be seen in Figure 8.10.

For both the HT and HG, we find that the shorter length scales correspond to

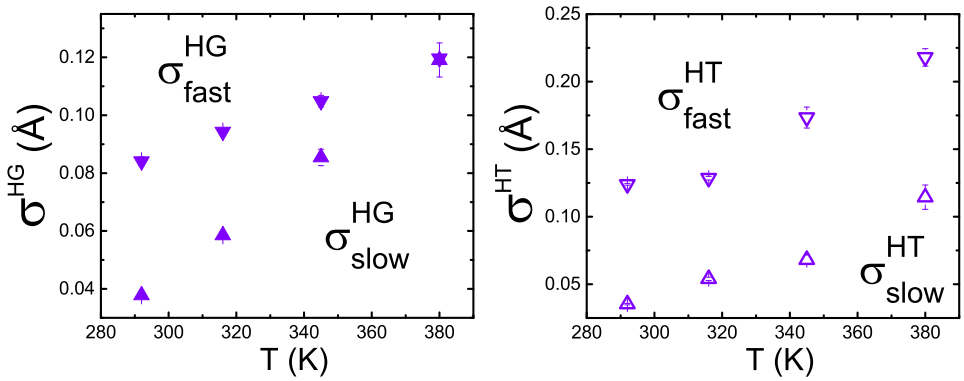

Figure 8.11: Length scales associated with the slow and fast localized relaxation modes of the HG and the HT.

"slow" movements taking place in the picosecond time range and longer length scales are associated with "fast" movements. This somewhat counter-intuitive result is physically plausible provided that these two motions conform to different microscopic mechanisms. In this context, the microscopic picture recently proposed by Cicerone et al. [13] offers a natural explanation of our results.

The σ values are model dependent both in terms of their magnitude and overall temperature dependence, but in both the HT and HG, they increase with temperature and are invariably larger for faster motions. For the HT, however, both length scales are distinctly different over the entire temperature range investigated in this work, whereas for the HG both length scales converge to the same value at the highest temperature investigated – while the two motions stay well separated with regards to their speed. The HT scenario consists of two populations (slow and fast molecules) the ratio of which shifts with rising temperature in favor of more fast molecules (Figures 8.11-8.12).

8.6 Discussion and conclusions

The analysis of the QENS data leads us to the unequivocal conclusion that there are three distinct dynamical processes taking place in liquid glycerol: one associated with the centre-of-mass translational diffusion of the molecule as a whole; and the other two corresponding to localized picosecond (slow) and sub-picosecond (fast) motions, both of which are insensitive to temperature. This result, together with our finding that

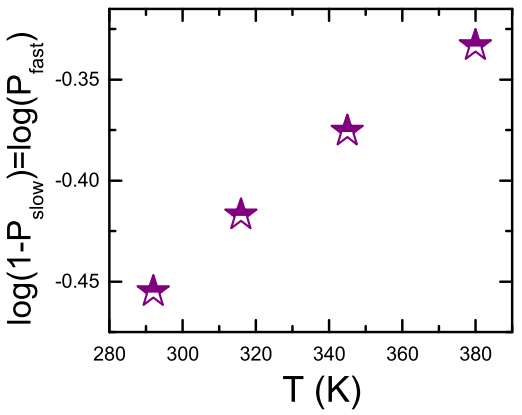

Figure 8.12: The panel shows the proportion of molecules performing the fast motion in the HT scenario.

fast (slow) motions take place over long (short) length scales are *independent of the underlying model chosen to fit the experimental data.*

Concerning the localized motions, it has to be noted that the information provided by the measured scattering function is not sufficient to establish a clear-cut preference for either physical scenario; the HT is favored over the HG but we cannot exclude that additional information might revert this order.

For the less likely HG, *all molecules* would be subjected to the same two types of motions, which we call rattling and hopping, at *all times* and also these two mechanisms would need to hold at all temperatures. The (smaller) rattling motion would need to occur on a slower time scale than the (larger) hopping and, at temperatures approaching $T = 380\,\mathrm{K}$, the two length scales merge (Figures 8.11-8.12), although their associated relaxation times are still clearly different (Figure 8.9). Our results for the HG scenario at high temperatures are also compatible with the microscopic mechanism proposed by Mamontov [191], with rattling motions described by confined diffusion on a sphere and fast motions by intramolecular localized motions.

Given the information encoded in our QENS data, the HT is the more plausible option, whereby a sizable and temperature-dependent fraction of the molecular ensemble undergoes faster motions over longer length scales. Following the work of Cicerone et al. [13], these motions would be associated with molecules belonging to regions in the fluid dominated by collective dynamics. The remainder of the ensemble would then

move more slowly over shorter length scales, a contribution that one could tentatively ascribe to "normal-liquid regions" [12]. These motions are well separated in relaxation time over the entire temperature range investigated, and show no signs of merging into a single dynamical process.

Conclusions

This thesis aimed to study the molecular dynamics in different compounds. The knowledge of the molecular motions in disordered systems is fundamental to understand their behavior in the microscopic scale. The study of the dynamics in disordered materials, however, is intrinsically complex due to the presence of many interactions. Thus, there is not a univocal physical description and many assumptions have to be made. Driven by this scientific challenge, the study of the dynamics in different compounds by means of different methods of investigation have been grouped in this thesis.

Bayesian approach allows to make few assumptions with respect other analytical methods, taking into account the correlations between parameters, and showing the complexity of the fit through the probability distribution functions. Using this method three compounds, showing different kinds of disorder, were studied: 1-chloroadamantane and freon113 exhibit an orientational disorder, while glycerol molecules, being in liquid phase, presents both orientational and translational disorder.

For what concerns 1-Chloroadamantane, Bayesian analysis has been used to prove the number of dynamical processes that better describe the data obtained from quasielastic neutron experiment in its plastic phase temperature range. A model selection through χ^2 PDFs shows that the anisotropic rotational model is favored and the analysis of the spectra has permitted to determine the rotational diffusion coefficients D_x and D_z. Both show a kink around 320 K.
Furthermore, the analysis of the diffraction patterns has evidenced a step-like behavior of the lattice parameter around the same temperature.
These two phenomena could be related with the anomalous calorimetric effect detected by Kobashi [8]. Thus, the dynamical changes in rotations and the change in structure seem to be correlated.

A dynamic and thermodynamic study of the orientational glass former Freon113 (1,1,2-trichloro-1,2,2-trifluoroethane, CCl_2F-$CClF_2$) has been presented in order to analyze its kinetic and thermodynamic fragilities. The properties of this material, in particular the internal molecular degrees of freedom, give rise to a complex energy landscape. Through the study of the orientational dynamics obtained by means of dielectric spectroscopy, together with the specific heat and the vibrational density of states from inelastic neutron scattering, we show that the high values of kinetic and thermodynamic fragilities of this OD phase (the highest values found in a plastic crystal) are accompanied by a strong coupling between low-energy modes due to the high number of intramolecular degrees of freedom and acoustic phonon branches. These modes contribute to the low temperature specific heat and to the density of states and, thus, to the excess (configurational) entropy, which makes the system thermodynamically and kinetically fragile.

Glycerol is one the most studied glass-formers. Here, a robust model selection, based on statistical assumption, has been presented. Line-shape analysis has shown the presence of three distinct processes in the description of molecular dynamics in liquid phase. One of such motions is associated with the translation of the center of mass of the whole molecule, while the other two are fast and slow movements that describe the transient confinement of the molecule created by the surrounding molecules.
Although the model selection has not clarified the problem, the heteregeneous model seems to be the one that best describes the quasielastic data. Probably this can be ascribed to the presence of heterogeneities, temperature-dependent domains, in which a fraction of molecules is subjected to faster movements (associated with the collective dynamics) and regions where molecules move slower over shorter length scales. The relaxation times of such motions are well separated and they do not seem to merge in single dynamical process in the temperature region examined.

The methods and procedures described in this work can be used to increase our knowledge in the dynamics of disordered systems. Although it remains a lot to do for a complete understanding of the behavior of disordered materials, this contribution will help to give some hints for further experiments and analysis.

Acknowledgments

The first thanks goes to Dr. Luis Carlos Pardo. Careful and generous, he has been able to teach me a lot with seriousness and sympathy. He has been an extraordinary supervisor, giving me all the tools and hints through all the project. His passion and his "electricity" have been an example for me and allowed me to reach the end of this trip... Mil Gracias Boss... aunque mil son pocas!

A sincere thanks to the "Big Boss", Prof. Dr. Josep Lluis Tamarit, man of science, able to teach not to give up, to improve and always with a smile.

Thanks to Prof. Dr. Maria Del Barrio, for all the suggestions during the experiments in the laboratory.

Thanks to Dr. Roberto Macovez and Dr. Michela Romanini, always available and willing to help. Thanks for being there in difficult times and for offering your home making me feel like one of the family.

To all the GCM members (especially Efi, Jin, Manesh and Pragya, with whom I shared more than the office), thanks to your friendship, the breaks, coffees and cigarettes and for all the time spent together.

To my family, despite the distance I never felt alone. To who looks at me from up there, and that I always carry with me.

Finally, I am deeply indebted to the most important person in my life: my wife Indre. She has always been there and has shown an immense amount of patience, understanding, and flexibility during my thesis writing. Thanks for being the wonderful woman you are. Aš tave myliu.

Alessandro Vispa
September 2016

Bibliography

[1] P. M. Ossi. *Disordered Material - an introduction.* Springer, 2006.

[2] G. de With. *Liquid-State Physical Chemistry - Fundamentals, Modeling, and Applications.* Wiley-VCH, 2013.

[3] J. A. Barker and D. Henderson. What is "liquid"? understanding the states of matter. *Rev. Mod. Phys.*, 45(4), 1976.

[4] J. M. Ziman. *Models of Disorder - the theoretical physics of homogeneously disordered systems.* Cambridge University Press, Cambridge, 1979.

[5] R. Brand, P. Lunkenheimer, and A. Loidl. Relaxation dynamics in plastic crystals. *J. Chem. Phys.*, 116:10386, 2002.

[6] M. Bée and J. P. Amoureux. Molecular reorientations of 1-chloroadamantane in its plastic solid phase. *Molecular Physics*, 48(1), 1983.

[7] G. Hinze, G. Diezemann, and Th. Basche. Rotational correlation functions of single molecules. *Phys Rev. Lett.*, 93:20, 2004.

[8] K. Kobashi, T. Kyomen, and M. Oguni. Construction of an adiabatic calorimeter in the temperature range between 13 and 505 K, and thermodynamic study of 1-chloroadamantane. *J. Phys. Chem. Solids*, 59:667, 1998.

[9] K. Duvvuri and R. Richert. Dynamics of glass-forming liquids. VI. Dielectric relaxation study of neat decahydro-naphthalene. *J. Chem. Phys.*, 117:4414, 2002.

[10] T. B. Schrøder, S. Sastry, J. C. Dyre, and S. C. Glotzer. Crossover to potential energy landscape dominated dynamics in a model glass-forming liquid. *J. Chem. Phys.*, 112, 2000.

[11] P. Chaudhuri, L. Berthier, and W. Kob. Universal nature of particle displacements close to glass and jamming transitions. *Phys. Rev. Lett.*, 99, 2007.

[12] H. Tanaka, T. Kawasaki, H. Shintani, and K. Watanabe. Critical-like behaviour of glass-forming liquids. *Nat. Mater.*, 9, 2010.

[13] M. T. Cicerone, Q. Zhong, and M. Tyagi. Picosecond dynamic heterogeneity, hopping, and Johari-Goldstein relaxation in glass-forming liquids. *Phys. Rev. Lett.*, 113, 2014.

[14] Y. Grebemichael, T. B. Schrøder, F. W. Starr, and S. C. Glotzer. Spatially correlated dynamics in a simulated glass-forming polymer melt: analysis of clustering phenomena. *Phys. Rev. E: Stat., Nonlinear, Soft Matter Phys.*, 64, 2001.

[15] A. J. Kovacs. La contraction isotherme du volume des polymères amorphes. *Journal of Polymer Science*, 30, 1958.

[16] C. T. Moynihan, A. J. Easteal, M.a. DeBolt, and J. Tucker. Dependence of the fictive temperature of glass on cooling rate. *American Ceramic Society*, 59, 1976.

[17] C. A. Angell. Structural instability and relaxation in liquid and glassy phases near the fragile liquid limit. *J. Non-Cryst. Solids*, 102:205, 1988.

[18] R. Böhmer, K. L. Ngai, C. A. Angell, and D. J. Plazek. Nonexponential relaxations in strong and fragile glass formers. *J. Chem. Phys.*, 99:4201, 1993.

[19] A. Cavagna. Supercooled liquids for pedestrians. *Phys. Rep.*, 476, 2009.

[20] W. Kauzmann. The nature of the glassy state and the behavior of liquids at low temperatures. *Chem. Rev.*, 43:219, 1948.

[21] R. Richert and C. A. Angell. Dynamics of glass-forming liquids. V. on the link between molecular dynamics and configurational entropy. *J. Chem. Phys.*, 108:9016, 1998.

[22] L. M. Martinez and C. A. Angell. A thermodynamic connection to the fragility of glass-forming liquids. *Nature*, 410:663, 2001.

[23] K. L. Ngai and O. Yamamuro. Thermodynamic fragility and kinetic fragility in supercooling liquids: A missing link in molecular liquids. *J. Chem. Phys.*, 111:10403, 1999.

[24] L. Battezzati G. Dalla Fontana. Thermodynamic and dynamic fragility in metallic glass-formers. *Acta Materialia*, 61:2260–2267, 2013.

[25] R. K. Wunderlich H. J. Fecht G. J. Fan, E. J. Lavernia. The relationship between kinetic and thermodynamic fragilities in metallic glass-forming liquids. *Philosophical Magazine*, 84(23):2471–2484, 2004.

[26] K. Ito, C. T. Moynihan, and C. A. Angell. Thermodynamic determination of fragility in liquids and a fragile-to-strong liquid transition in water. *Nature*, 398:492, 1999.

[27] C. A. Angell. Entropy and fragility in supercooling liquids. *J. Res. Natl. Inst. Stand. Technol.*, 102(2):171, 1997.

[28] L. Leuzzi and T. M. Nieuwenhuizen. *Thermodynamics of the Glassy State*. Taylor Francis Group, 2008.

[29] P. G. Debenedetti, T. M. Truskett, C. P. Lewis, and F. H. Stillinger. Theory of supercooled liquids and glasses: energy landscape and statistical geometry perspectives. *Advances in Chemical Engineering*, 28, 2001.

[30] E. Rössler. Indications for a change of diffusion mechanism in supercooled liquids. *Phys. Rev. Lett.*, 65:1595, 1990.

[31] H. Sillescu G. Fleischer F. Fujara, B. Geil. Translational and rotational diffusion in supercooled orthoterphenyl close to the glass transition. *Z. Phys. B*, 88:195, 1992.

[32] M.D. Ediger M.T. Cicerone. Enhanced translation of probe molecules in supercooled o-terphenyl: Signature of spatially heterogeneous dynamics? *J. Chem. Phys.*, 104:7210, 1996.

[33] V. Garcia Sakai, C. Alba-Simionesco, and S.-H. Chen. *Dynamics of soft matter - Neutron applications*. Springer, 2011.

[34] S. W. Lovesey. *The theory of neutron scattering for condensed matter, Vol. 1*. Oxford Science Publications, 1984.

[35] M. Bée. *Quasielastic neutron scattering*. IOP Publishing Ltd, 1988.

[36] T. Lucatorto, A. C. Parr, and K. Baldwin. *Experimental Methods in the Physical Sciences.* Elsevier Inc., 2013.

[37] G. L. Squires. *Introduction to the theory of thermal neutron scattering.* Dover Publications, Inc., 1978.

[38] K. Sköld and D. L. Price. *Methods of Experimental Physics - Neutron scattering.* Academic Press, Inc., 1986.

[39] D. S. Sivia. *Elementary Scattering Theory - for X-ray and Neutron users.* Oxford University Press, 2011.

[40] J. Baruchel, J. L. Hodeau, and M. S. Lehmann. *Neutron and synchrotron radiation for condensed matter studies.* Springer, 1993.

[41] F. Kremer and A. Schönhals. *Broadband dielectric spectroscopy.* Springer, 2002.

[42] Grenoble (France) Institut Laue-Langevin, editor. *The Yellow Book, Guide to Neutron Reasearch Facilities - www.ill.eu/instruments-support/instruments-groups/yellowbook/.* 2008.

[43] A.-J. Dianoux and G. Lander. *Neutron Data Booklet.* OCP Science, 2003.

[44] ISIS Science Technology Facilities Council, editor. *ISIS, Instruments - www.isis.stfc.ac.uk/instruments/instruments2105.html.*

[45] P. Heitjans and J. Kärger. *Diffusion in Condensed Matter - Methods, Materials, Models.* Springer, 2005.

[46] V. Garcìa Sakai. Quasi-elastic neutron scattering. *13th Oxford School of Neutron Scattering*, 2013.

[47] B.T.M. Willis and C.J. Carlile. *Experimental Neutron Scattering.* 2009.

[48] R.E. Lechner. Neutron investigations of superprotonic conductors. *Ferroelectrics*, 167, 1995.

[49] STFC Rutherford Appleton Laboratory. *Iris - Workhorse high-resolution spectrometer at ISIS.* 2016.

[50] V. Garcia Sakai, M. A. Adams, W. S. Howells, M. T. F. Telling, F. Demmel, and F. Fernandez-Alonso. *The IRIS User Guide - 3rd Edition.* 2010.

[51] Research Neutron Source Heinz Maier-Leibnitz (FRM II) Technical University of Munich, editor. *www.mlz-garching.de/.*

[52] T. Unruh, J. Neuhaus, and W. Petry. The high-resolution time-of-flight spectrometer TOFTOF. *Nuclear Instruments Methods in Physics Research A*, 580:1414–1422, 2007.

[53] T. Unruh, J. Neuhaus, and W. Petry. Erratum to "the high-resolution time-of-flight spectrometer TOFTOF" [Nucl. Instr. and Meth. A 580 (2007) 1414-1422]. *Nuclear Instruments Methods in Physics Research A*, 585, 2008.

[54] E. Guarini. *Scattering anelastico di neutroni e tecniche di analisi dati.* 2003.

[55] J. Wuttke. Frida (Fast Reliable Inelastic Data Analyis). http://apps.jcns.fz-juelich.de/doku/frida/start.

[56] Mantid: Manipulation Analysis Toolkit for Instrument Data., editor. *Mantid Project. http://dx.doi.org/10.5286/SOFTWARE/MANTID.* 2013.

[57] H. H. Paalman and C. J. Pings. Numerical evaluation of x-ray absorption factors for cylindrical samples and annular sample cells. *Journal of Applied Physics*, 33(8):2635, 1962.

[58] NIST Center for Neutron Research. *DAVE - Data Analysis and Visualization Environment.* 2009.

[59] A. Cunsolo, A. Orecchini, C. Petrillo, and F. Sacchetti. On the anomalous behaviour of microscopic diffusion of liquid water. *Journal of Physics: Condensed Matter*, 19, 2007.

[60] A. Cunsolo, A. Orecchini, C. Petrillo, and F. Sacchetti. Interplay between microscopic diffusion and local structure of liquid water. *Journal of Physical Chemistry B*, 114(50), 2010.

[61] S. H. Chen, C. Liao, F. Sciortino, P. Gallo, and P. Tartaglia. Model for single-particle dynamics in supercooled water. *Physical Review E*, 59, 1999.

[62] A. Faraone, L. Liu, C.-Y. Mou, P.-C. Shih, J. R. D. Copley, and S.-H. Chen. Translational and rotational dynamics of water in mesoporous silica materials: MCM-41-S and MCM-48-S. *Journal of Chemical Physics*, 119(7), 2003.

[63] M. D. Ediger. Spatially heterogeneous dynamics in supercooled liquids. *Annu. Rev. Phys. Chem.*, 51, 2000.

[64] V. F. Sears. Theory of cold neutron scattering by homonuclear diatomic liquids: I. Free rotation. *Canadian Journal of Physics*, 44(6), 1966.

[65] CRG two-axis diffractometer D1B. *www.ill.eu/instrumentssupport/instruments-groups/instruments/d1b*. 2016.

[66] D. Richard, M. Ferrand, and G. J. Kearley. *The Lamp Book*. 2006.

[67] J. Rodríguez-Carvajal. Recent developments of the program FULLPROF, in commission on powder diffraction (IUCr). available www.ill.eu/sites/fullprof. *Newsletter*, 26:12–19, 2001.

[68] I. A. Blech and B. L. Averbach. Multiple scattering of neutrons in vanadium and copper. *Phys. Rev.*, 137:A1113âA1116, 1965.

[69] V. F. Sears. Slow-neutron multiple scattering. *Adv. Phys.*, 24(1):1–45, 1975.

[70] A. K. Soper and P. A. Egelstaff. Multiple scattering and attenuation of neutrons in concentric cylinders: I. isotropic first scattering. *Nuclear Instruments and Methods*, 178(2-3):415, 1980.

[71] T. Bausenwein, H. Bertagnolli, K. Tödheide, and P. Chieux. Multiple scattering and self-absorption correction for highpressure neutron diffraction with cylindrical cells. *Nuclear Instruments and Methods in Physics Research Section B: Beam Interactions with Materials and Atoms*, 61(4):527, 1991.

[72] L. A. Rodríguez Palomino, J. Dawidowski, J. J. Blostein, and G. J. Cuello. Data processing method for neutron diffraction experiments. *Nuclear Instruments and Methods in Physics Research Section B: Beam Interactions with Materials and Atoms*, 258(2):453, 2007.

[73] T. Roisnel and J. Rodríguez-Carvajal. WinPLOTR: a Windows tool for powder diffraction patterns analysis, Materials Science Forum. *Proceedings of the Seventh European Powder Diffraction Conference (EPDIC 7)*, pages 118–123, 2000.

[74] P. F. Mosotti. Ueber die fraunhofer'schen gitterspectra und analyse des lichtes derselben. *Bibl. Univ. Modena*, 6:193, 1847.

[75] R. Clausius. Die mechanische behandlung der electricität. *Die mechanische Wärmelehre*, 2, 1879.

[76] L. Onsager. Electric moments of molecules in liquids. *J. Am. Chem. Soc.*, 58, 1936.

[77] J. G. Kirkwood. The dielectric polarization of polar liquids. *J. Chem. Phys.*, 58, 1939.

[78] J. G. Kirkwood. The local field in dielectrics. *Ann. NY Acad. Sci.*, 40, 1940.

[79] J. G. Kirkwood. The influence of hindered molecular rotation on the dielectric polarisation of polar liquids. *Trans. Faraday Soc.*, 42, 1946.

[80] H. Fröhlich. *Theory of Dielectrics.* London: Oxford Univ. Press, 1958.

[81] P. Lunkenheimer, U. Schneider, R. Brand, and A. Loidl. Glassy dynamics. *Contemp. Phys.*, 41:15, 2000.

[82] P. Lunkenheimer and A. Loidl. Dielectric spectroscopy of glass-forming materials: α-relaxation and excess wing. *Chem. Phys.*, 284:205, 2002.

[83] Novocontrol Technologies. *www.novocontrol.de.* 2016.

[84] Novocontrol Technologies. *www.novocontrol.de/html/index_temp_contr.htm.* 2016.

[85] M. Wübbenhorst and J. van Turnhout. Analysis of complex dielectric spectra. i. one-dimensional derivative techniques and three-dimensional modelling. *J. Non. Cryst. Solids*, 305:40, 2002.

[86] J.F. Böttcher and P. Bordewijk. *Theory of Electric Polarisation, vol. 2, second edition.* 1992.

[87] P. Debye. *Polar Molecules.* New York: Chem. Catalog, 1929.

[88] K. S. Cole and R. H. Cole. Dispersion and absorption in dielectrics I. Alternating current characteristics. *J. Chem. Phys.*, 9, 1941.

[89] D. W. Davidson and R. H. Cole. Dielectric relaxation in glycerine. *J. Chem. Phys.*, 18, 1950.

[90] S. Havrilliak and S. Negami. A complex plane analysis of α-dispersions in some polymer systems. *J. Polym. Sci. C*, 14, 1966.

[91] S. Havrilliak and S. Negami. A complex plane representation of dielectric and mechanical relaxation processes in some polymers. *Polymer*, 8, 1967.

[92] R. Kohlrausch. Ueber das dellmann'sche elektrometer. *Pogg. Ann. Phys.*, 72(3), 1847.

[93] A. Alvarez, A. Alegria, and J. Colmenero. Relationship between the time-domain Kohlrausch-Williams-Watts and frequency-domain Havriliak-Negami relaxation functions. *Phys. Rev. B*, 44, 1991.

[94] P. Lunkenheimer, L. C. Pardo, M. Köhler, and A. Loidl. Broadband dielectric spectroscopy on benzophenone: α relaxation, β relaxation, and mode coupling theory. *Phy. Rev. E*, 77, 2008.

[95] G. P. Johari and M. Goldstein. Viscous liquids and the glass transition. II. secondary relaxations in glasses of rigid molecules. *J. Chem. Phys.*, 53:2372, 1970.

[96] N. G. McCrum, B. E. Read, and G. Williams. *Anelastic dielectric effects in polymeric solids.* Dover Publications, 1991.

[97] K. L. Ngai, P. Lunkenheimer, C. León, U. Schneider, R. Brand, and A. Loidl. Nature and properties of the Johari-Goldstein β-relaxation in the equilibrium liquid state of a class of glass-formers. *J. Chem. Phys.*, 115, 2001.

[98] S. Pawlus, M. Paluch, M. Sekula, K. L. Ngai, S. J. Rzoska, and J. Ziolo. Changes in dynamic crossover with temperature and pressure in glass-forming diethyl phthalate. *Phy. Rev. E*, 68, 2003.

[99] R. Nath, A. Nowaczyk, B. Geil, and R. Böhmer. ^{2}H NMR studies of supercooled and glassy aspirin. *J. Non-Cryst. Solids*, 353, 2007.

[100] K. Adrjanowicz, K. Kaminski, Z. Wojnarowska, M. Dulski, L. Hawelek, S. Pawlus, M. Paluch, and W. Sawicki. Dielectric relaxation and crystallization kinetics of ibuprofen at ambient and elevated pressure. *J. Phys. Chem. B*, 114, 2010.

[101] M. Vogel and E. Rössler. Slow beta process in simple organic glass formers studied by one- and two-dimensional H_2 nuclear magnetic resonance. i. *J. Chem. Phys.*, 114, 2001.

[102] J. S. Harmon, M. D. Demetriou, W. L. Johnson, and K. Samwer. Anelastic to plastic transition in metallic glass-forming liquids. *Phys. Rev. Lett.*, 99, 2007.

[103] C. Gainaru, O. Lips, A. Troshagina, R. Kahlau, A. Brodin, F. Fujara, and E. A. Rössler. On the nature of the high-frequency relaxation in a molecular glass former: a joint study of glycerol by field cycling NMR, dielectric spectroscopy, and light scattering. *J. Chem. Phys.*, 128, 2008.

[104] W. Götze. Properties of the glass instability treated within a mode coupling theory. *Z. Physik B*, 60, 1985.

[105] W. Götze and L. Sjögren. Relaxation processes in supercooled liquids. *Rep. Prog. Phys.*, 55, 1992.

[106] W. Götze. *Complex Dynamics of Glass-Forming Liquids.* Oxford University Press, 2009.

[107] E. Leutheusser. Dynamical model of the liquid-glass transition. *Phys. Rev. A*, 29, 1984.

[108] G. Li, W. M. Du, X. K. Chen, and H. Z. Cummins. Testing mode-coupling predictions for α and β relaxation in $Ca_{0.4}K_{0.6}(NO_3)_{1.4}$ near the liquid-glass transition by light scattering. *Phys. Rev. A*, 45, 1992.

[109] J. Wuttke, J. Hernez, G. Li, G. Coddens, H. Z. Cummins, F. Fujara, W. Petry, and H. Sillescu. Neutron and light scattering study of supercooled glycerol. *Phys. Rev. Lett.*, 72:3052, 1994.

[110] W. Götze and M. R. Mayr. Evolution of vibrational excitations in glassy systems. *Phys. Rev. E*, 61, 2000.

[111] L. C. Pardo, M. Rovira-Esteva, S. Busch, J.-F. Moulin, and J. L. Tamarit. Fitting in a complex χ^2 landscape using an optimized hypersurface sampling. *Phys. Rev. E*, 84:046711, 2011.

[112] D. Sivia and J. Skilling. *Data Analysis: A Bayesian Tutorial.* 2006.

[113] G. Sala, F. Haberl, J. José, A. Parikh, R. Longl, L. C. Pardo, and M. Andersen. Constraints on the mass and radius of the accreting neutron star in the rapid burster. *Astrophys. J.*, 752(2), 2012.

[114] N. Metropolis, A. Rosenbluth, M. Rosenbluth, A. Teller, and E. Teller. Equation of state calculations by fast computing machines. *J. Chem. Phys.*, 21, 1953.

[115] L. C. Pardo, M. Rovira-Esteva, S. Busch, M. D. Ruiz-Martìn, and J. Ll. Tamarit. FABADA: a Fitting Algorithm for Bayesian Analysis of DAta. *J. Phys.: Conf. Ser.*, 325, 2011.

[116] L. C. Pardo. *https://gcm.upc.edu/en/members/luis-carlos.*

[117] L. C. Pardo. *https://gcm.upc.edu/en/members/luis-carlos/bayes$_v$3.ppt.* 2013.

[118] L.C. Pardo, M. Rovira-Esteva, S. Busch, M.D. Ruiz-Martin, J.Ll. Tamarit, and T. Unruh. Bayesian analysis of QENS data: From parameter determination to model selection. *arXiv:0907.3711v3 [physics.data-an]*, 2009.

[119] D. Monserrat, A. Vispa, L. C. Pardo, R. Tolchenov, S. Mukhopadhyay, and F. Fernandez-Alonso. FABADA goes MANTID to answer an old question: How many lines are there? *J. Phys.: Conf. Ser.*, 663, 2015.

[120] K. J. Chang and M. L. Cohen. Solid-solid phase transitions and soft phonon modes in highly condensed Si. *Phys. Rev. B*, 31, 1985.

[121] Y. Peng, F. Wang, Z. Wang, A. M. Alsayed, Z. Zhang, A. G. Yodh, and Y. Han. Two-step nucleation mechanism in solid-solid phase transitions. *Nat. Mat.*, 14:101–108, 2015.

[122] N. Giovambattista, T. Loerting, B. R. Lukanov, and F. W. Starr. Interplay of the glass transition and the liquid-liquid phase transition in water. *Scientific Reports*, 390, 2012.

[123] H. Tanaka, R. Kurita, and H. Mataki. Liquid-liquid transition in the molecular liquid triphenyl phosphite. *Phys. Rev. Lett.*, 92:025701, 2004.

[124] R. Kurita and H. Tanaka. Critical-like phenomena associated with liquid-liquid transition in a molecular liquid. *Science*, 306, 2004.

[125] G. Franzese, G. Malescio, A. Skibinsky, S. V. Buldyrev, and H. E. Stanley. Generic mechanism for generating a liquid-liquid phase transition. *Nature*, 409, 2001.

[126] T. Speck, C. P. Royall, and S. R. Williams. Liquid-liquid phase transition in an atomistic model glass former. *arXiv:1409.0751v2 [cond-mat.stat-mech]*, 2014.

[127] L. Carpentier, R. Decressain, and M. Descamps. Influence of phase transformation on the low temperature dielectric measurements in 1-cyanoadamantane. *J. Chem. Phys.*, 128:024702, 2008.

[128] Y. Huang, D. F. R. Gilson, I. S. Butler, and F. Morin. Study of molecular motions in the orientationally disordered organic solids 1-bromoadamantane and 1-adamantanecarboxylic acid by carbon-13 NMR spin-lattice relaxation and dipolar dephasing time measurements. *J. Phys. Chem.*, 95:2151–2156, 1991.

[129] Y. Huang, R. M. Paroli, D. F. R. Gilson, and I. S. Butler. Order-disorder transitions in adamantane derivatives: vibrational spectroscopic and 13C NMR studies of 1-chloroadamantane. *Can. J. Chem.*, 71, 1993.

[130] J. C. Martinez-Garcia, J. Ll. Tamarit, S. Capaccioli, M. Barrio, N. Veglio, and L. C. Pardo. α-relaxation dynamics of orientanionally disordered mixed crystals composed of Cl-adamantane and CN-adamantane. *J. Chem. Phys.*, 132:164516, 2010.

[131] B. B. Hassine, P. Negrier, M. Barrio, D. Mondieig, S. Massip, and J. Ll. Tamarit. Phase transition in hydrogen-bonded 1-adamantane-methanol. *Cryst. Growth Des.*, 15:4149–4155, 2015.

[132] F. Affouard. Orientationally disordered crystals: from the onset of slow dynamics to the glass transition. *J. Non-Cryst. Solids*, 307-310:9–15, 2002.

[133] P. Negrier, M. Barrio, J. Ll. Tamarit, and D. Mondieig. Polymorphism in 2-X-adamantane derivatives (X= Cl, Br). *J. Phys. Chem. B*, 118:9595–9603, 2014.

[134] J. F. Willart and M. Descamps. Structural signature of the configurational entropy change during the glass formation of plastic crystal cyanoadamantane. *J. Chem. Phys.*, 112, 2000.

[135] R. Angelini, T. Scopigno, A. Beraud, and G. Ruocco. High frequency dynamics of an orientationally disordered molecular crystal. *J. Non-Crystalline Solids*, 352:4552–4555, 2006.

[136] T. Clark, T. Mc O. Knox, H. Mackle, and M. A. McKervey. Order-disorder transitions in substituted adamantanes. *J. Chem. Soc., Faraday Trans. 1*, 73:1224, 1977.

[137] L.A. Fraczyk and Y. Huang. A high pressure FT-IR spectroscopic study of phase transitions in 1-chloro-and 1-bromoadamantane. *Spectrochimica Acta Part A*, 57:1061–1071, 2001.

[138] M. Bée and J. P. Amoureux. Quasielastic neutron scattering study of reorientational motions in 2-adamantanone $C_{10}H_{14}O$. *Mol. Phys.*, 47 (3):533–550, 1982.

[139] F. Affouard and M. Descamps. Two-step rotational relaxation in glassy crystal cyanoadamantane. *Phys. Rev. B*, 59:14, 1999.

[140] F. Affouard, E. Cochin, R. Decressain, and M. Descamps. Experimental and numerical signatures of dynamical crossover in orientationally disordered crystals. *Europhys. Lett.*, 53 (5):611–617, 2001.

[141] G. Ali Mansoori. Diamondoid molecules. *Advances in Chemical Physics*, 136:207–258, 2007.

[142] J. P. Amoureux, M. Sahour, C. Fernandez, and P. Bodart. Dielectric properties of chloroadamantane and adamantanone. *Phys. Status Solid*, 143:441, 1994.

[143] P. Bordat, A. Lerbret, M. Descamps, and F. Affouard. Slow dynamics in glass-forming materials. *Mol. Simulat.*, 32:12–13, 2006.

[144] A. Henao, M. Rovira-Esteva, A. Vispa, J. Ll. Tamarit, E. Guardia, and L. C. Pardo. Insights into the determination of molecular structure from diffraction data using a Bayesian algorithm. *J. Phys.: Cond. Matter*, 25:454217, 2013.

[145] M. Rovira-Esteva, N. A. Murugan, L. C. Pardo, S. Busch, J. Ll. Tamarit, Sz. Pothoczki, G. J. Cuello, and F. J. Bermejo. Interplay between intramolecular and intermolecular structures of 1,1,2,2-tetrachloro-1,2-difluoroethane. *Phys. Rev. B*, 84:064202, 2011.

[146] S. Busch, C. Smuda, L. C. Pardo, and T. Unruh. Molecular mechanism of long-range diffusion in phospholipid membranes studied by quasielastic neutron scattering. *J. Am. Chem. Soc.*, 10:3232, 2010.

[147] M. Rovira-Esteva, A. Murugan, L. C. Pardo, S. Busch, M. D. Ruiz-Martìn, M. S. Appavou, J. Ll. Tamarit, C. Smuda, T. Unruh, F. J. Bermejo, G. J. Cuello, and S. J. Rzoska. Microscopic structures and dynamics of high-and low-density liquid tran s-1,2-dichloroethylene. *Phys. Rev. B*, 81 (9):092202, 2010.

[148] A. Vispa, S. Busch, J. L. Tamarit, T. Unruh, F. Fernandez-Alonso, and L. C. Pardo. A robust comparison of dynamical scenarios in a glass-forming liquid. *Phys. Chem. Chem. Phys.*, 18:3975, 2016.

[149] I. V. Sharapova, A. I. Krivchikov, O. A. Korolyukand A. Jezowski, M. Rovira-Esteva, J. Ll. Tamarit, L. C. Pardo, M. D. Ruiz-Martin, and F. J. Bermejo. Disorder effects on heat transport properties of orientationally disordered crystals. *Phys. Rev. B*, 81:094205, 2010.

[150] P. Negrier, M. Barrio, J. Ll. Tamarit, L. C. Pardo, and D. Mondieig. Polymorphism in halogen-ethane derivatives: CCl_3-CF_2Cl and CF_3-CF_2Cl. *Cryst. Growth Des.*, 12 (3):1513–1519, 2012.

[151] P. Negrier, J. Ll. Tamarit, M. Barrio, and D. Mondieig. Polymorphism in halogen-ethane derivatives: CCl_3-CCl_3 and ClF_2C-CF_2Cl. *Cryst. Growth Des.*, 13 (2):782–791, 2013.

[152] G. A. Vdovichenko, A. I. Krivchikov, O. A. Korolyuk, J. Ll. Tamarit, L. C. Pardo, M. Rovira-Esteva, F. J. Bermejo, M. Hassaine, and M. A. Ramos. Thermal properties of halogen-ethane glassy crystals: Effects of orientational disorder and the role of internal molecular degrees of freedom. *J. Chem. Phys.*, 143:084510, 2015.

[153] S. C. Pérez, M. Zuriaga, P. Serra, A. Wolfenson, Ph. Negrier, and J. Ll. Tamarit. Dynamic characterization of crystalline and glass phases of deuterated 1,1,2,2-tetrachloroethane. *J. Chem. Phys.*, 143:134502, 2015.

[154] L. C. Pardo, P. Lunkenheimer, and A. Loidl. α and β relaxation dynamics of a fragile plastic crystal. *J. Chem. Phys.*, 124:124911, 2006.

[155] A.P. Sokolov, R. Calemczuk, B. Salce, A. Kisliuk, D. Quitmann, and E. Duval. Low-temperature anomalies in strong and fragile glass formers. *Phys. Rev. Lett.*, 78:2405, 1997.

[156] R. Brand, P. Lunkenheimer, and A. Loidl. Relaxations and fast dynamics of the plastic crystal cyclo-octanol investigated by broadband dielectric spectroscopy. *Phys. Rev. B*, 56:5713, 1997.

[157] R. Puertas, M. A. Rute, J. Salud, D. O. López, S. Diez, J. K. van Miltenburg, L. C. Pardo, J. Ll. Tamarit, M. Barrio, M. A. Pérez-Jubindo, and M. R. de la Fuente. Thermodynamic, crystallographic, and dielectric study of the nature of glass transitions in cyclo-octanol. *Phys. Rev. B*, 69:224202, 2004.

[158] R. Puertas, J. Salud, D.O. López, M.A. Rute, S. Diez, J.Ll. Tamarit, M. Barrio, M.A. Pèrez-Jubindo, M.R. de la Fuente, and L.C. Pardo. Static and dynamic studies on cycloheptanol as two-orientational glass-former. *Chem. Phys. Lett.*, 401:368, 2005.

[159] P. Lunkenheimer and A. Loidl. Molecular reorientation in ortho-carborane studied by dielectric spectroscopy. *J. Chem. Phys.*, 104:4324, 1996.

[160] J. C. Martinez-Garcia, J. Ll. Tamarit, S. Capaccioli, M. Barrio, N. Veglio, and L. C. Pardo. α-relaxation dynamics of orientanionally disordered mixed crystals composed of Cl-adamantane and CN-adamantane. *J. Chem. Phys.*, 132:164516, 2010.

[161] M. Romanini, Ph. Negrier, J. Ll. Tamarit, S. Capaccioli, M. Barrio, L. C. Pardo, and D. Mondieig. Emergence of glassy-like dynamics in an orientationally ordered phase. *Phys. Rev. B*, 85:134201, 2012.

[162] J. Ll. Tamarit, D. O. López, M. R. de la Fuente, M. A. Pérez-Jubindo, and M. Barrio J. Salud. Relaxation dynamics in orientationally disordered molecular mixed crystal $[(CH_3)_3CCH_2OH]_{0.7}$ $[(CH_3)_2C(CH_2OH)_2]_{0.3}$. *J. Phys.: Condens. Matter*, 12:8209, 2000.

[163] A. Drozd-Rzoska, S. J. Rzoska, S. Pawlus, and J. Ll. Tamarit. Dynamics crossover and dynamic scaling description in vitrification of orientationally disordered crystal. *Phys. Rev. B*, 73:224205, 2006.

[164] A. Drozd-Rzoska, S. J. Rzoska, S. Pawlus, and J. Ll. Tamarit. Dielectric relaxation in compressed glassy and orientationally disordered mixed crystals. *Phys. Rev. B*, 74:064201, 2006.

[165] C.A. Angell. Relaxation in liquids, polymers and plastic crystals-strong/fragile patterns and problems. *J. Non-Crystalline Solids*, 13:131–133, 1991.

[166] D. Huang and G. B. McKenna. New insights into the fragility dilemma in liquids. *J. Chem. Phys.*, 114:5621, 2001.

[167] G. Ruocco, F. Sciortino, F. Zamponi, C. De Michele, and T. Scopigno. Landscapes and fragilities. *J. Chem. Phys.*, 120:10666, 2004.

[168] F. Mizuno, J.-P. Belieres, N. Kuwata, A. Pradel, M. Ribes, and C. A. Angell. Highly decoupled ionic and protonic solid electrolyte systems, in relation to other relaxing systems and their energy landscapes. *J. Non-Crystalline Solids*, 352:5147, 2006.

[169] V. P. Kolesov, E. A. Kosarukina, D. Yu. Zhogin, M. E. Poloznikova, and Yu. A. Pentin. Heat capacities, phase transitions, and thermodynamic functions of 1,1,2,2-tetrafluoro-1,2-dichloroethane and 1,1,2-trifluoro-1,2,2-trichloroethane. *J. Chem. Thermodynamics*, 13:115, 1981.

[170] D. Szewczyk, A. Jezowski, G. A Vdovichenko, A. I. Krivchikov, F. J. Bermejo, J. Ll. Tamarit, L. C. Pardo, and J. W. Taylor. Glassy dynamics versus thermodynamics: The case of 2-adamantanone. *J. Phys. Chem. B*, 119:8468, 2015.

[171] A. I. Krivchikov, O. A. Korolyuk, I. V. Sharapova, J. Ll. Tamarit, F. J. Bermejo, L. C. Pardo, M. Rovira-Esteva, M. D. Ruiz-Martin, A. Jezowski, J. Baran, and

N. A. Davydova. Effects of internal molecular degrees of freedom on the thermal conductivity of some glasses and disordered crystals. *Phys. Rev. B*, 85:014206, 2012.

[172] B. Kabtoul, R. J. Jiménez-Riobóo, and M. A. Ramos. Thermal and acoustic experiments on polymorphic ethanol. *Phil. Mag.*, 88:4197, 2008.

[173] M. A. Ramos, M. Hassaine, and B. Kabtoul. Low-temperature properties of monoalcohol glasses and crystals. *Low Temp. Phys.*, 39:600, 2013.

[174] M. Goldstein. Viscous liquids and the glass transition: a potential energy barrier picture. *J. Chem. Phys.*, 51:3728, 1969.

[175] S. Sastry. The relationship between fragility, configurational entropy and the potential energy landscape of glass-forming liquids. *Nature*, 409:164, 2001.

[176] V. Lubchenko and P. G. Wolynes. Theory of structural glasses and supercooled liquids. *Annu. Rev. Phys. Chem.*, 58:235–66, 2007.

[177] H. Tanaka. Two-order-parameter description of liquids. I. A general model of glass transition covering its strong to fragile limit. *J. Chem. Phys.*, 111:3163, 1999.

[178] H. Tanaka. Simple view of waterlike anomalies of atomic liquids with directional bonding. *Phys. Rev. B*, 66:064202, 2002.

[179] W. F. Rall and G. M. Fahy. Ice-free cryopreservation of mouse embryos at -196 °C by vitrification. *Nature*, 313:573, 1985.

[180] D. Li, B. Liu, Y. Liu, and C. Chen. Predict the glass transition temperature of glycerol-water binary cryoprotectant by molecular dynamic simulation. *Cryobiology*, 56:114, 2008.

[181] U. Schneider, R. Brand, P. Lunkenheimer, and A. Loidl. Excess wing in the dielectric loss of glass formers: A Johari-Goldstein β relaxation? *Phys. Rev. Lett.*, 84:5560, 2000.

[182] U. Schneider, R. Brand, P. Lunkenheimer, and A. Loidl. Dielectric and far-infrared spectroscopy of glycerol. *J. Non-Cryst. Solids*, 235:173, 1998.

[183] P. Lunkenheimer, R. Wehn, U. Schneider, and A. Loidl. Glassy aging dynamics. *Phys. Rev. Lett.*, 95:055702, 2005.

[184] A. Brodin and E. A. Rössler. Depolarized light scattering study of glycerol. *Eur. Phys. J. B*, 44:3, 2005.

[185] D. J. Tomlinson. Temperature dependent self-diffusion coefficient measurements of glycerol by the pulsed NMR technique. *Mol. Phys.*, 25:735, 1972.

[186] L. J. Burnett and J. F. Harmon. Self-diffusion in viscous liquids: Pulse NMR measurements. *J. Chem. Phys.*, 57:1293, 1972.

[187] D. Aranghel, V. Tripadus, A. Radulescu, M. Petre, M. O. Dima, and C. Petre. Quasielastic neutron scattering on glycerol. *J. Optoelectron. Adv. M.*, 12:953, 2010.

[188] K. F. Larsson. Rotational and translational diffusion in complex liquids. *Phys. Rev.*, 167:171, 1968.

[189] C. M. Roland and K. L. Ngai. Short-time viscous and density relaxation in glycerol and ortho-terphenyl. *J. Chem. Phys.*, 106:1187, 1997.

[190] R. Busselez, R. Lefort, A. Ghoufi, B. Beuneu, B. Frick, F. Affouard, and D. Morineau. The non-Gaussian dynamics of glycerol. *J. Phys.: Cond. Matter*, 23:505102, 2011.

[191] E. Mamontov. Diffusion in confinement as a microscopic relaxation mechanism in glass-forming liquids. *Chem. Phys. Lett.*, 530:55, 2012.

[192] J. Blieck, F. Affouard, P. Bordat, A. Lerbret, and M. Descamps. Molecular dynamics simulations of glycerol glass-forming liquid. *Chem. Phys.*, 317:253, 2005.

[193] J. Wuttke, I. Chang, O. G. Randl, F. Fujara, and W. Petry. Tagged-particle motion in viscous glycerol: Diffusion-relaxation crossover. *Phys. Rev. E*, 54:5364, 1996.

[194] J. Wuttke, W. Petry, G. Coddens, and F. Fujara. Fast dynamics of glass-forming glycerol. *Phys. Rev. E*, 52:4026, 1995.

[195] C. A. Angell. Liquid fragility and the glass transition in water and aqueous solutions. *Chem. Rev.*, 102:2627–2650, 2002.

[196] B. Best. *http://www.benbest.com/cryonics/mobility.html*. 1990.

[197] J. Orava. Characterization of supercooled liquid $Ge_2Sb_2Te_5$ and its crystallization by ultrafast-heating calorimetry. *Nat. Mat.*, 11, 2012.

[198] NPL National Physical Laboratoy. *http://www.kayelaby.npl.co.uk*. 1995.

[199] IPS Engineering. *http://www.ips-engineering.it/pulp-paper/105-data-book/189-viscosity-of-glycerol-water-solutions*. 2016.

[200] L. B. Lane. Freezing points of glycerol and its aqueous solutions. *Ind. Eng. Chem.*, 17:924, 1925.

[201] The Soap Detergent Association Glycerine Oleochemical Division, editor. *Glycerin: an overview*. 1990.

[202] T. Unruh, J. Neuhaus, and W. Petry. The high-resolution time-of-flight spectrometer TOFTOF. *Nucl. Instrum. Meth. Phys. Res. Sect. A*, 580:1414, 2007.

[203] D. S. Sivia and C. J. Carlile. Molecular spectroscopy and Bayesian spectral analysis - how many lines are there? *J. Chem. Phys.*, 96:170, 1992.

[204] T. Kikuchi, K. Nakajima, S. Ohira-Kawamura, Y. Inamura, O. Yamamuro, M. Kofu, Y. Kawakita, K. Suzuya, M. Nakamura, and M. Arai. Mode-distribution analysis of quasielastic neutron scattering and application to liquid water. *Phys. Rev. E*, 87:062314, 2013.

[205] S. Busch and T. Unruh. The slow short-time motions of phospholipid molecules with a focus on the influence of multiple scattering and fitting artefacts. *J. Phys.: Cond. Matter*, 23:254205, 2011.

[206] S. A. Reinsberg, X. H. Qiu, M. Wilhelm, H. W. Spiess, and M. D. Ediger. Length scale of dynamic heterogeneity in supercooled glycerol near T_g. *J. Chem. Phys*, 114, 2001.

[207] S. Busch. *The Pico- to Nanosecond Dynamics of Phospholipid Molecules*. PhD Thesis, Technische Universität München, 2012.

[208] G. P. Johari. Glass transition and secondary relaxations in molecular liquids and crystals. *Ann. NY Acad. Sci.*, 279:117, 1976.

[209] A. Vispa, M. Rovira-Esteva, M. D. Ruiz-Martín, S. Busch, T. Unruh, L. C. Pardo, and J. Ll. Tamarit. Microscopic dynamics of glycerol: a QENS study. *J. Phys.: Conf. Ser.*, 549:012013, 2014.

[210] F. Fernandez-Alonso, F. J. Bermejo, S. E. McLain, J. F. C. Turner, J. J. Molaison, and K. W. Herwig. Observation of fractional Stokes-Einstein behavior in the simplest hydrogen-bonded liquid. *Phys. Rev. Lett*, 98:077801, 2007.

[211] F. Fernandez-Alonso, S. E. McLain, J. W. Taylor, F. J. Bermejo, I. Bustinduy, M. D. Ruiz-Martín, and J. F. C. Turner. Correlated atomic motions in liquid deuterium fluoride studied by coherent quasielastic neutron scattering. *J. Chem. Phys.*, 126:234509, 2007.

[212] A. Rahman, K. S. Singwi, and A. Sjöler. Theory of slow neutron scattering by liquids. I. *Phys. Rev.*, 126:986, 1962.

[213] J. P. Boon and S. Yip. *Molecular Hydrodynamics.* McGraw-Hill, 1980.